Title

Application of BioMEMS, Optics, and Electronics to Bioenergy

Author

Song, Minsun

Publication Date

2019

Peer reviewed|Thesis/dissertation

Application of BioMEMS, Optics, and Electronics to Bioenergy

By

Minsun Song

A dissertation submitted in partial satisfaction of the

requirements for the degree of

Joint Doctor of Philosophy
with University of California, San Francisco

in

Bioengineering

in the

Graduate Division

of the

University of California, Berkeley

Committee in charge:

Professor Luke P. Lee, Chair

Professor Ming-Chiang Wu

Professor Randall Lee

Fall 2019

Abstract

Application of BioMEMS, Optics, and Electronics to Bioenergy

by

Minsun Song

Doctor of Philosophy in Bioengineering

University of California, Berkeley

Professor Luke P. Lee, Chair

Today, the development of eco-friendly and renewable energy sources is imperative because we are facing a severe global warming and energy depletion. In this regard, the microalgae that absorb carbon dioxide from the atmosphere and convert it into a high-energy carrier which can be used as biofuel are in the spotlight. Microalgae have been considered as a next-generation energy source in that it is not only extremely renewable and reducing carbon dioxide but also highly productive even with non-arable lands, seawater or wastewater. However, its applicability to next-generation energy sources still faces practical limitations, such as the higher unit cost of producing microalgae-based biofuel compared to fossil fuels. The reason is that technologies essential to efficient and economically competitive production of microalgae-based biofuel have not yet been fully developed. The representative bottlenecks include the lack of technologies as follows; 1) methods for screening the most productive microalgae strain from the hundreds of thousands of natural and genetically engineered strains rapidly and efficiently. 2) on-site, real-time, and non-invasive methods for monitoring of mass production of microalgae over the extensive area. In this respect, this thesis discusses the novel methods for superior microalgal species selection and real-time microalgal cultivation monitoring utilizing various technologies of BioMEMS, optics, and electronics.

First, we demonstrate a buoyancy-based cell separation method that can easily sort out the best microalgal strain accumulating the largest amount of lipids using BioMEMS technology. Our simple microfluidic channel structure inducing hydraulic jumps of incoming cells allows the selection of only the lightest species (i.e., superior one which accumulates the largest amount of lipid) among numerous microalgae cells having various densities depending on their lipid amount. This method has the advantage of being able to select superior species easily and rapidly without additional labeling process and observation of the entire microalgal growth process.

Second, we demonstrate an integrated microalgae analysis photobioreactor for rapid strain selection using optics. Our photobioreactor, hemispherical cavity embedded with metal nanostructures, scatters specific wavelengths favored by microalgae, which will increase the photosynthetic efficiency of microalgae, resulting in shorter screening times

through rapid growth. Besides, the additional optical property (i.e., light focusing) provided by the geometry of a hemispherical cavity helps rapid screening even with naked-eye by facilitating rapid growth through cell gathering and cell-cell interactions.

Lastly, we demonstrate a novel electrical sensor that can effectively monitor microalgae in the real field. Our approach utilizes electric signal, photocurrent, derived from the channel-rhodopsin, a unique feature of microalgae. This new method overcomes the limitations in terms of the field application that other existing approaches have not solved in that it can monitor microalgae in real-time and in-situ even with low cost without the need for additional sample processing steps.

We believe this series of new approaches can elevate the productivity in real fields of microalgae-based biofuel production by contributing to the superior strain selection and production management and are expected to provide an opportunity to step closer to the realization of microalgae as a next-generation energy source.

Table of Contents

Acknowledgments

I would like to express my most sincere gratitude to every one of those who contributed to this study. This dissertation would not have been accomplished without the guidance and support of several people who have provided invaluable help throughout the process of conducting this study.

First and above all, I would like to give my sincere appreciation to my research advisor Dr. Luke Lee for his valuable guidance, warm encouragement, and support that made me complete this study successfully. His great vision and enthusiasm for the research have made me always motivated and do my best. Also, I would like to extend my sincere gratitude to my dissertation committee members, Dr. Randall Lee and Dr. Ming-Chiang Wu, for their advice, suggestions, and encouragement.

Also, I would like to acknowledge all BioPOETs lab members. It was a great honor to join BioPOETs, where I was able to build extensive knowledge in various fields through active discussions with excellent lab members. Especially, I would like to express thanks to my wonderful mentor, Dr. SoonGweon Hong, and seniors, Dr. Inhee Choi, Dr. Jihwan Song, and Dr. Jonghwan Lee, for their kind guidance and critical scientific advice that have helped me well-settled in the new environment and grow as what I am now. And, I also thank my fellow Dr. Byungrae Cho, for his support both mentally and academically.

Lastly, but most importantly, I want to express gratitude to my loving parents and brother, Seon Ki Song, Youngja Lee and Juwon Song, for their endless support and unconditional love that they offered to me. Without their support, none of this would have been possible. I sincerely appreciate it again.

Chapter 1

Introduction to Bioenergy

1.1. Importance of Bioenergy

Today, we are facing a worldwide energy crisis as well as the severe impacts of global warming caused by the unregulated consumption of fossil fuels [1]. As industrial development and population growth continue to skyrocket global energy demand, and as fossil fuel reserves decrease, we are facing more and more severe energy crises than ever before. According to the latest BP Statistical Review of World Energy (2019, 68th edition), fossil fuel reserves will be exhausted in 200 years (Fig. 1.1) [2]. More seriously, the accumulation of greenhouse gases emitted by the use of fossil fuels as energy sources has a catastrophic impact on the environment and our life [3]. The level of greenhouse gases has been quite constant over the past few thousand years until the industrial revolution. However, since the industrial revolution, atmospheric CO_2 has been increased by about 40 % owing to human activity. This significant change has historically taken about thousands of years, but it is now going on for decades (Fig. 1.2) [4-5]. Rapid increases in greenhouse gases are problematic because it promotes global warming, and it threatens all life on Earth by changing the climate more unpredictably and quickly than the living things can adapt. For instance, nowadays, the sea level is gradually rising as the ice sheet of Antarctica melts, and extreme weather such as deadly heatwaves, more intense storms, more prolonged rain, and drought are also becoming more frequent.

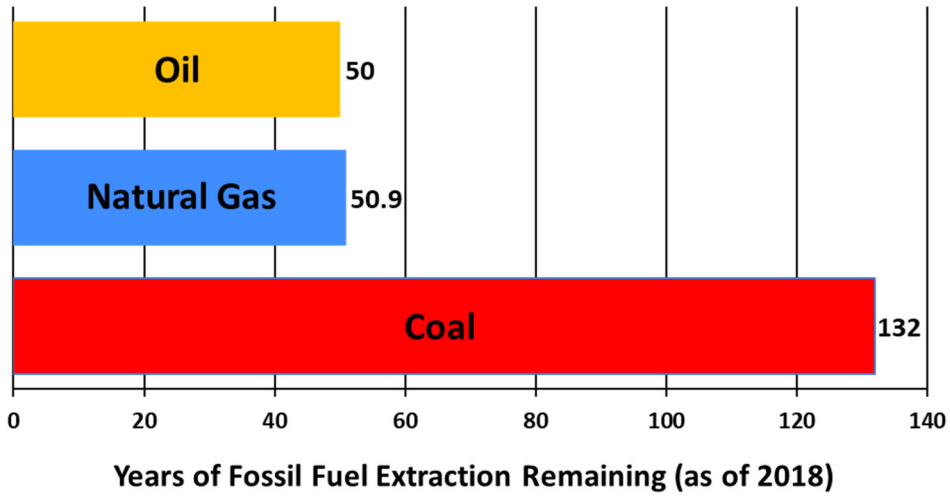

Figure 1.1. Estimated years of extraction remaining depending on fossil fuel types. Fossil fuels will run out in less than 200 years [2].

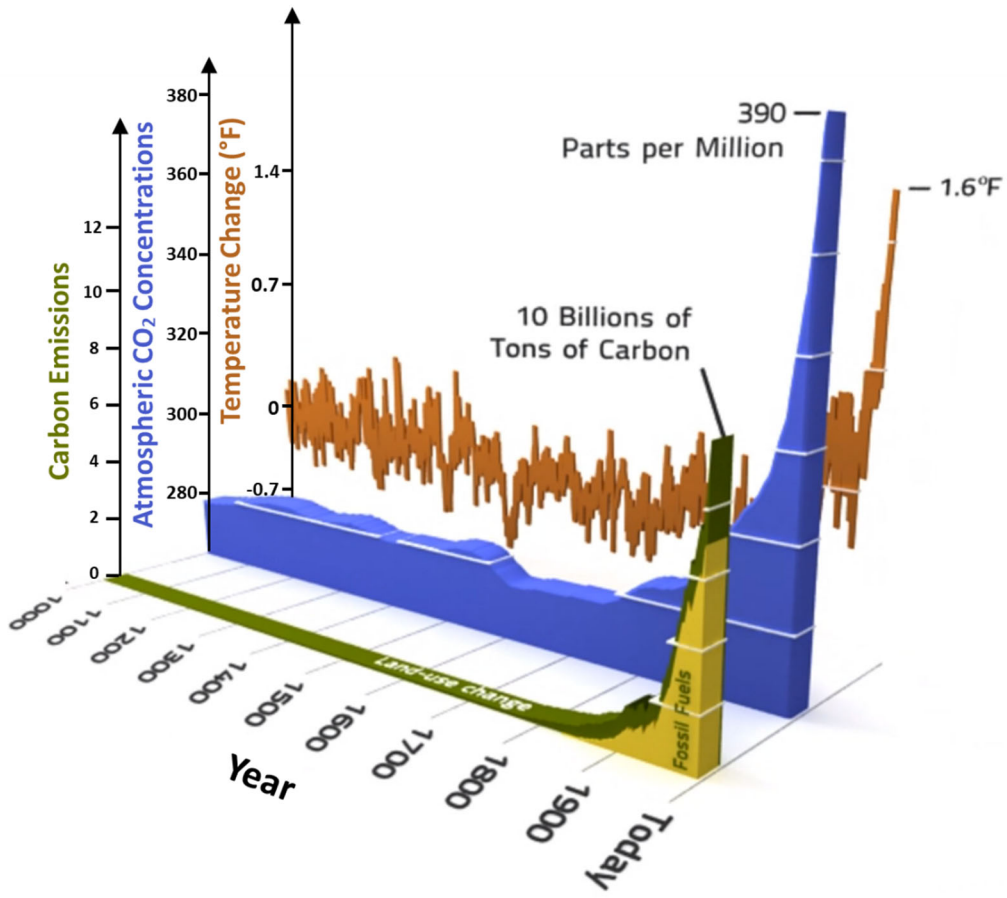

Figure 1.2. Trends of global temperatures and atmospheric carbon dioxide concentration. After the Industrial Revolution, the concentration of carbon dioxide in the atmosphere began to skyrocket, and the global temperature is also rising rapidly [4-5].

From this point of view, it is urgent to change energy sources from limited, environmentally destructive fossil fuels to renewable and environmentally friendly ones [6-7]. The major types of renewable and eco-friendly energy sources are solar, wind, hydroelectric power, geothermal, and biomass [8-9]. Among them, biomass, which stores sunlight in the form of chemical energy by capturing CO_2 in the atmosphere, is getting more attention as it is more reliable in many regions than other sources, and it can be converted into many different fuel sources [10-12]. The energy produced from biomass is called as bioenergy, and it has the following advantages;

1) Bioenergy is extremely renewable because its sources, biomass, can be continuously replenished.
2) Its net greenhouse gas emission is zero. The carbon emitted by the use of bioenergy is what was absorbed by the biomass during its life cycles.
3) Unlike petroleum-based fuels, which are major sources of land and water pollution, biofuels such as biodiesel and bioethanol are biodegradable and less poisonous.
4) It can be produced even with organic waste, resulting in savings of environmental and economic costs.

5) Local production of biomass and bioenergy can provide new employment and economic development opportunities for regional communities by replacing fossil fuels, which should be obtained through imports.
6) Unlike most other renewable energies, bioenergy can be generated simultaneously in two or more forms, such as heat and electricity, in a cogeneration plant.

Because of these advantages, bioenergy accounts for half of all renewable energy consumed in nowadays [13].

1.2. Resources of Bioenergy

Bioenergy has received increasing attention, and its proportion of global energy consumption is growing more and more. Also, bioenergy is becoming more diverse in terms of resource and end-use as it grows in size. In the past, bioenergy was limited to those derived from wood-based raw materials. However, today's bioenergy field utilizes almost all types of available biomass, ranging from organic waste to energy crops and microorganisms. Followings are the leading options of resource for bioenergy;

1.2.1 Food Crops

High-starch grains such as corn and sugar cane have been converted into ethanol since the 1970s [14]. They were considered as an excellent feedstock for bioethanol production due to its abundance, high-starch content, and ease of conversion to ethanol. The converted ethanol can be used with gasoline as a biofuel.

Despite a lot of advantages, currently, biofuels based on food crops are controversial due to rising food prices, competing for land use for food, low net energy yield, and environmental issue. As corn-based ethanol production has increased, corn prices have doubled from 2007 to 2015. Given that we are facing the food shortage issue, it is also a problem to use food crops as an energy source instead of food and obstruct real food cultivation by occupying fertile land.

Another problem is that the produced ethanol is highly water-soluble that the energy required to separate it from water is substantial. Even though the net energy yield of corn-based ethanol production has improved significantly over the past two decades, 50 % of the energy output is lost during the process of corn production, ethanol conversion, and ethanol separation yet [15]. Also, it is difficult to avoid criticism that a significant amount of fossil fuels is used to produce corn-based biofuels. Furthermore, from an environmental point of view, there are pollution problems on the surface and groundwater as a result of pesticide and nutrient used during crop production. While these issues have undergone many improvements with continued interest, there is still concern about bioenergy production using crops [16-17].

1.2.2 Plants

Another approach is using plants. High-lipid plants, which contain long-chain hydrocarbons, such as Jatropha, soybeans, and sunflowers, can be converted to biodiesel. Because

biodiesel is a very dense fuel, it has the advantage of being able to directly replace petroleum-based diesel fuel, which is ideal for transportation. Also, in terms of net energy yield, conversion of plants to biodiesel is more efficient than obtaining bioethanol from food crops because long-chain hydrocarbons, the primary components of biodiesel, are not mixed with water.

However, plant-based diesel production has the disadvantage of inherently low yield per unit area, resulting in a high cost of biodiesel production, so it cannot compete with petroleum-based diesel prices. They also cannot avoid blame for occupying the fertile land that should be used for food crops [18].

1.2.3 Cellulosic

Non-edible cellulosic biomass can be converted to bioethanol. Primary feedstocks for cellulosic ethanol are Switchgrass and Miscanthus, due to its high productivity per acre. Switchgrass can achieve over 500% more energy yield than the energy consumed during its production and management because it requires little inputs in production, such as fertilizers and herbicides. Also, their ability to grow fast in many types of lands, including non-productive land, makes them more versatile [19]. Because cellulosic ethanol uses non-edible parts and non-fertile areas, it has the advantages that it does not need to compete with food and does not increase the price of food. Although its primary raw materials are grasses, cellulosic ethanol can also be produced from paper pulp, municipal solid waste, and wood residues such as sawdust. These are considered as wastes, so when used, feedstock costs for cellulosic ethanol can be as low as free. Furthermore, in terms of the environment, cellulosic ethanol is much better than corn-based ethanol. As mentioned earlier, the production of grass does not require environmentally harmful chemicals such as herbicides. Also, after ethanol conversion from cellulosic, the remaining solid that has not been converted can be burned and used as an energy source for the conversion plant. According to the U.S. Department of Energy, the cellulosic ethanol reduces greenhouse gas emissions by 86 percent compared to gasoline and 52 percent less than corn-based ethanol [20].

However, cellulosic ethanol production is still in its initial stages. Even with the low feedstock price, it is hard to compete with gasoline due to the high cost of enzymes which are crucial to converting ethanol from cellulosic. Also, even though the feedstocks can be produced on land that is not fertile, for large-scale cellulosic ethanol production, it eventually competes with food crops for agricultural land.

1.2.4 Complex Organic Waste

Not only food crops and plants but also complex organic wastes and residues from agricultural, industrial, animal, and human can also be converted into bioenergy like biogas (*i.e.,* methane and hydrogen) and bioelectricity through specialized microorganisms [21]. Waste-based bioenergy accounts for about 10% of total bioenergy use in the United States in 2017 [16]. Using complex organic waste as a feedstock for bioenergy has lots of advantages. It can be converted to various types of energy, including biogas, liquid biofuels, and electricity. It does not compete with food crops. As the wastes are discarded unless they are used for bioenergy, the feedstock costs can be considered as zero. Also, because the residues often cause severe damage to the environment,

using it as an energy source without throwing it away is a great help to the environment. And the most significant advantage is that the water naturally leaves during the process of converting organic wastes into energy using microorganisms. It saves a lot of energy costs which is inevitable in corn or cellulosic grass-based ethanol production for separating the biofuel from water.

However, there are also some drawbacks to waste-based bioenergy production. Unlike food crops and cellulosic grasses, which consist of mostly glucose-based repeat units such as starch and cellulose, organic wastes include a complex mixture of carbohydrates, proteins, lipids, cellulose, lignin, etc. As the raw materials are more chemically complex, producing bioenergy from organic waste is more complicated and requires multiple steps than converting bioethanol from food crops or grasses. Generally, energy production from organic wastes takes place through microorganisms and consists of three steps: First, most organic wastes are complex solids and macromolecules, so they need to be broken down into bioavailable chemical forms (*e.g.*, carbohydrates, peptides, fatty acids) that can be absorbed by microorganisms. The second step is converting the bioavailable materials into simpler forms such as acetate and ethanol through fermentation. The last step is to produce CH_4, H_2, and electrons by using particular microorganisms. Waste-based bioenergy production has the disadvantages of requiring high energy/chemical costs. This is because the first step can only be accomplished by a combination of chemical, mechanical, and enzymatic attacks, such as high/low pH, high temperature, ultrasound, microwave, and hydrolytic enzyme. Odor also occurs during this process. The biggest drawback of this approach is that current technology can only convert about 50% of the energy value from organic wastes into bioavailable forms. If someone can find a way to convert complex chemical forms to bioavailable forms 100%, waste-based energy production will take more spotlight in the bioenergy field.

1.2.5 Phototrophic Microorganisms

In waste-based bioenergy production, microorganisms have been used as a means of converting raw materials into energy, but microorganisms themselves also can become energy sources. Phototrophic microorganisms such as microalgae and cyanobacteria use atmospheric carbon dioxide as a carbon source and convert solar energy into energy-rich hydrocarbon compounds. Using phototrophic organisms for bioenergy production offers many more advantages over using the other biomass [22-25].

First, they use fewer resources than human needs. According to the data on the World Bank and the U.S. Department of the Interior Bureau of Reclamation, only 11% of the world's land is arable, and only 0.5% of the earth’s water is available freshwater [16]. As the phototrophic microorganisms can grow in the desert or the ocean with wastewater and smoke coming from factories, they do not have to compete with the human for the resources that very limited but are indispensable for human survival such as fertile land, clean water, and air.

Second, they have super high productivity. Unlike other biomass such as crops and plants, the microorganisms can be harvested multiple times a year as they grow fast with a short life cycle, and they don't have a specific growing season. Thus, they have very high biofuel yield per unit area, which is up to 60 times higher than land-based plants, according to the U.S. Department of Energy [26]. Therefore, they also require much less land to produce the same amounts of biofuels than corn or soybeans. The Energy Department estimates that if soy biodiesel replaced all the

diesel in the U.S., it would require half the landmass of the U.S. to grow soybeans. However, if we are using algae fuel, it needs only 15,000 square miles, which is a few thousand miles larger than Maryland.

Third, the microorganisms can produce valuable co-products along with biofuels. The examples of high value-added co-products are carotenoids, polyunsaturated fatty acids (PUFAS), carbohydrates, omega-3 fatty acids, plastics (*e.g.*, PHA), proteins, and pigments such as astaxanthin and lutein. These products can be recovered and used in diverse industries such as nutraceutical, pharmaceutical, food, cosmetic, and chemical. In this way, by taking advantage of the various high value-added co-products, microorganism-based biofuel production can maximize the economic value of the whole process.

The comprehensive benefits of microorganisms as a bioenergy source, such as high productivity and the ability to produce precious co-products along with biofuels without competing with human resources, have been captured the enormous interest of researchers and entrepreneurs these days. However, despite these many advantages, the production of bioenergy using microorganisms requires more research to be more economically competitive.

1.3. Current Approaches and Limitations on Realizing Microalgae-based Bioenergy

As discussed in the above, there are various options for bioenergy sources. Among the options, phototrophic microorganisms are considered as strong candidates for next-generation biofuels [22-25]. This is because they are superior to terrestrial plants and other organic materials in many aspects, such as growth rates, photosynthetic conversion efficiency, diverse metabolic capability, and energy-rich hydrocarbon contents. In particular, as microalgae can accumulate much more lipid than other phototrophic microorganisms, such as cyanobacteria, we will focus on microalgae-based biofuel production in the remaining sections. Despite the many advantages, the commercialization of algae biofuel still has a lot of challenges to achieve cost-competitive fuels. The major challenges include strain selection, production management, harvesting, and fuel extraction as follows:

1.3.1 Strain Selection

Biofuels using microalgae are still economically less competitive with other cheap fossil-based fuels. The first step in increasing the economic competitiveness of algae-based biofuel for commercialization would be to select superior microalgae species that have the highest production efficiency in a short time with the lowest energy inputs.

Over 40,000 microalgae species have been considered for the selection of superior species, but it is only a fraction of the available ones on Earth [27-28]. The remaining species are currently being studied with a lot of time and effort. Besides, microalgae species are dramatically increasing in recent years due to the development of genetic engineering technologies and efforts to develop superior microalgae species. The problem is that the insertion of foreign genes into nuclear genes

as a way of developing superior species is mostly random in microalgae cells, resulting in a large variety of different clones, requiring extensive screening [29].

Also, the fact that the optimum species can vary depending on the conditions of the growing environment dramatically increases the screening works to identify the best species in each environment. Even though the microalgae species are the same, the efficiency of cell growth and bioenergy carrier production considerably vary depending on the surrounding environment such as light intensity, temperature, nutrients, pH and amount of available carbon dioxide [30-33]. In other words, the best performance microalgae species selected in particular 'A' environment can have completely different results in a 'B' environment. Therefore, there is a difficulty that the optimum species should be selected newly according to the local environmental conditions where the microalgae cells are to be grown.

Although a lot of human resources, time, and effort are being consumed on enormous screening works, the current research focuses exclusively on the development of new microalgae species. Unfortunately, little effort is being made to reduce the energies involved in screening. As the selection of superior species plays the most crucial role in the successful biofuel industrialization using microalgae, there is an urgent need for novel screening methods that scan such a vast pool of microalgae species quickly and easily to select superior ones.

1.3.2 Production Management

In agriculture, timely management (*e.g.*, seeding, nutrient supply, pesticide treatment, and harvesting) is a critical factor directly related to yield. If it is poorly managed not on time, the production rate will be dropped significantly. For example, if you miss the timing of providing nourishment or do not harvest even after its maturation, crops may be in poor condition, and the yields will be dropped significantly. In the worst case, both the resources and time spent on cultivation can come to nothing. Therefore, monitoring of crop conditions for timely management is one of the critical factors in crop production.

The same goes for microalgae farming. The timely management is even more critical in the case of microalgae due to the shorter time frames of its cultivation. Microalgae have short cellular cycles so that the level of growth and bioenergy carrier production changes rapidly even in few hours along with shifts in the surrounding environment, requiring more frequent and careful monitoring for the timely management. Although commercialized sensors can be used to monitor physicochemical variables, such as pH, temperature, and photon flux density, monitoring of the most critical biological variables relies on methods that are currently applicable only for laboratory scale.

In general, the measurement of optical properties (*i.e.*, measuring fluorescence and absorbance of visible or infrared light) is considered as the most promising way to use in the field because it requires relatively inexpensive equipment and can estimate biological quantities (*i.e.*, cell number and concentration of lipid or pigment). Thus, attempts have been made recently to implement these optical measurement methods into actual microalgae culture sites rather than

laboratories. However, these optical-based methods cannot readily be adapted to production monitoring because it has the disadvantages of having too short dynamic range (*i.e.*, not measurable if the cell concentration is too low, or dilution is required if the cell concentration is too high) [34] and requiring additional sample processing step (*e.g.*, cell staining with dye) [35].

Therefore, for the commercialization of microalgae-based biofuels, it is urgent to develop inexpensive, easy, and reliable real-time microalgae monitoring technology that can be used in the real-field.

1.3.3 Harvesting

When microalgal growth and bioenergy carrier production reach optimal stages, microalgae cells should be harvested and prepared for downstream processing. As the microalgae cells are grown in water, it must be separated from the liquid. Its small size and density similar to water makes the separation process difficult and expensive [36]. Generally, microalgae harvesting requires one or more steps of solid-liquid separation, an energy-intensive process that takes 20-30% of the total biofuel production cost [37]. This excessive energy consumption must be reduced before entering mass production because it increases overall production costs and hinders commercialization.

A typical microalgal harvesting method is centrifugation. It is the fastest and most reliable harvesting method regardless of microalgae species but has the fatal drawback of being too high in energy consumption and operational costs to handle bulk volumes. Therefore, as an alternative to expensive centrifugation, many harvesting strategies, including filtration, sedimentation, flotation, flocculation, electrocoagulation, magnetic separation, and ultrasonic separation, have been studied and are still under development [38-40]. However, most methods are still expensive or even though some approaches are cost-effective some extent but have problems in large-scale applications as follows: 1) highly dependent on algal species, 2) slow, 3) unreliable, 4) low recovery rates, or 5) difficulty in obtaining a pure biomass due to the usage of other additives (*e.g.*, chemical, metal anion, magnetic particles). Sometimes, combinations of different methods (*e.g.*, pre-concentration via auto-flocculation and followed by dewatering through centrifugation) are used to take benefits of each technique. However, it is still not good enough to implement in the real field on a large-scale. Thus, the novel harvesting methods, which can reduce the costs dramatically without the problems mentioned earlier, are desperately required in realizing commercialization.

1.3.4 Energy-carrier Extraction

Another bottleneck in the commercialization of algae-based biofuels is lipid extraction from harvested and dehydrated microalgae [41]. Unlike extracting lipids from grains, lipid extraction from microalgae is relatively tough due to the thick cell walls. Besides, the choice of lipid extraction technology is tricky because it depends on various factors, including algal species, growth status, and characteristics of target components to be extracted [42].

Essential factors in choosing a lipid extraction method are cost, efficiency, purity, ease of handling, and applicability to large scales. Commonly considered methods for extracting lipids from microalgae are as follows: presses, solvent extraction, enzymatic extraction, osmotic shock, ultrasonic-assisted extraction, microwave-assisted extraction, and supercritical CO_2 fluid extraction [43-45]. Among these methods, osmotic shock and supercritical carbon dioxide methods are not suitable for commercial use because of their high operating costs. Enzymatic extraction is also not ideal for a large scale due to the relatively expensive cost of enzymes. Presses, supercritical CO_2 fluid extraction, and ultrasonic-assisted extraction are also can only be used on laboratory scales due to the shortcomings of slow processing and difficulties in scale-up. The solvent-assisted extraction, a widely used method on a laboratory scale owing to its low cost and easiness, is easy to be considered as the most promising way to use also in the field application. However, still, it is not ideal for commercial-scale applications in that it requires a significant amount of chemical solvents for efficient lipid extraction, and substantial additional energy consumed for solvent recovery. The toxicity and stability of solvents are also problematic. Thus, further optimization or novel approaches of lipid extraction technologies are urgently required before going into the commercial scale.

1.4. Outline of Thesis

Because of the advantages stated above, we've focused only on the microalgae-based biofuel among various types of bioenergy. To take a step closer to realizing microalgae-based biofuel as a next-generation energy, this thesis will discuss only the first two aspects of the above mentioned technical limitations on the commercialization as follows; (1) how we can screen superior microalgae species faster and easier, and (2) how we can monitor the microalgae cultivation process effectively in the field in real-time. Particularly the thesis contains three categories of (1) Label-free Density Difference Amplification-based Cell Sorting, (2) Photonic Cavity for Rapid Microalgae Strain Screening, and (3) Photocurrent-based Microalgal Farming Monitoring.

In the second chapter, we will discuss how to easily sort out the best microalgal strains that accumulate the largest amount of lipids using BioMEMS technology. As lipids are lighter than water, the density of each microalgae species will vary depending on the amount of lipids accumulated in their bodies. The sudden geometric change of the microfluid channel causes a hydraulic jump of cells passing through the channel, which facilitates separation by cell density, making it easy to select superior species (*i.e.*, lightest one) without additional labeling processes. In general, the selection of superior species has been made through observation of the entire process of cell growth and lipid accumulation in cells, which requires a long time and effort. However, the buoyancy-based method, which will be addressed in this paper, means a lot in that it is possible to select a superior species quickly and easily without those kinds of the whole process.

The third chapter will discuss how optics can help accelerate microalgae growth and lipid production, leading to rapid screening. As microalgae are photosynthetic organisms, the light illumination plays a crucial role in its growth, and production of energy carriers. In the third chapter, we will present a hemispherical cavity embedded with metal nanostructures, as a compact photobioreactor for rapid microalgae screening. We will use the inherent optical property of the

metal nanostructures that scatter specific wavelengths favored by microalgae, which will increase the photosynthetic efficiency of microalgae, resulting in shorter screening times through rapid growth. Besides, the additional optical property (*i.e.*, light focusing) provided by the geometry of a hemispherical cavity will help rapid screening even with naked-eye by facilitating rapid growth through cell gathering and cell-cell interactions.

Finally, the fourth chapter will cover how electronics can be applied to monitor microalgae. This approach is different from other existing methods in that microalgae monitoring has been mostly optical-based ones. We will introduce a novel electrical sensor that can effectively monitor microalgae in the real field, utilizing photocurrent derived from the channelrhodopsin, a unique feature of microalgae. This new method overcomes the limitations in terms of the field application that other existing approaches have not solved in that it can monitor microalgae in real-time in-situ even with low cost without the need for additional sample processing steps.

Reference

[1] Curtis, F., Peak globalization: Climate change, oil depletion and global trade. *Ecological Economics* **2009,** *69* (2), 427-434.

[2] https://www.bp.com/content/dam/bp/business-sites/en/global/corporate/pdfs/energy-economics/statistical-review/bp-stats-review-2019-full-report.pdf

[3] Patz, J.A., Gibbs, H.K., Foley, J.A., Climate Change and Global Health: Quantifying a Growing Ethical Crisis. *EcoHealth* **2007**, 4: 397.

[4] Peter, S. C., Reduction of CO2 to Chemicals and Fuels: A Solution to Global Warming and Energy Crisis. *ACS Energy Letters* **2018,** *3* (7), 1557-1561.

[5] https://www.climatecommunication.org/climate/the-problem/

[6] Arent, D. J.; Wise, A.; Gelman, R., The status and prospects of renewable energy for combating global warming. *Energy Economics* **2011,** *33* (4), 584-593.

[7] Jennings, P., New directions in renewable energy education. *Renewable Energy* **2009,** *34* (2), 435-439.

[8] Bull, S. R., Renewable energy today and tomorrow. *Proceedings of the IEEE* **2001,** *89* (8), 1216-1226.

[9] Lund, H., Renewable energy strategies for sustainable development. *Energy* **2007,** *32* (6), 912-919.

[10] Balat, M.; Ayar, G., Biomass Energy in the World, Use of Biomass and Potential Trends. *Energy Sources* **2005,** *27* (10), 931-940.

[11] Demirbaş, A., Biomass resource facilities and biomass conversion processing for fuels and chemicals. *Energy Conversion and Management* **2001,** *42* (11), 1357-1378.

[12] McKendry, P., Energy production from biomass (part 1): overview of biomass. *Bioresource Technology* **2002,** *83* (1), 37-46.

[13] https://www.iea.org/renewables2018/ (accessed July 2018).

[14] Goldemberg, J., Ethanol for a Sustainable Energy Future. *Science* **2007,** *315* (5813), 808.

[15] Rittmann, B. E., Opportunities for renewable bioenergy using microorganisms. *Biotechnology and Bioengineering* **2008,** *100* (2), 203-212.

[1] https://www.eia.gov/energyexplained/index.php?page=biomass_home.
[2] https://www.usda.gov/oce/reports/energy/2015EnergyBalanceCornEthanol.pdf
[3] Hood, E. E., Plant-based biofuels. *F1000Res* **2016,** *5*, F1000 Faculty Rev-185.
[4] Tilman, D.; Hill, J.; Lehman, C., Carbon-Negative Biofuels from Low-Input High-Diversity Grassland Biomass. *Science* **2006,** *314* (5805), 1598.
[5] https://www.energy.gov/sites/prod/files/edg/news/archives/documents/Myths_and_Facts.pdf
[6] Cu, T. T. T.; Nguyen, T. X.; Triolo, J. M.; Pedersen, L.; Le, V. D.; Le, P. D.; Sommer, S. G., Biogas production from vietnamese animal manure, plant residues and organic waste: influence of biomass composition on methane yield. *Asian-Australas J Anim Sci* **2015,** *28* (2), 280-289.
[7] Baicha, Z.; Salar-García, M. J.; Ortiz-Martínez, V. M.; Hernández-Fernández, F. J.; de los Ríos, A. P.; Labjar, N.; Lotfi, E.; Elmahi, M., A critical review on microalgae as an alternative source for bioenergy production: A promising low cost substrate for microbial fuel cells. *Fuel Processing Technology* **2016,** *154*, 104-116.
[8] Menetrez, M. Y., An Overview of Algae Biofuel Production and Potential Environmental Impact. *Environmental Science & Technology* **2012,** *46* (13), 7073-7085.
[9] Rodionova, M. V.; Poudyal, R. S.; Tiwari, I.; Voloshin, R. A.; Zharmukhamedov, S. K.; Nam, H. G.; Zayadan, B. K.; Bruce, B. D.; Hou, H. J. M.; Allakhverdiev, S. I., Biofuel production: Challenges and opportunities. *International Journal of Hydrogen Energy* **2017,** *42* (12), 8450-8461.
[10] Singh, A. K.; Singh, M. P., Importance of algae as a potential source of biofuel. (1165-158X (Electronic)).
[11] https://www.energy.gov/eere/videos/energy-101-algae-fuel
[12] Guiry, M. D., HOW MANY SPECIES OF ALGAE ARE THERE? *Journal of Phycology* **2012,** *48* (5), 1057-1063.
[13] Stark, M.; O'Gara, I., An Introduction to Photosynthetic Microalgae. *Disruptive Science and Technology* **2012,** *1* (2), 65-67.
[14] Doron, L.; Segal, N. a.; Shapira, M., Transgene Expression in Microalgae-From Tools to Applications. *Front Plant Sci* **2016,** *7*, 505-505.
[15] Abo Bodjui, O.; Odey Emmanuel, A.; Bakayoko, M.; Kalakodio, L., Microalgae to biofuels production: a review on cultivation, application and renewable energy. In *Reviews on Environmental Health*, 2019; Vol. 34, p 91.
[16] Gatamaneni, B. L.; Orsat, V.; Lefsrud, M., Factors Affecting Growth of Various Microalgal Species. *Environmental Engineering Science* **2018,** *35* (10), 1037-1048.
[17] Juneja, A.; Ceballos, M. R.; Murthy, S. G., Effects of Environmental Factors and Nutrient Availability on the Biochemical Composition of Algae for Biofuels Production: A Review. *Energies* **2013,** *6* (9).
[18] Mata, T. M.; Martins, A. A.; Caetano, N. S., Microalgae for biodiesel production and other applications: A review. *Renewable and Sustainable Energy Reviews* **2010,** *14* (1), 217-232.
[19] Benavides, M.; Mailier, J.; Hantson, A.-L.; Muñoz, G.; Vargas, A.; Van Impe, J.; Vande Wouwer, A., Design and Test of a Low-Cost RGB Sensor for Online Measurement of Microalgae Concentration within a Photo-Bioreactor. *Sensors* **2015,** *15* (3).
[20] Natunen K. (2017) Monitoring Microalgal Neutral Lipid Accumulation with Nile Red. In: . Methods in Molecular Biology. Humana Press

[21] Milledge, J.J. & Heaven, S. Rev Environ Sci Biotechnol (2013) 12: 165. https://doi.org/10.1007/s11157-012-9301-z
[22] Molina Grima, E.; Belarbi, E. H.; Acién Fernández, F. G.; Robles Medina, A.; Chisti, Y., Recovery of microalgal biomass and metabolites: process options and economics. *Biotechnology Advances* **2003,** *20* (7), 491-515.
[23] Greenwell, H. C.; Laurens, L. M. L.; Shields, R. J.; Lovitt, R. W.; Flynn, K. J., Placing microalgae on the biofuels priority list: a review of the technological challenges. *J R Soc Interface* **2010,** *7* (46), 703-726.
[24] Uduman, N.; Qi, Y.; Danquah, M. K.; Forde, G. M.; Hoadley, A., Dewatering of microalgal cultures: A major bottleneck to algae-based fuels. *Journal of Renewable and Sustainable Energy* **2010,** *2* (1), 012701.
[25] Vandamme, D.; Foubert, I.; Muylaert, K., Flocculation as a low-cost method for harvesting microalgae for bulk biomass production. *Trends in Biotechnology* **2013,** *31* (4), 233-239.
[26] Khan, M. I.; Shin, J. H.; Kim, J. D., The promising future of microalgae: current status, challenges, and optimization of a sustainable and renewable industry for biofuels, feed, and other products. *Microb Cell Fact* **2018,** *17* (1), 36-36.
[27] Li, Y.; Ghasemi Naghdi, F.; Garg, S.; Adarme-Vega, T. C.; Thurecht, K. J.; Ghafor, W. A.; Tannock, S.; Schenk, P. M., A comparative study: the impact of different lipid extraction methods on current microalgal lipid research. *Microb Cell Fact* **2014,** *13* (1), 14.
[28] Araujo, G. S.; Matos, L. J. B. L.; Fernandes, J. O.; Cartaxo, S. J. M.; Gonçalves, L. R. B.; Fernandes, F. A. N.; Farias, W. R. L., Extraction of lipids from microalgae by ultrasound application: Prospection of the optimal extraction method. *Ultrasonics Sonochemistry* **2013,** *20* (1), 95-98.
[29] Cheng, C.-H.; Du, T.-B.; Pi, H.-C.; Jang, S.-M.; Lin, Y.-H.; Lee, H.-T., Comparative study of lipid extraction from microalgae by organic solvent and supercritical CO2. *Bioresource Technology* **2011,** *102* (21), 10151-10153.
[30] Ranjith Kumar, R.; Hanumantha Rao, P.; Arumugam, M., Lipid Extraction Methods from Microalgae: A Comprehensive Review. *Frontiers in Energy Research* **2015,** *2*, 61.

Chapter 2

Label-free Density Difference Amplification-based Cell Sorting (dDACS)

Effective screening of individual microalgae cells is one of the major prerequisites to maximize biofuel production: it is needed from selecting profitable strains to collecting cells matured for byproduct harvesting. To date, most of the separation techniques, with the aid of external forces, have exploited either the difference in inherent physical properties (*e.g.*, a size and dielectric property) between different kinds of cells or labeling to induce the difference between them. However, these methods are limited when separating from cells of the same type or cells with similar size and dielectric properties. In this chapter, we will present a novel label-free microfluidic device that is capable of separating cells according to a subtle difference in density without any external forces [1]. The conceptual microfluidic design consists of an inlet, separation chamber, and multiple outlets. Incoming cells experience gravity, buoyancy, and drag forces in the separation chamber, and depending on their densities, both the height and distance that each cell can reach in the chamber are different, allowing us to separate the cells into the multiple outlets. The separation behavior of cells with various densities has been studied systematically according to the channel height ratio of the inlet and separation chambers and the Reynolds number. Numerical simulation shows that as the ratio of channel height increases, the height difference between only lighter cells close to the density of the surrounding liquid increases. Whereas reducing the Reynolds number can amplify the height difference between the cells regardless of their density.

2.1. Introduction

Isolating specific cells of interest from a heterogeneous or homogeneous mixture is considered as a critical step in a wide range of applications. For example, diagnosis and therapy of Human Immunodeficiency Virus (HIV) rely on the successful separation of particular white blood cell subset, CD4+ T cell, from whole blood samples [2-3]. Similarly, efficient separation and sorting of circulating tumor cells (CTCs) from whole blood samples have a significant meaning since they are highly correlated with early diagnosis which prevents cancer metastasis and poor prognosis [4-5]. Recently, separation of lipid rich microalgae is drawing attention in the field of energy harvesting since they are being spotlighted as the upcoming alternative energy source [6].

To date, separation techniques have been exploited the difference in either size or intrinsic properties (e.g., dielectric, electrical charge, magnetic, etc.) between different kinds of cells with the aid of external forces or labeling [7-13]. For example, acoustophoresis focuses particles larger than a desired size into the center of the channel by creating low pressure nodes with an aid of acoustic forces from ultrasonic standing waves [14-16]. In fluorescence-activated cell sorter (FACS), individual cells are identified via specific antibodies labeled with fluorescent molecules and sorted by applying electric charge when it reaches the break off point [7-8]. These methods; however, have some drawbacks in terms of cell viability since external forces (e.g., high acoustic

pressures, joule heating in electrophoresis, shear stress in centrifuging, etc.) or labeling can cause damage to biological cells [17-19]. More importantly, these methods are limited in separating specific cells from cells with similar size and charge; recently the later has strong implications in solar-energy harvesting with cells.

Here we designed a novel microfluidic system that allows separating cells with the same size and charge according to the density difference without any external forces or labeling.

2.2. Concept of the dDACS

Figure 2.1 illustrates our proposed method and its mechanism for the separation. The microfluidic design consists of an inlet, a separation chamber, and multiple outlets. Incoming cells experience gravity (F_G), buoyancy (F_B), and drag (F_D) forces in the separation chamber, and net force acted on the cells can be described as

$$F = F_G + F_B + F_D \quad \text{(eq. 2.1)}$$

Each force is defined as $F_G = -\rho_p V g, F_B = \rho_f V g, F_D = C_D A_p \rho_f v^2/2$, respectively.

As the net force contains density terms, the particles with different densities will experience different net force and have different positions. The height (H) and distance (D) that each particle can travel within the chamber can be analytically derived as follow,

$$H(t) = y_0 + \left(\frac{\rho_p V_p}{\alpha}\right)\left(\ln\left|\sqrt{\frac{v_{y0}^2}{\beta}+1}\right| - \ln\left|\sec\left(\left(\frac{\alpha\sqrt{\beta}}{\rho_p V_p}\right)t + \tan^{-1}\left(v_y/\sqrt{\beta}\right)\right)\right|\right), \quad \text{(eq. 2.2)}$$

$$D(t) = x_0 + \left(\frac{\rho_p V_p}{\alpha}\right)\left(\ln\left|\rho_p V_p\right| - \ln\left|\rho_p V_p - \alpha v_{x0} t\right|\right), \quad \text{(eq. 2.3)}$$

where α and β represent $C_D A_p \rho_f/2$ and $(\rho_p - \rho_f)V_p g/\alpha$, respectively. v_o, C_D, A_p, ρ_f, ρ_p, and V_p are fluid flow velocity at the entrance in the chamber, the drag coefficient, cross-sectional area of a particle, the fluid density, the particle density, and the particle volume, respectively.

The proposed microfluidic system comprising a separation chamber can achieve greater H differences of cells having different densities during the same D as compared to a microfluidic system without a separation chamber. As shown in Figure 2.1(b), tangential angle (θ) of F_D acting on the cells have significantly different characteristic along the y-direction depending on the channel designs (i.e., uniform channel height (left), gradual channel expansion (middle) and sudden channel expansion (right)).

Our proposed design, sudden channel expansion, creates a sudden vertical displacement of the fluid, which leads to a large tangential angle (θ) of the F_D at the entrance of the separation chamber. Thus, the change in y-directional net force acting on cells at the entrance of the separation chamber by the contribution of the F_D is relatively large compared to the other two cases, which leads to a noticeable rearrangement of cell's y-directional position in the separation chamber. Moreover, the relative contribution of F_D to the y-directional net force acting on the cell varies depending on the cell density even within a separation chamber of the same design. For light cells whose density is close to that of the surrounding liquid, the contribution of F_D in the y-direction is

large enough to offset the F_G which is the opposite direction to F_D. But the heavy cells are less affected by an additional contribution of F_D due to the relatively large F_G.

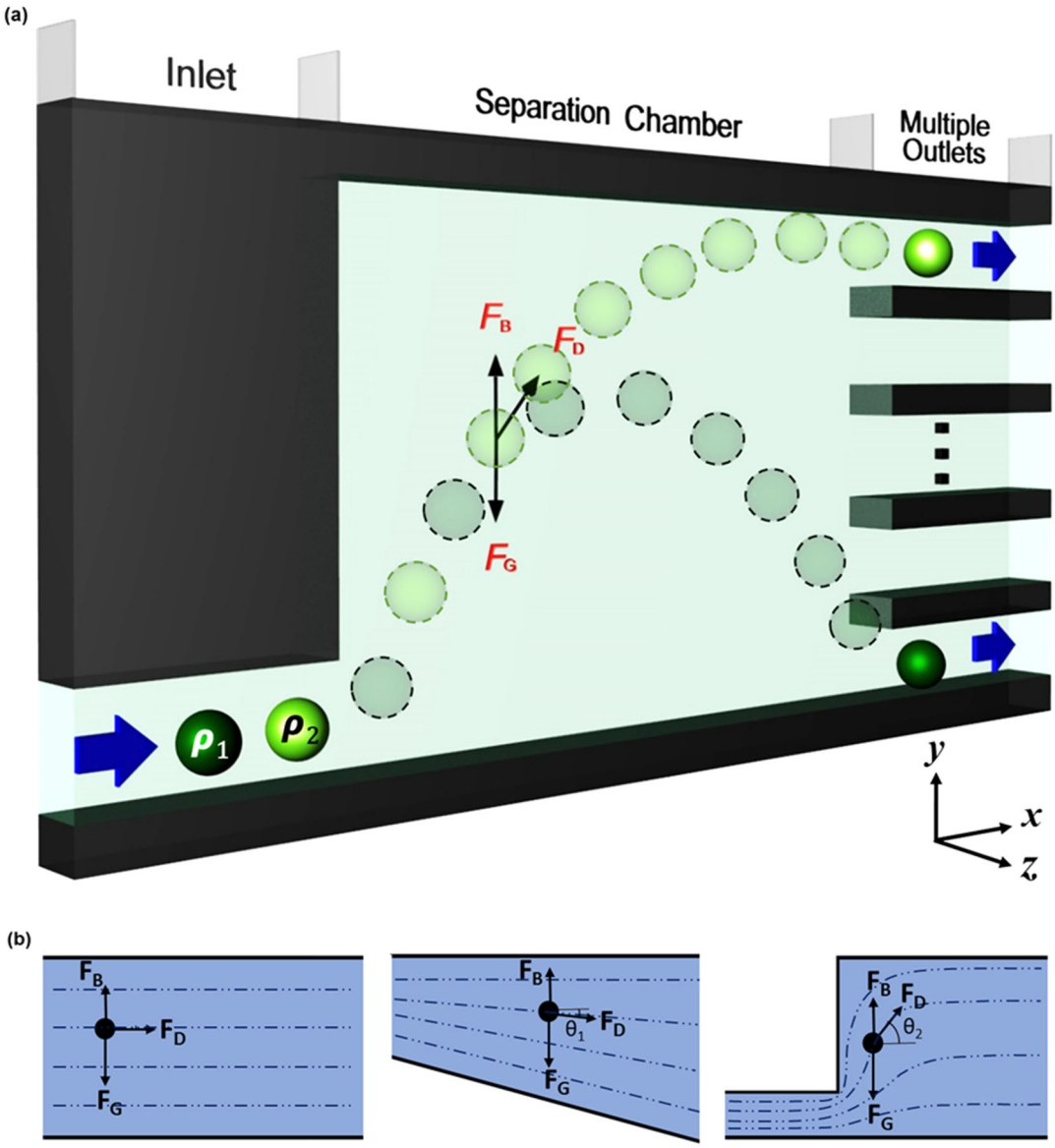

Figure 2.1. Schematic illustration of label-free density difference amplification-based cell sorting (dDACS), which exploits differences in the densities ($\rho_1 > \rho_2$) of cells with similar diameters (d) and charge. **(A)** The conceptual microfluidic design consists of an inlet, a separation chamber (hydraulic jump cavity), and multiple outlets. Incoming cells experience gravity (F_G), buoyancy (F_B), and drag (F_D) forces in the separation chamber, and depending on their densities, the height (H) and distance (D) that each cell is able to reach will be different, allowing the cells to be separated into multiple outlets. **(B)** Possible microfluidic channel configurations for density-based separation: Uniform channel height (left), gradual channel expansion (middle), and hydraulic jump cavity with sudden channel expansion (right). The height difference between cells with different densities can be amplified by the sudden channel expansion compared to the other two cases due to the relatively large tangential angle, θ of F_D ($|\theta_1| << |\theta_2|$).

As a result, the height difference between cells with different densities can be amplified in the sudden expanding separation chamber due to the relatively increased contribution of F_D to the y-directional net force as the cell density decreases. Consequentially, in the sudden expanding separation chamber, both the H and D of the cell vary greatly depending on their density, so that the cells of different densities are separated into distinct outlets.

2.3. Density-dependent Separation Behaviors in the Microfluidic System

In order to analyze the jump characteristics of the cells according to the density difference, the jump height (H) and the travel distance (D) are systematically investigated. The variation of cell density is selected from 1.1 g/cm^3 to 2.0 g/cm^3 with the increase of 0.1 g/cm^3 density. These values are quite reasonable because the difference in density among micro-organisms has been reported about 0.2 g/cm^3, according to their internal cellular context [20].

Figure 2.2(a) shows the trajectory of 100 cells of identical density. The jump height and travel distance are varied according to the position of cells at the inlet. Thus, the maximum jump height, H_{max}, and the maximum travel distance, D_{max}, are defined according to the investigation on the jump height and the travel distance of 100 cells which are injected from different positions. Also, the H_{max} and D_{max} are analytically derived from the eq. 2.2 and 2.3 and those are approximated as

$$H^{\max} \approx y_0 + \left(v_0^y\right)^2 / 2(1-\rho)g \text{ , and}$$

$$D^{\max} \approx x_0 + \left\{(v_0^x)^2 / (1-\rho)g\right\}\left\{1-\sqrt{2\left(\rho_p-\rho_f\right)Vg / C_D A_p \rho_f (v_0^x)^2}\right\}, \text{ where } \rho = \rho_f / \rho_p .$$

Figure 2.2(b) represents each H_{max} and D_{max} of cells concerning 10 kinds of different densities. The smaller density particle shows the higher H_{max} and the longer D_{max}. The H_{max} according to the cell density difference is shown in Figure 2.2(c). The H_{max} at the Re = 0.5, for example, cells with a density of 1.1 g/cm^3 and 1.2 g/cm^3, are 2206 μm and 2166 μm, respectively. The difference of H_{max} between the two cells (ΔH_{max}) is 40 μm. As Re decreases, ΔH_{max} tends to increase. For example, the ΔH_{max} between cells having a density of 1.1 g/cm^3 and 1.2 g/cm^3 is increased to 187 μm as the Re decreases to 0.1, while that is decreased to 14 μm as the Re increase to 1.0. The ΔH_{max} between cells with a density of 1.1 g/cm^3 and 2.0 g/cm^3 is monotonously increased from 258 μm to 1384 μm with a decrease of Re from 1.0 to 0.1. The H_{max} is determined by the three different forces, $F_{gravity}$, $F_{buoyancy}$, and F_{drag}. The effect of F_{drag} (i.e., $C_D A_p \rho_f \boldsymbol{v}^2/2$) is increased with the increase of flow velocity; thus, the H_{max} is increased. When the flow velocity is decreased, the effect of $F_{gravity}$ and $F_{buoyancy}$ (i.e., $-(\rho_p - \rho_f)Vg$) is relatively enhanced in determining the H_{max}, because the effect of F_{drag} is rapidly decreased proportionally to the square of flow velocity.

Thus, the H_{max} reacts more sensitively to change in the density difference, (ρ_p - ρ_f), as the Re is decreased, resulting in ΔH_{max} according to the density difference is remarkably represented. Notably, ΔH_{max} shows clearly different tendency due to the effect of density difference with the fluid, even the density difference between the two cells is same. For instance, the ΔH_{max} between the cells having a density of 1.1 g/cm^3 and 1.2 g/cm^3 is 187 μm, while that between the cells with a density of 1.9 g/cm^3 and 2.0 g/cm^3 is 85 μm. Furthermore, the cells which have smaller density difference with the fluid such as the 1.1 g/cm^3 to 1.4 g/cm^3 shows the lager ΔH_{max} than the cells

which have larger density difference with the fluid such as 1.5 g/cm^3 to 2.0 g/cm^3. It can be explained with the analytically approximated ΔH_{max} as $\left\{\left(v_0^y\right)^2/2g\right\}\left\{\left(\rho_{p2}-\rho_{p2}\right)/\left(\rho_1^{'}-1\right)\left(\rho_2^{'}-1\right)\right\}$, where ρ' is ρ_p/ρ_f. When the density difference between the two cells is constant, the less density difference with the fluid which means the smaller ρ' makes the more increased ΔH_{max}. Thus, the minimizing of density difference with the fluid allows effective separation of particles.

Figure 2.2(d) shows the D_{max} according to the cell density difference. The D_{max} at the Re=0.1, for example, of the cells having a density of 1.1 g/cm^3 and 1.2 g/cm^3, is 29130 μm and 14287 μm, respectively. The graph shows that the D_{max} is rapidly decreased as the density of cell increases. The D_{max} is analytically approximated as

$$D^{\max} \approx x_0 + \left\{(v_0^x)^2/(1-\rho)g\right\}\left\{1-\sqrt{2\left(\rho_p-\rho_f\right)Vg/C_D A_p \rho_f (v_0^x)^2}\right\}.$$

The first bracket, $\{(v_0^x)^2/(1-\rho)g\}$ represents the effect of forces ratio, $F_{\text{ratio}} = F_{\text{drag}}^x / F_{\text{gravity}} - F_{\text{buoyancy}}$ and the second bracket, $\left\{1-\sqrt{2\left(\rho_p-\rho_f\right)Vg/C_D A_p \rho_f (v_0^x)^2}\right\}$ can be rewritten as $\left\{1-\sqrt{F_{\text{gravity}}-F_{\text{buoyancy}}/F_{\text{drag}}^x}\right\}$. Thus, the D_{max} and the forces ratio have a relation as $D^{\max} \propto F_{ratio}(1-\sqrt{1/F_{ratio}})$. Both of F_{ratio} and $(1-\sqrt{1/F_{ratio}})$ are increased as the density difference between the cell and the fluid decreases, because the $F_{\text{gravity}} - F_{\text{buoyancy}}$ is decreased with the smaller density difference. As a result, D_{max} is rapidly increased as the density difference between those decreases.

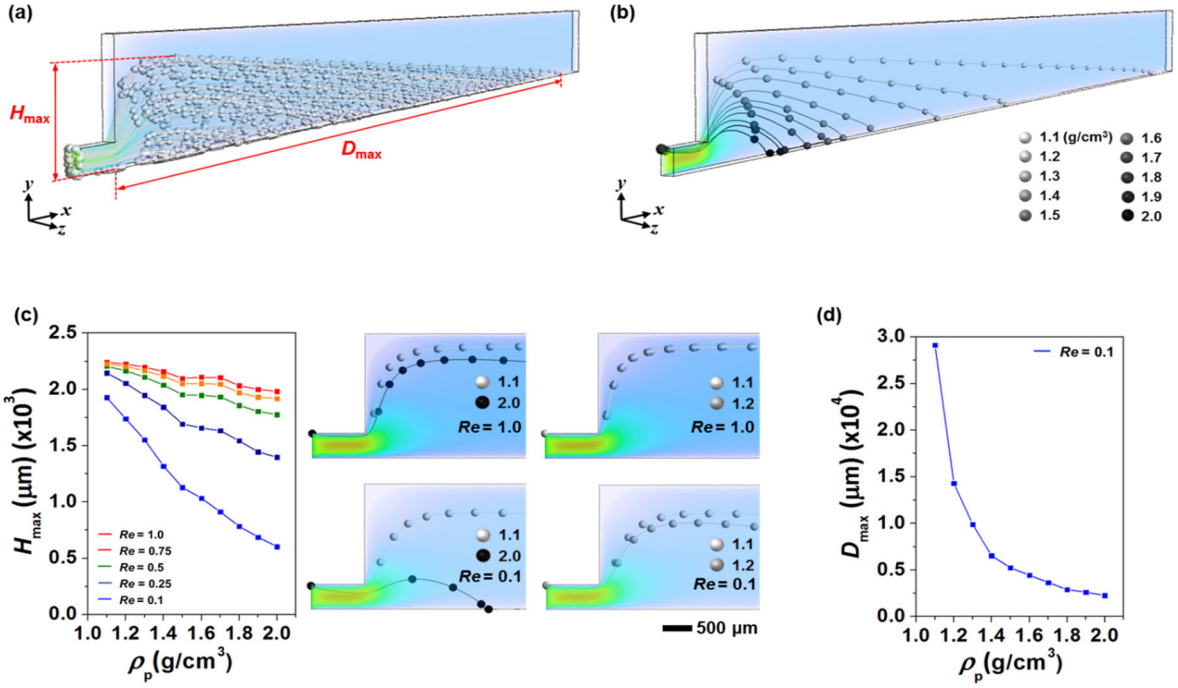

Figure 2.2. Microfluidic cell separation with respect to Reynolds number (Re). **(A)** Trajectories in the separation chamber of a hundred cells with the same density starting from inlet positions chosen arbitrarily in order to investigate the effect of the inlet positions on the maxima of the height ($H_{\max}$) and distance ($D_{\max}$) prior to further simulation. **(B)** Representative trajectories of cells having different densities from 1.1 to 2.0 g/cm^3. **(C)** The maximum height ($H_{\max}$) of each cell with respect to Re. **(D)** Representative maximum distance ($D_{\max}$) of each cell at Re = 0.1.

2.4. Geometry-dependent Separation Behaviors in the Microfluidic System

Next, in order to analyze the cell separation behavior according to the microfluidic geometry, the effect of geometric ratio, h_c/h_i for the H_{max} is investigated as shown in Figure 2.3. Interestingly, the result shows the obviously different tendency according to the cell density. For instance, the H_{max} of cell having a density of 1.1 g/cm^3 is increased from 1927 μm to 6475 μm as the h_c/h_i increases from 5 to 20, while that of 1.9 g/cm^3 shows small change about 30 μm from the 701 μm to 734 μm with the identical geometric ration changes. As similar with the D_{max}, the analytically approximated $H^{\max} \approx y_0 + \left(v_0^y\right)^2 / 2(1-\rho)g$ shows the relation with the forces as $H^{\max} \propto F_{\text{drag}}^y / F_{\text{gravity}} - F_{\text{buoyancy}}$. It means that the H_{max} reacts more sensitively to change in the F_{drag} as $F_{\text{gravity}} - F_{\text{buoyancy}}$ is reduced. The cell of 1.1 g/cm^3 has an about 10 times smaller $F_{\text{gravity}} - F_{\text{buoyancy}}$ than that of 1.9 g/cm^3 due to its smaller density difference with the fluid. Thus, depending on the height of the separation chamber which has a direct influence on the fluid flow, the cells which have smaller density difference with fluid show a wide variation of H_{max}, such as the cells having a density of 1.1 g/cm^3. On the other hand, the H_{max} of heavier cells having a density of 1.9 g/cm^3 has a small variation due to the larger density difference. The results of Figure 2.3 can be concluded that increasing the h_c/h_i can be one further way of separating the cells which have the density close to the surrounding fluid.

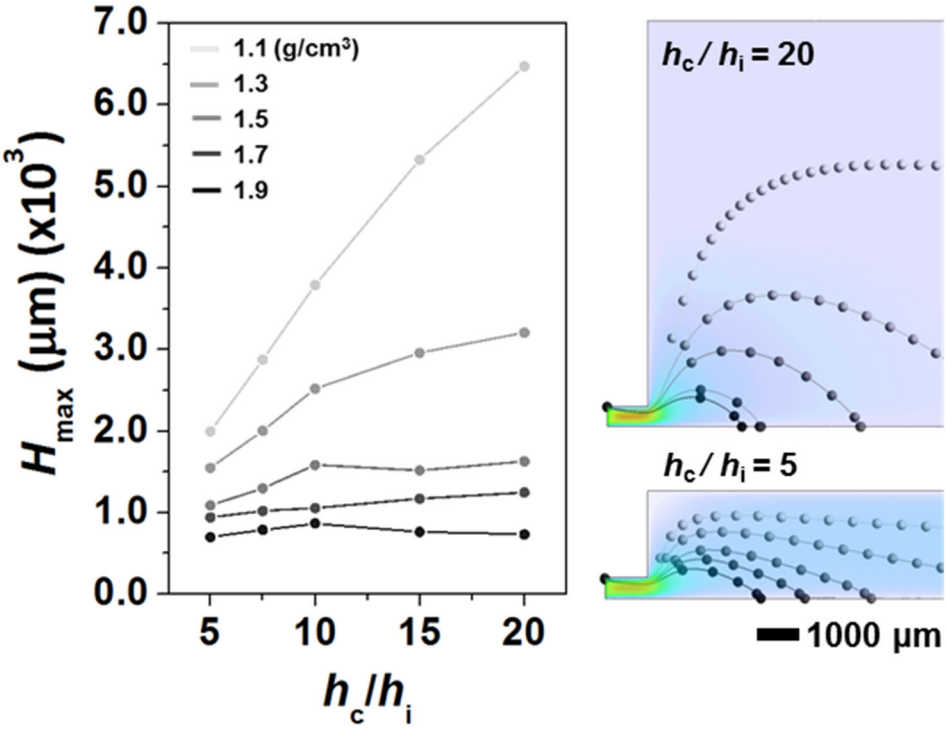

Figure 2.3. Microfluidic cell separation with respect to the ratio of the height of the inlet (h_i) to the separation chamber (h_c).

2.5. Optimized Device for the Selective Separation of the Lightest Cells

Based on the above approach, we propose a design of the microfluidic device which can selectively separate the lightest cells. Figure 2.4(a) only shows one unit consisting of three outlets, which can be connected in series for the cell separating microfluidic device. Using this design, the separation of the lightest cell having a density of 1.1 g/cm^3 is considered among 125 cells with 5 different densities (25 cells each per density) of 1.1 g/cm^3, 1.2 g/cm^3, 1.3 g/cm^3, 1.4 g/cm^3, and 1.5 g/cm^3. Figure 2.4(b) shows the representative separation behavior of the cells depending on their density. From the single separation process, 40% of the lightest cells (1.1 g/ cm^3) are recovered through the upper outlet. When the separation process is sequentially operated, the yield of separating lightest cells is enhanced with the increasing number of cycles as shown in Figure 4(c).

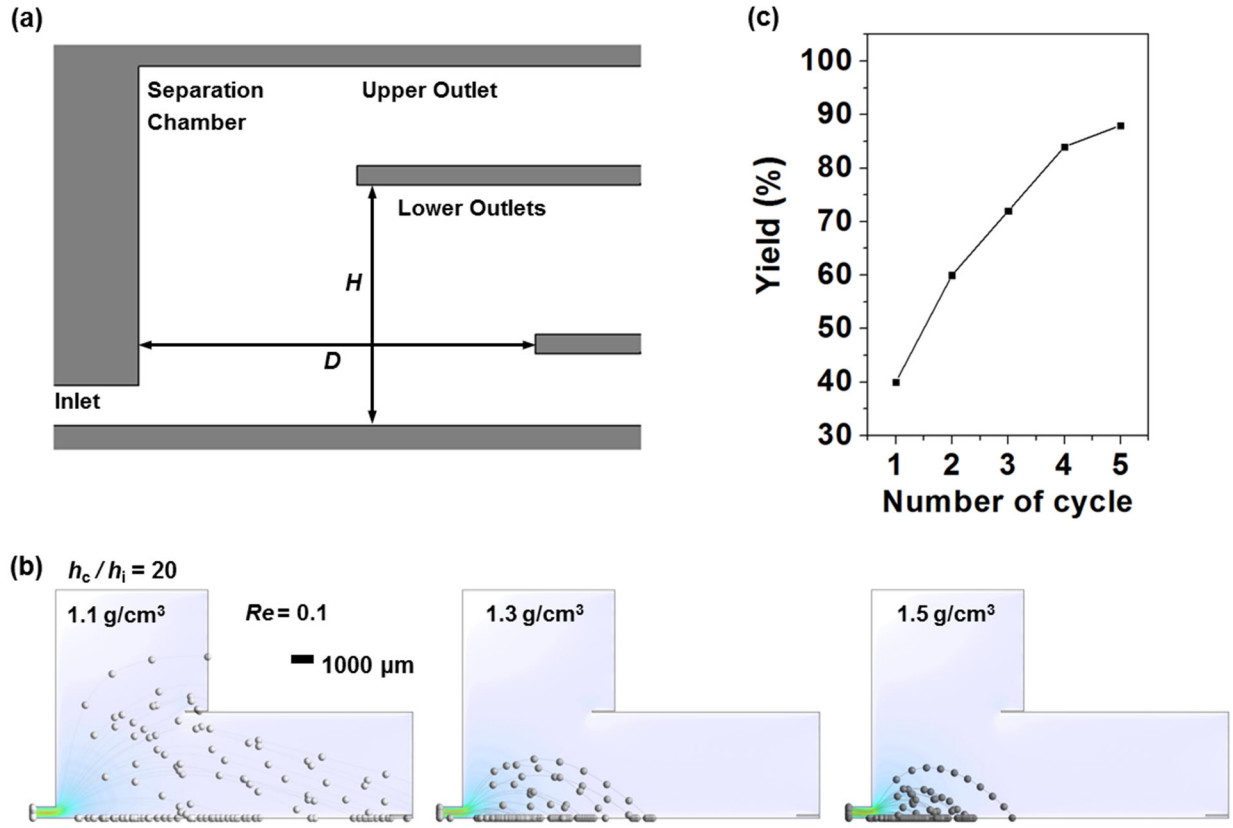

Figure 2.4. (A) One unit of the proposed microfluidic device for the selective separation of the lightest cell based on the simulation results. Cells are separated into two outlets based on differences in both the height and distance traveled stemming from differences in density. **(B)** Representative separation behavior of cells observed in the device. **(C)** The yield of the lightest cell (1.1 g/cm^3) with the proposed microfluidic device according to the number of cycles (*i.e.*, this unit is assumed to be connected in series).

2.6. Conclusion

In summary, we have demonstrated that the cells which have subtle density difference can be separated in the simple microfluidic device without any external forces. Our microfluidic cell separating design consists of three simple components, an inlet, a separation chamber, and multiple outlets. The cells having various densities show considerably different jump characteristics in the separation chamber according to the acted forces, such as $F_{Buoyancy}$, $F_{Gravity,}$ and F_{Drag}. The jump characteristics of cells have been defined as maximum jump height (H_{max}), and maximum travels distance (D_{max}). Notably, the minimizing of density difference with the surrounding fluid allows effective separation of cells, and increasing the ratio of channel height of inlet and separation chamber (i.e., h_c/h_i) can be one further way of effective separating the cells having the density close to the surrounding fluid. Based on these results, we also proposed a microfluidic device that can selectively separate lightest cells among numerous cells having various density. We expect that the density-based separation design will aid in the selective separation of lipid-rich microalgae for bioenergy applications.

Reference

[1] J. Song, M. Song, T. Kang, D. Kim, and L. P. Lee, Biomicrofluidics 8, 6, 064108 (2014).
[2] X. Cheng, D. Irimia, M. Dixon, K. Sekine, U. Demirci, L. Zamir, R. G. Tompkins, W. Rodriguez, and M. Toner, Lab Chip. 7, 170 (2007).
[3] W. A. O'Brien, P. M. Hartigan, E. S. Daar, M. S. Simberkoff, and J. D. Hamilton, Ann. Intern. Med. 126, 939 (1997).
[4] N. M. Karabacak, P. S. Spuhler, F. Fachin, E. J. Lim, V. Pai, E. Ozkumur, J. M. Martel, N. Kojic, K. Smith, P. Chen, J. Yang, H. Hwang, B. Morgan, J. Trautwein, T. A. Barber, S. L. Stott, S. Maheswaran, R. Kapur, D. A. Haber, and M. Toner, Nat. protoc. 9, 694 (2014).
[5] H. W. Hou, M. E. Warkiani, B. L. Khoo, Z. R. Li, R. A. Soo, D. S. Tan, W. Lim, J. Han, A. A. S. Bhagat, and C. T. Lim, Scientific Reports 3, 1259 (2013).
[6] A. W. D. Larkum, I. L. Ross, O. Kruse, B. Hankamer, Trends Biotechnol. 30, 198 (2012).
[7] G. Mayer, M. S. L. Ahmed, A. Dolf, E. Endl, P. A. Knolle, M. Famulok, Nat. Prot. 5, 1993, (2010).
[8] M. M. Wang, E. Tu, D. E. Raymond, J. M. Yang, H. Zhang, N. Hagen, B. Dees, E. M. Mercer, A. H. Forster, I. Kariv, P. J. Marchand, and W. F. Butler, Nat. Biotechnol. 23, 83 (2005).
[9] J. D. Adams, U. Kim, H. T. Soh, PNAS. 105, 18165 (2008).
[10] K. Schriebl, G. Satianegara, A. Hwang, H. L. Tan, W. J. Fong, H. H. Yang, A. Jungbauer, A. Choo, Tissue Eng. Pt. A 18, 899 (2012).

[11] M. D. Vahey, and J. Voldman, Anal. Chem. 80, 3135 (2008).
[12] U. Kim, J. R. Qian, S. A. Kenrick, P. S. Daugherty, H. T. Soh, Anal. Chem. 80, 8656 (2008).
[13] X. Y. Hu, P. H. Bessette, J. R. Qian, C. D. Meinhart, P. S. Daugherty, and H. T. Soh, PNAS. 102, 15757 (2005).
[14] Y. Liu, and KM. Lim, Lab Chip. 11, 3167 (2011).
[15] N.R. Harris, M. Hill, S. Beeby, Y. Shen, N.M. White, J.J. Hawkes, W.T. Coakley, Sens. Actuators B 95, 425 (2003).
[16] M. Evander, A. Lenshof, T. Laurell, and J. Nilsson, Anal. Chem. 80, 5178 (2008).
[17] P. Sajeesh, A. K. Sen, Microfluid Nanofluid 17, 1 (2014).
[18] T. Morijiri, S. Sunahiro, M. Senaha, M. Yamada, and M. Seki, Microfluid Nanofluid 11, 105 (2011).
[19] A. A. S. Bhagat, H. Bow, H. W. Hou, S. J. Tan, J. Han, and C. T. Lim, Med. Biol. Eng. Comput. 48, 999 (2010).
[20] E. Eroglu, and A. Melis, Biotechnol. Bioeng. 102, 1406 (2009).

Chapter 3

Photonic Cavity Bioreactor for Rapid Strain Screening

Algal photosynthesis, which makes up a large proportion of the photosynthesis on Earth, is considered as a sustainable and renewable solution to generating bioenergy. However, to maximize the efficiency of photosynthesis in non-arable regions with varying environmental conditions, a precise and rapid screening method is critical for selecting suitable strains from hundreds of thousands of natural and genetically engineered strains. In this chapter, we will present a photonic cavity bioreactor (PCB) as a microalgal bioreactor that provides an optimal microenvironment of light and intercellular interactions, allowing the rapid screening of microalgae in a high-throughput manner [1]. Our PCBs can scatter and amplify incident light, converting it into a spectrum favorable for photosynthetic pigment absorption. The bowl-shaped cavity permits proximity between cells; thus, the typical lag phase of algal cultures is almost considerably shortened. *Chlamydomonas reinhardtii* was cultured in the PCBs, and we attained 2-fold and 1.5-fold enhancements in the growth rate and lipid production, respectively, with a 2-day reduction in the duration of the lag phase. By generating such high growth and biomass conversion rates over a short period, the PCBs are ideal bioreactors and rapid screening platforms for biofuel applications.

3.1. Introduction

Phototrophic organisms play a crucial role in capturing solar energy and converting it to chemical energy. Traditional agriculture has been vital for providing food throughout human history. Now, different types of byproducts from phototrophic species are being sought as a promising solution to the current energy crisis [2-9]. Microalgae are being considered as the most promising long-term, sustainable sources of biomass and fuel energy. In addition to their rapid growth, the merits of microalgae stem from the fact that algal farming does not compete with agriculture, as it uses non-arable land and water sources that are not useable for arable crops [10]. Because less than 4 % of the Earth's surface area and 1 % of global water [11] are suitable for traditional agriculture, microalgae offer enormous potential for the generation of phototrophic byproducts if algal farming can be achieved in environments other than on arable land and water. However, current microalgal researchers have focused on the feasibility of microalgal applications and investigated mainly a minuscule portion of the enormous biodiversity of microalgae in nature. An estimation that non-studied microalgae strains will be more productive of valuable byproducts in a local environment [12-17] implies the necessity of efficient screening methods of microalgae. Moreover, since the current genetic engineering approach to enhance the bio-productivity of microalgae further expands strain diversity due to the imperfectness of engineering methods (i.e., a lack of gene delivery tools specific for various subcellular compartments [6]), a screening procedure is critical in developing genetically superior strains. Herein, we develop a rapid screening platform enabling accelerated growth rates and biomass production of microalgae, which provides compelling advantages for the initial screening from a low-density algal population.

A conventional microalgal screening from an algal pool (i.e., local sample and genetic mutation) involves a low-density culture in liquid-based media [16, 18-20]. This approach requires a long period over a few weeks and a large amount of media, thus limiting the throughput of screening. As an alternative, agar plate-based screening has been introduced to increase screening throughput [21-24]. Although several benefits are attained, such as convenience in culturing, tracking and retrieving individual strains, rapid and homogenous initial growth rate, and naked-eye examination, agar plate culture cannot be ideal since microalgae in nature grow as floating in water but not immobilized. However, our screening platform can provide homogenous and rapid growth of microalgae as a liquid-based culture due to the unique optical properties and shape of the photonic cavity bioreactor (PCB).

3.2. Design of Photonic Cavity Bioreactor (PCB)

The functional unit of our screening platform, PCB, is configured as a monolithic assembly of plasmonic nanostructures on a macroscale hemispherical wall. To allow rapid screening, the plasmonic nanostructures and the optical geometry of the PCBs amplify the incident light and convert it into a spectrum favorable for photosynthesis. The hemispheric cavity, as uniformly covered with the plasmonic nanostructures, can focus light selectively scattered from the plasmonic nanostructures at the bottom center of the cavity geometry. Because phototaxis and sedimentation of microalgae permit a high density of microalgae at the bottom of the PCB cavities, the favorably amplified light can be effectively delivered to a population of microalgae in the PCBs (Fig. 3.1).

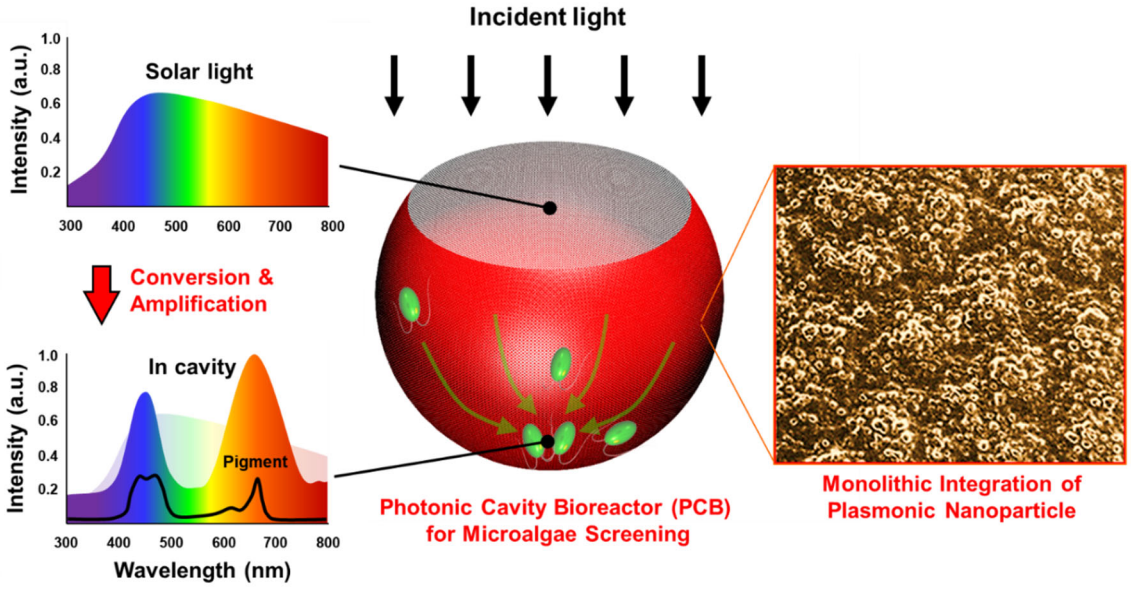

Figure 3.1. Features of Photonic Cavity Bioreactor (PCB). (Left) Plasmonic nanostructures in the PCB wall convert incident light to a spectrum favorable to photosynthesis pigment. Also, the optical geometry of the PCB allows the focus of light favorably converted for photosynthesis at the bottom center of PCB. (Middle) Phototaxis and bounded movement of microalgae can gather microalgae at the position of the optical focus. (Right) A zoom-in illustration shows the photonic cavity bioreactor integrated with plasmonic nanoparticles on the inner wall.

3.3. Fabrication of Photonic Cavity Bioreactor (PCB)

For this study, we fabricated PCB utilizing a novel fabrication process termed ionic water lithography (iWL). At the interface between different media that are immiscible with each other, the byproducts of chemical reactions can be unique differently from those of volume reactions, in which one type of molecule reacts with different ones in other interfacing media. By utilizing interfacial reactions during the polymerization process of a pre-polymer, a monolithic array of metal nanoparticle can be created at the surface of the polymer. The detailed procedure for ionic water lithography is as follows. By dropping ionic water onto the pre-polymer, a bowl-shaped geometry is created owing to the combined effects of gravity, surface tension, density differences, and repulsion between the immiscible water and pre-polymer (Fig. 3.2 Left & Middle). The curvature of the bowl-shaped geometry is determined by the surface tension, the volume of the ionic water droplets, and the density difference between the two immiscible media. Simultaneously, metal nanoparticles are formed and align with the surface of the bowl-shaped geometry (Fig. 3.2 Right). The formation and arrangement of these metal nanoparticles are driven by the diffusion of cations into the pre-polymer, as well as by charge interactions, the reducing potential of the curing agent, thermodynamics, and surface energy. The size and density of the metal nanoparticles on the surface of the bowl-shaped geometry are controlled by the concentration of ionic water, the ratio of pre-polymer base to curing agent, and the temperature.

As shown in Figure 3.3A, we fabricated four types of PCBs in a 96-well format on a polydimethylsiloxane (PDMS) substrate by varying the concentration of gold ions in the process of ionic water lithography. As will be introduced later, plasmonic gold nanostructures, which are embedded underneath the PCB surface as a thin layer (Fig. 3.3B, C & D), hold optical resonance around 680 nm. Thus, our screening platform is arrayed as red-colored elliptical cavities. From the concentration of gold ions in the process of ionic water lithography, the four types of PCBs possessed different densities of plasmonic nanostructures with a variety of optical scattering resonance around 680 nm. They were termed PCB 1, PCB 2, PCB 3, and PCB 4 as the nanostructure density increases. Also, for a control experiment, we fabricated a cavity of the same shape as the PCB concave bowl without plasmonic nanoparticle integration. We utilized this ‘bare’ cavity to visualize the movement of individual microalgae and to decouple the effects of enhanced intercellular interactions and the favorably amplified light resulting from nanoparticle scattering.

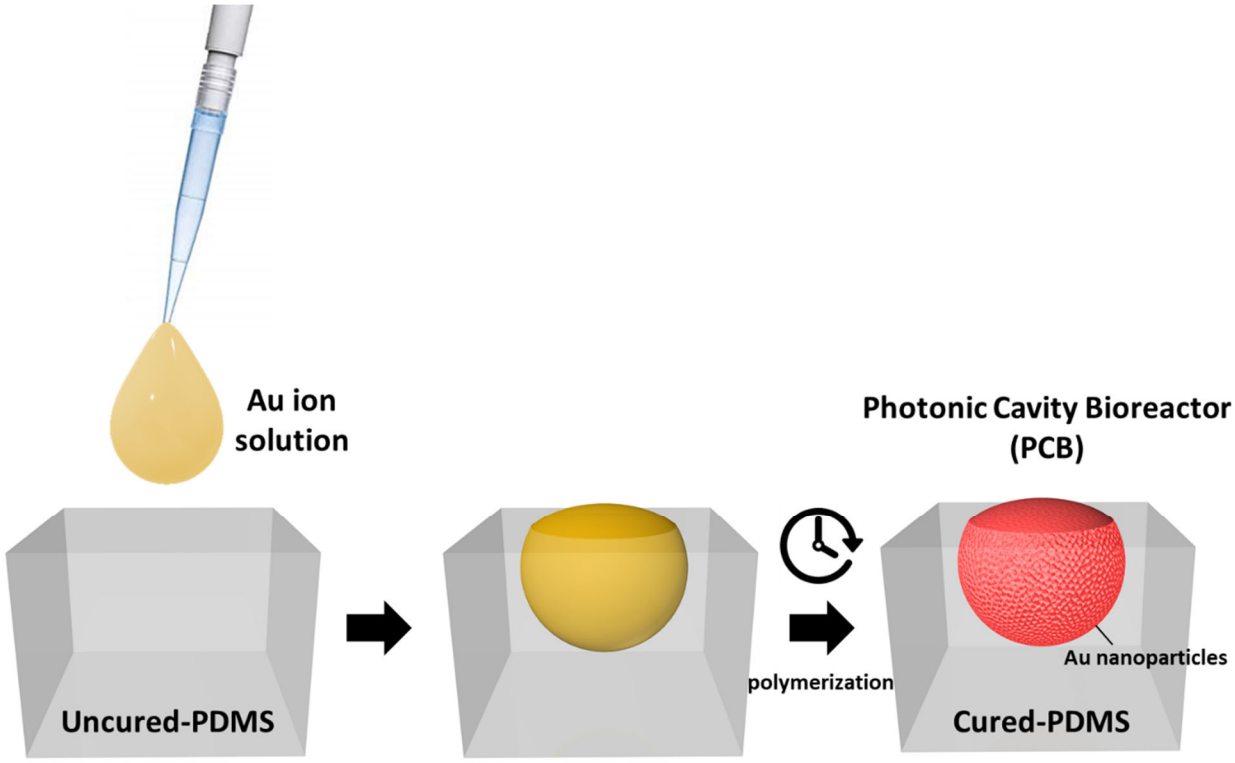

Figure 3.2. Schematic illustration of the Photonic Cavity Bioreactor (PCB) fabrication process. When the gold ion solution dropped on top of the uncured-PDMS, a bowl-shaped cavity is generated due to the combined effects of gravity, surface tension, density differences, and repulsion between immiscible gold ion solution and uncured-PDMS. As time passes, gold ions in solution move into the uncured-PDMS through diffusion and charge interactions, and gold nanoparticles are formed and aligned along the surface of the bowl-shaped cavity simultaneously, which are driven by the reducing potential of the curing agent, thermodynamics, and surface energy.

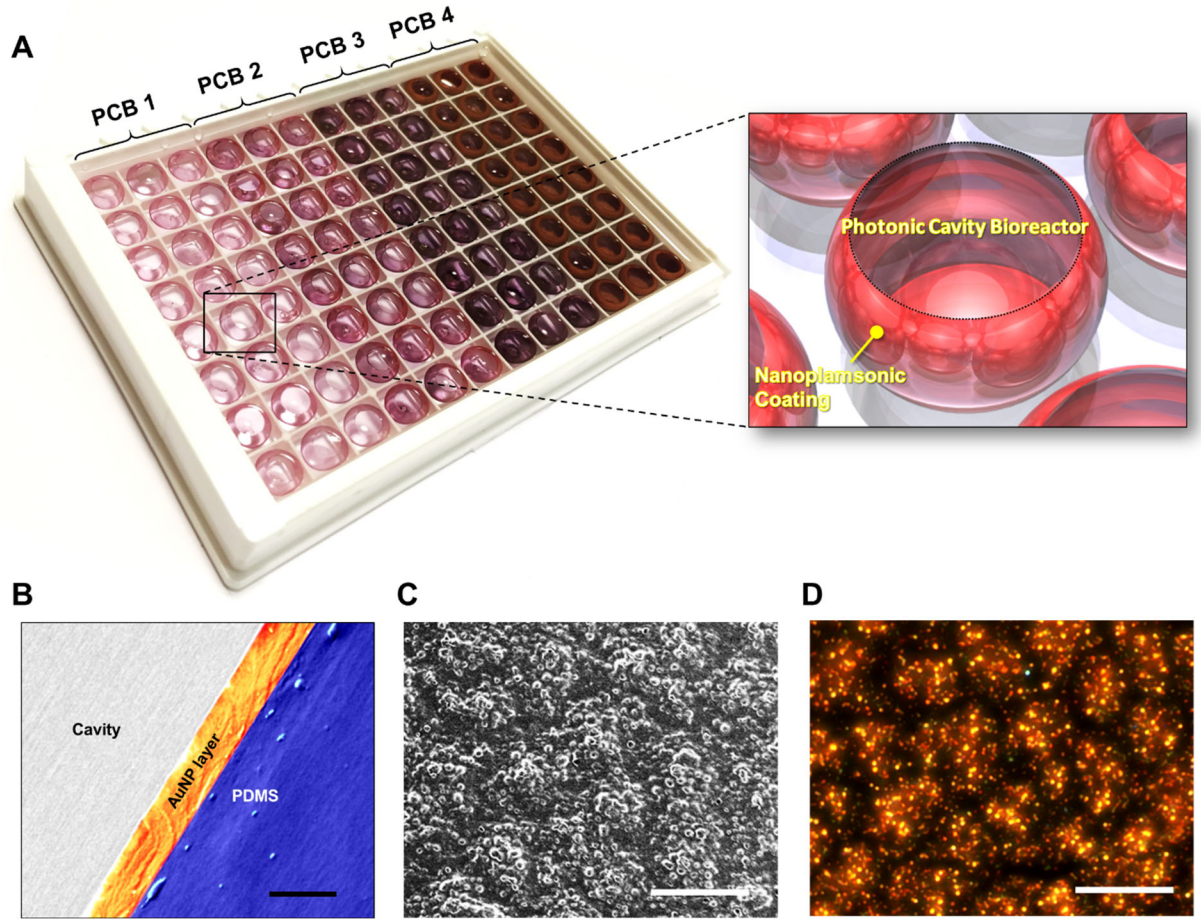

Figure 3.3. Fabricated PCBs in a 96-well format. **(A)** The integrated microalgae analysis photobioreactor used in this study was arrayed with four types of PCB as a 96-well format. A zoom-in illustration shows the photonic cavity unit integrated with plasmonic nanoparticles on the inner wall. According to the calculation result, the plasmonic nanoparticle density of four types of PCB could be varied from 500 to 3000 nm interparticle distances (details in Supporting Information). **(B)** A pseudo-colored scanning electron microscopy (SEM) image for the cryosectioned photonic cavity (PCB 3). The thickness of the plasmonic nanoparticle layer was about 1-μm thick. The scale bar is 2 μm. **(C & D)** SEM and optical dark-field images for gold nanoparticle clusters embedded a photonic cavity, respectively. The scale bar is 20 μm.

3.4. Characterization of Optical Properties of the Photonic Cavity Bioreactor (PCB)

3.4.1. Asymmetric Optical Scattering of the Gold Nanoparticle in the PCB

To assess the optical properties of the PCB, first, we characterized the spectral conversion feature of the photonic cavity by using theoretical calculations and experiments. Because the gold nanoparticles integrated in the PCB wall were 100–200 nm in diameter from electron microscopy characterization, we evaluated the spatial distribution of plasmonic scattering from nanoparticles of this size. By using commercial software (a 3D RF module of COMSOL 3.5a), electromagnetic field generating around 100-200nm gold nanospheres were calculated upon a spatially homogenous illumination of 500-1000 nm. For this, a circular oblique illumination attained by the dark-field condenser was considered as incident light. The calculation result was imported into MATLAB (a mathematical software) and post-processed as far-field intensity distribution in a nanoparticle-centered spherical coordinate. The electromagnetic simulation indicated that plasmonic nanoparticles larger than 100 nm in diameter could generate an asymmetrical pattern of optical scattering that differs from ideal dipole scattering (i.e., a pattern that is perpendicular to the incident direction), as shown in Figure 3.4A. To experimentally examine the asymmetry of PCB nanoparticle scattering, we measured and compared dark-field scattering spectra by using different numerical apertures (NA) of 0.25, 0.4, and 0.6 because the NA is related to the angular integration range of the scattering measurement (details in Appendix). We characterized three scattering regions as $\theta < \sin^{-1}(0.25)$, $\sin^{-1}(0.25) < \theta < \sin^{-1}(0.4)$, $\sin^{-1}(0.4) < \theta < \sin^{-1}(0.6)$ based on NA=n $\sin(\theta)$, where n (refractive index) is 1. The results in Figure 3.4B show that the nanoparticles in the PCBs can preferentially scatter incident light at 120 to 140 ° relative to the dark-field illumination angle, which occurs at $\sin^{-1}(0.25) < \theta < \sin^{-1}(0.4)$.

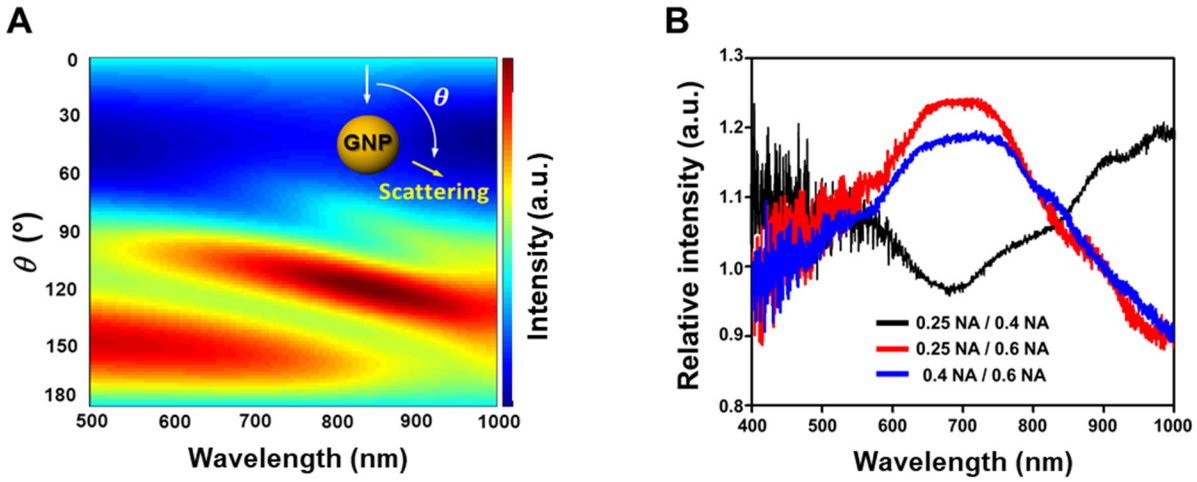

Figure 3.4. Characterization of optical scattering patterns generated from gold nanoparticle embedded in the PCB **(A)** Spatial distribution of optical scattering generated from the 150-nm gold nanosphere for the polar angle θ as a function of wavelength. This heatmap plot indicates a scattering profile different from an ideal dipole scattering. **(B)** Experimental demonstration for the asymmetric scattering pattern of the gold nanoparticle. A set of dark-field scattering spectra was measured using three objectives of different numerical apertures (NA) from a thin slice of a photonic cavity (PCB 2) as immersed in a refractive-index-matched liquid.

3.4.2. Amplified Optical Field at the Bottom Center of the PCB

Combined with the asymmetry of the nanoparticle scattering pattern described above, the optical geometry of the cavity shape permits intense focusing of incident light at the bottom center of the PCBs. For ray optics calculation, ray tracing on the photonic cavity was performed using an in-house program. In the calculation, PDMS and cavity volume were set with refractive indexes of 1.4 and 1.33, respectively, and the cavity surface was a scattering boundary with characteristics attained from electromagnetic simulation. Representative rays were overlaid over the optical intensity heatmap as red lines. The ray optics calculation result (Fig. 3.5A) shows the light focusing feature at the bottom center of the photonic cavity. Also, using an in-house scattering measurement setup with a low-NA optical fiber scanner (Fig. B.3 in supplementary information), we experimentally confirmed that the amplified optical field is generated at the bottom center of the PCBs. The spatial optical scattering distribution shown in Figure 3.5B is normalized to the blue-to-red color axis ranging from 0 to 1, and the four types of PCBs exhibited an almost identical spatial profile of scattering distribution as normalized, with different absolute maxima proportional to the dark-field scattering ratio.

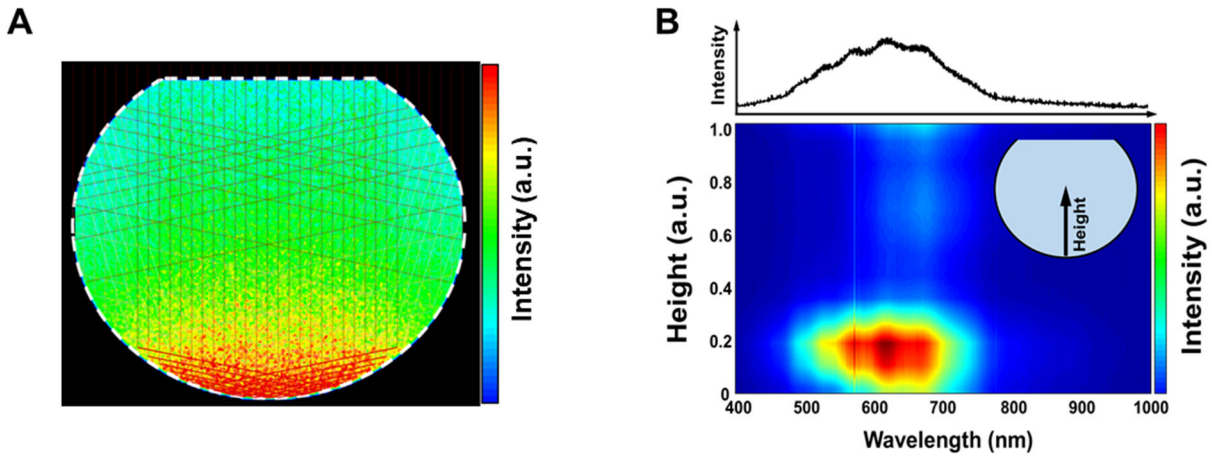

Figure 3.5. Light focusing feature of the PCB **(A)** A heatmap plot for optical intensity profile inside the photonic cavity. A ray-tracing was applied for 650nm illumination with the scattering profile of the nanoparticles attained in (Fig. 3.4A). The main rays are shown as red lines in the plot. **(B)** Experimental measurement of optical power distribution along the z-axis of the cavity from the bottom center. The light from a 4000K halogen bulb was illuminated vertically on the PCB 2 half-cut along the z-axis. Details of the experimental setup is shown in supplementary information (Fig. B.3).

3.4.3. Optical Characteristics of the Four PCBs

To assess optical properties of the four different types of PCB, the dark-field scattering spectrum was measured from each photonic cavity. All of the PCBs produced optical resonances similar to the absorption peak of a photosynthesis pigment at approximately 680 nm with minor variations (Fig. 3.6A). But their scattering spectrum has different maximal intensities each other as indicated in the legend. Thus, by using indices for spectrum quality, $\int I_{PCB} \cdot Q_{abs}\, d\lambda$ (here, I_{PCB} and Q_{abs} are scattering intensity of PCB and absorption magnitude of photosynthesis pigment at a specific wavelength, respectively) and optical power exposed cells residing at the bottom center of the PCBs, the four PCB types can allow the variation of spectrum quality and optical power for a green microalgae growth (Fig. 3.6B).

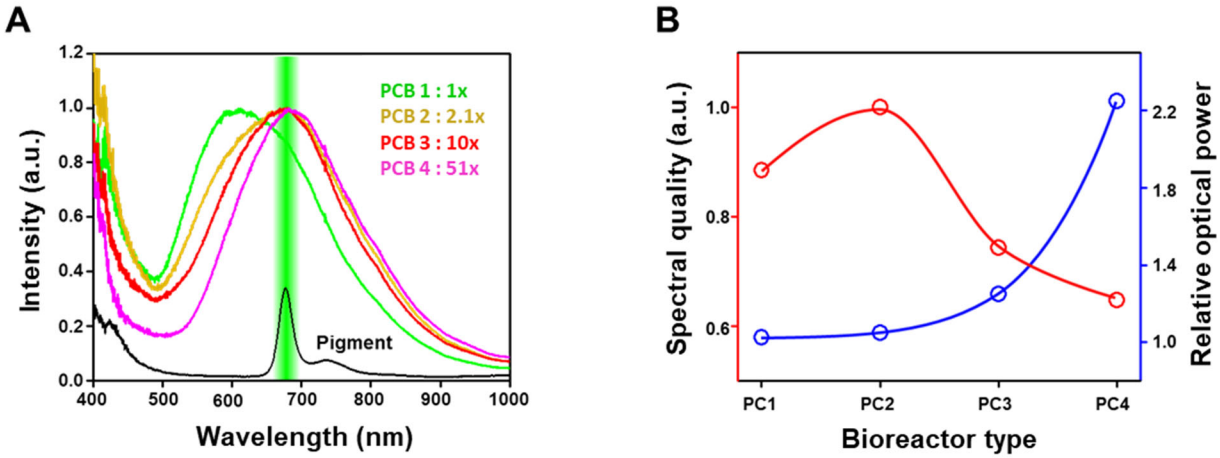

Figure 3.6. Optical characteristics of the four different types of PCBs **(A)** Dark-field scattering spectra of the four types of PCBs. The absorption spectrum of photosynthetic pigments extracted from *Chlamydomonas reinhardtii* is overlaid as a black line. All spectra are normalized, and each maximal intensity is indicated in the legend. **(B)** Optical characteristics of the four photonic cavities regarding spectral quality for photosynthetic pigments and optical power on the cellular population accumulated cavity center.

3.5. Characterization of Movement Behaviors of Microalgae in PCB

3.5.1. Confined Movement of Microalgae at the Bottom Center of the PCB

In addition to their optical characteristics, the cavity geometry of PCBs can facilitate a stable gathering of microalgal cells, which can accelerate initial population growth. In order to characterize the movement behaviors of microalgae in the PCB, single-cell tracking was performed with the hundreds of cells freely swimming in the PCB under illumination and compared with the case of the flat chamber. Our single-cell tracking of *Chlamydomonas reinhardtii*, a flagellated microalgae, indicates that the PCB chamber enhances the local cell density and intercellular interactions, thus potentially being advantageous during early-stage cell growth, as a shortened lag phase is commonly observed in solid-phase culture (i.e., agar culture) [21].

As shown in Figure 3.7A & B, the swimming patterns of the flagellated microalgae were apparently different between the flat- and the cavity-shaped chambers. The individual swimming patterns of microalgae were consistently restricted around the geometric center of the cavity chamber, whereas those of microalgae in the flat chamber were random. We analyzed two aspects of these different swimming patterns: the spatial frequency of cell positioning, and the effective radius of the swimming trace. The spatial frequency analysis demonstrated that the cavity chamber generated a higher frequency of positioning closer to the center of the cavity. But the cells under the other condition displayed a random spatial distribution of positioning frequency, which may result in an inconsistent initial growth rate of low-density culture (Fig. 3.7C & D). The characterization on the effective radius (the minimum radius enclosing the entire trace for individual cells) shows that regardless of swimming distance, the overall movement in the cavity chambers was bounded by smaller radii than that in the flat chamber (Fig. 3.7E). All the analyses confirm that the cells can be stably positioned at the bottom center of the cavity, thus enhancing intercellular interactions during algal culture in the PCB.

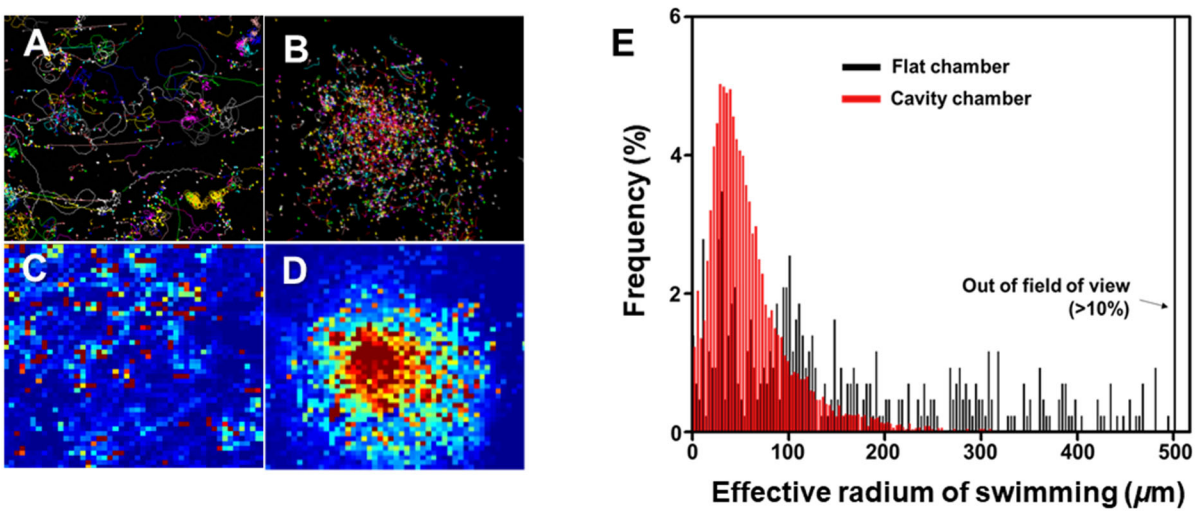

Figure 3.7. Confined movement of microalgae and enhanced intercellular interaction in PCB. **(A & B)** Individual swimming traces in the flat chamber and PCB, respectively. **(C & D)** Heatmap plots for spatial positioning frequency in the flat chamber and PCB, respectively. **(E)** A histogram for effective radii of swimming traces of individual cells. Approximately 300 cells were counted for this histogram.

3.5.2. Benefit of the Confined Movement at the Bottom Center of the PCB

The movement confined at the cavity center can be beneficial for a microalgal screening process because it allows growth to be evaluated by the naked eye, similarly to solid-phase screening [25-27]. Thus, we observed the change and growth of populations freshly added to the cavities over four days. Figure 3.8A & B are successive short-term and long-term snapshots, respectively. Within 3 hours, an increased local density at the bottom center of the cavity was clearly observed, and the extent of growth was able to be distinguished over four days. To examine the correlation between cell number and the snapshot results, we added various known cell concentrations into the PCB and examined the green color intensity of the acquired images. As shown in Figure 3.8C, a correlation was clearly observed between the total cell number and the green color intensity.

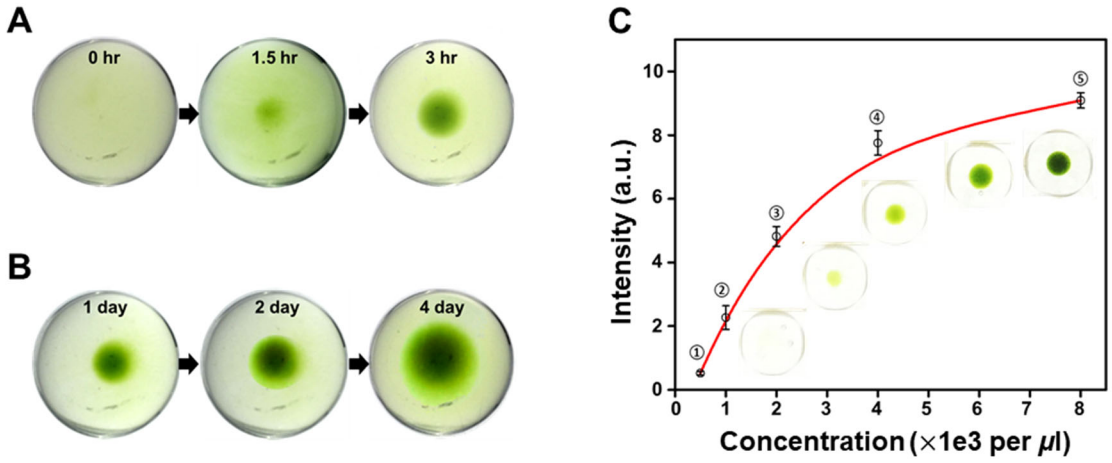

Figure 3.8. Naked-eye examination of cell growth enabled by confined movement of cells. **(A & B)** Top-view photographs of short-term (up to 3 hrs) and long-term (up to 4 days) culture of *Chlamydomonas reinhardtii* in the bare cavity. The microalgae were inoculated to the cavity vessel as 3000 per μL. To mimic the optical condition in PCB, a ring illumination was placed at the top of the cavity and focused at the bottom center. A stable accumulation of the microalgae at the bottom center was attained within 3 hours and maintained along with the population growth. **(C)** A correlation plot between cell number and green-color intensity at the cavity center. Known concentrations of cells (x-axis) were inoculated in cavities with a volume of 200 μL. Those cells were accumulated at the bottom center after 4 hours.

Also, the confined movement due to the geometry of the PCB permits enhanced intercellular interaction resulting in expedite cell growth in a low concentration culture. To assess the advantage of the confined movement in the low-density cell culture which is coming from photonic cavity geometry, we inoculated *Chlamydomonas reinhardtii* (CC124), flagellated green microalgae, as single-cell dissociation in bare cavities with four different curvatures as a low density of 2 cells per μl. 18 hours after inoculation, the microalgae population was augmented as the curvature of cavity increases, as shown in Figure 3.9A. The microalgae population increased up to 1.9 folds at the cavity of the biggest curvature in comparison with the case of the lowest one. As demonstrated, the features of the PCBs can be valuable for accelerating the initial growth of

microalgae, thus decreasing the time cost of microalgal R&D stages, which require the handling of a small number of microalgal cells for individual strains in screening and selection. Blue and green wavelength light can inhibitory biomass production and cell division through the dissipation of excess excitation energy as heat or low photosynthetic quantum yield [28]. When only a tiny number of cells are available in culture, growth inhibitory factors often cause elongated lag phase more randomly, thus making early characterization difficult (Fig. 3.9B). As favorably amplified optical spectrum and enhanced intercellular interactions and local density can be attained in PCB cultures, a rapid characterization on population growth and biomass production rates can be accomplished in a low-density screening.

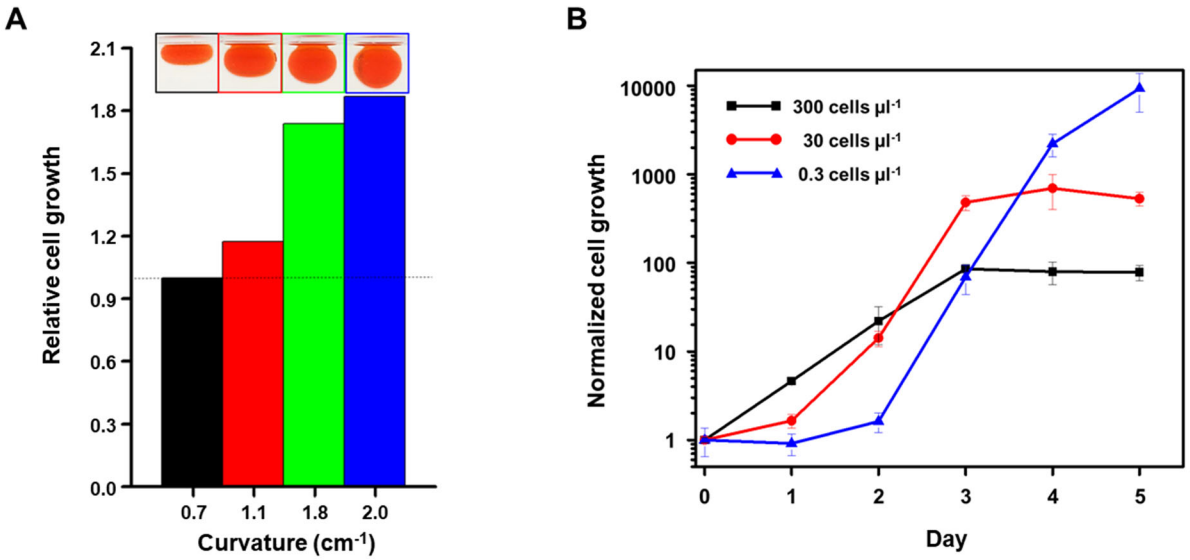

Figure 3.9. Benefit of the cavity's curvature in the low-density cell culture. **(A)** Relative cell growth from the bare cavities with four different curvatures normalized by the cell numbers in the cavity with minimum curvature (0.7). It shows higher relative cell growth as the curvature increases. Microalgae cells, which were in the 5th day of the stationary phase, were inoculated into the various curvature cavities, and the cell numbers were counted after 18 hours. **(B)** Correlation between lag phase duration and initial inoculation cell density. The lag phase becomes longer as the initial cell density decreases. All standard deviations were calculated from five independent cultures.

3.6. Characterization of Microalgal Culture in PCBs

3.6.1. Microalgal Growth in PCB

Herein, we characterized three aspects of algal culture productivity (growth rate, lag phase duration, and biofuel production) by culturing *Chlamydomonas reinhardtii* CC124 (a wild-type strain) at a low population density to demonstrate the advantages of PCB in strain screening. These aspects are generally considered when screening microalgal strains for biofuel applications [29, 30]. First, to evaluate the microalgal growth rate in the photonic cavity, microalgae in the exponential phase (Fig. B.4 in supplementary information) were inoculated in various photonic cavities, and the changes in the cell number and chlorophyll content were characterized (Fig. 3.10A). Compared to a flat cylindrical chamber and a bare cavity, the PCB cultures significantly enhanced the cell number and chlorophyll content by up to 2 folds. The PCB 1, 2, and 3 induced more chlorophyll production than population growth, indicating that chlorophyll content was more strongly influenced by spectral quality than by optical power. In contrast, the PCB 4 generated a less growth and chlorophyll content than the other PCB types, and the observed increase in chlorophyll was smaller than the increase in population, which indicated an overdose of light exposure from the high-density plasmonic nanostructures.

To evaluate the lag-phase period in PCB culture, microalgae on the 5th day of the saturation stage were placed into PCBs and control chambers with fresh media. Over the next 4 days, all growth curves from PCBs, both bare cavity and flat chamber, were S-curve-shaped. Typically, the microalgal growth curve consists of a lag phase, an exponential phase, and a stationary phase. Compared to a flat chamber culture, the lag phases of cultures grown in PCBs and bare cavities were shortened by 2.5 and 1.5 days, respectively. As shown in Figure 3.10B, the growth curve of the PCB cultures appeared to enter the exponential stage, even on the 1st day of culture. The growth rates of the PCB cultures also were enhanced by more than 2-fold during the exponential phase compared to the bare cavity and flat chamber cultures.

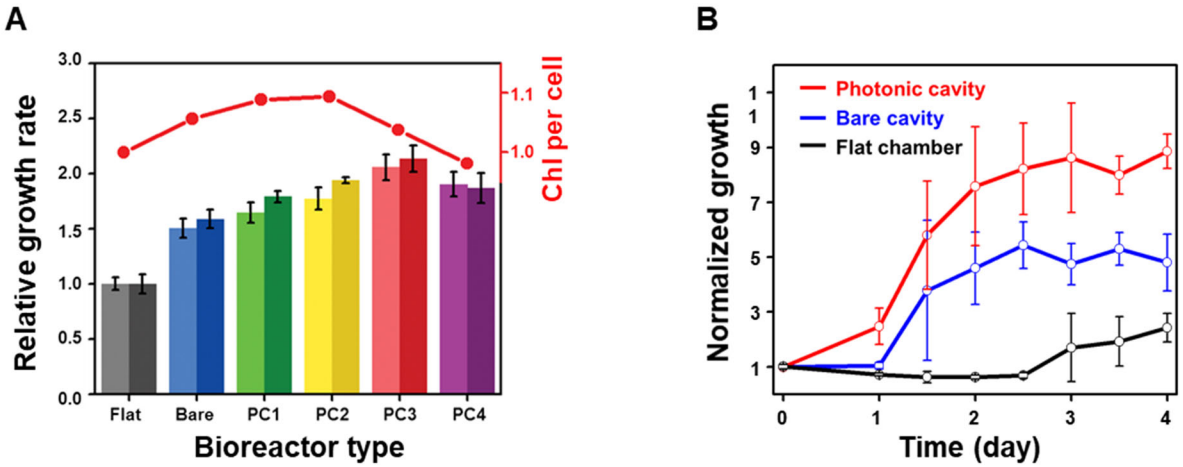

Figure 3.10. Characterization of microalgal culture in PCBs. **(A)** Change of cell number and chlorophyll content from PCBs and control chambers after 24-hour culture. *Chlamydomonas reinhardtii*, which were in the exponential stage of growth, were inoculated into the various culture chambers, and the amounts of population and chlorophyll were measured by hemocytometer and optical density, respectively. All cases were normalized by the flat chamber culture. The lighter and darker bars in the plot present cell number and chlorophyll, respectively. The red line is the

comparison between cell number and chlorophyll amount. **(B)** Characterization of lag phase in low-density culture. Cells in the saturation stage were inoculated into various culture chambers as a low density (i.e., 1 per 5 µL in 200 µL volume). All standard deviations were calculated from five independent cultures.

3.6.2. Microalgal Lipid Induction in PCB

Additionally, the photonic cavity was able to increase the lipid production rate, which is essential for biofuel applications. When a nitrogen source (NH_3^+) is removed from the culture medium (i.e., Tris-Acetate-Phosphate [TAP] medium), the algal metabolism and photosynthetic products result in the accumulation of lipid bodies in the cytoplasm [31,32]. Typically, small-size lipid bodies can be observed in the 2-3 days of induction, and along with further induction, the lipid bodies easily become as big as half of cell volume [32]. However, our PCB cultures clearly demonstrated lipid body formation after as few as 1 day. Our quantitative comparison on the 2nd day indicated that the total amount of lipids induced in the PCBs was 1.5x and 1.2x higher than that in the flat chamber and bare cavity, respectively (Fig. 3.11A). Notably, a small portion of cells from the PCB induction contained large compartments of lipid bodies in the cytoplasm (Fig. 3.11B③), a feature that was rarely observed among the flat chamber induction cells. As shown in the *Chlamydomonas reinhardtii* experiments, increased growth rates, reduced lag-phase times, and enhanced lipid production rates allow the accumulation of the desired cell population and lipid content over a short period, and these are considered to be crucial factors in initial microalgal strain screening.

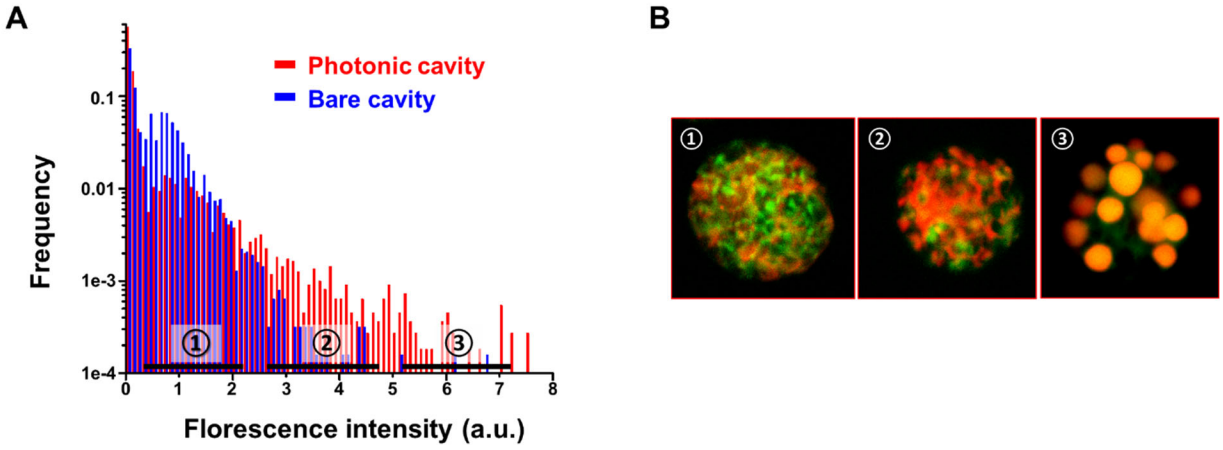

Figure 3.11. Characterization of microalgal lipid induction in PCB **(A)** A histogram of single-cell characterization on lipid induction. Lipid production of *Chlamydomonas reinhardtii* was induced by nitrogen starvation for 2 days. **(B)** The insets are confocal microscopy images, where the green and red channels are chlorophyll and lipid, respectively. Confocal microscopy images of lipid body stained microalgae, where the green and red channels are chlorophyll and lipid, respectively.

3.7. Conclusion

In conclusion, we present a photonic cavity bioreactor (PCB) that is monolithically covered with nanoplasmonic structures, which provide unique optical characteristics and advantages for microalgal culture. The enhanced intercellular interactions and favorably amplified optical spectrum attained in PCB culture were demonstrated to enhance the algal growth rate and biomass conversion and to decrease the lag phase. Besides, the ability to quantify population growth by the naked eye and the additional properties of the PDMS substrate, such as optical transparency and gas permeability, provide further benefits for algal screening. This study shows the potential of photonic cavity bioreactors for an expedite algal screening application, as well as for use as farm field bioreactor components.

Reference

[1] Hong, S.; Song, M.; Kim, S.; Bang, D.; Kang, T.; Choi, I.; Lee, LP. ACS Nano 2016;10(6):5635-42.
[2] Mata, T. M.; Martins, A. A.; Caetano, N. S. Renewable and Sustainable Energy Reviews 2010, 14, 217-232.
[3] Ahmad, A. L.; Yasin, N. H. M.; Derek, C. J. C.; Lim, J. K. Renewable and Sustainable Energy Reviews 2011, 15, (1), 584-593.
[4] Sayre, R. BioScience 2010, 60, (9), 722-727.
[5] Malcata, F. X. Trends in biotechnology 2011, 29, (11), 542-9.
[6] Markou, G.; Nerantzis, E. Biotechnology advances 2013, 31, (8), 1532-42.
[7] Schenk, P.; Thomas-Hall, S.; Stephens, E.; Marx, U.; Mussgnug, J.; Posten, C.; Kruse, O.; Hankamer, B. Bioenerg. Res. 2008, 1, (1), 20-43.
[8] Huang, G.; Chen, F.; Wei, D.; Zhang, X.; Chen, G. Applied energy 2010, 87, (1), 38-46.
[9] Spolaore, P.; Joannis-Cassan, C.; Duran, E.; Isambert, A. Journal of bioscience and bioengineering 2006, 101, (2), 87-96.
[10] Pittman, J. K.; Dean, A. P.; Osundeko, O. Bioresource Technology 2011, 102, (1), 17-25.
[11] Stephens, E.; Ross, I. L.; Mussgnug, J. H.; Wagner, L. D.; Borowitzka, M. A.; Posten, C.; Kruse, O.; Hankamer, B. Trends Plant Sci 2010, 15, (10), 554-64.
[12] Yang, H.-L.; Lu, C.-K.; Chen, S.-F.; Chen, Y.-M.; Chen, Y.-M. Marine biotechnology 2010, 12, (2), 173-185.
[13] Zhou, W.; Li, Y.; Min, M.; Hu, B.; Chen, P.; Ruan, R. Bioresource Technology 2011, 102, (13), 6909-6919.
[14] Duong, V. T.; Li, Y.; Nowak, E.; Schenk, P. M. Energies 2012, 5, (6), 1835-1849.

[15] Zhou, W.; Hu, B.; Li, Y.; Min, M.; Mohr, M.; Du, Z.; Chen, P.; Ruan, R. Applied biochemistry and biotechnology 2012, 168, (2), 348-363.
[16] Lee, K.; Eisterhold, M. L.; Rindi, F.; Palanisami, S.; Nam, P. K. J Nat Sci Biol Med 2014, 5, (2), 333-9.
[17] Larkum, A. W.; Ross, I. L.; Kruse, O.; Hankamer, B. Trends Biotechnol 2012, 30, (4), 198-205.
[18] Doan, T. T. Y.; Sivaloganathan, B.; Obbard, J. P. Biomass and Bioenergy 2011, 35, (7), 2534-2544.
[19] Sydney, E. B.; da Silva, T. E.; Tokarski, A.; Novak, A. C.; de Carvalho, J. C.; Woiciecohwski, A. L.; Larroche, C.; Soccol, C. R. Applied Energy 2011, 88, (10), 3291-3294.
[20] Cole, J. K.; Hutchison, J. R.; Renslow, R. S.; Kim, Y.-M.; Chrisler, W. B.; Engelmann, H. E.; Dohnalkova, A. C.; Hu, D.; Metz, T. O.; Fredrickson, J. K.; Lindemann, S. R. Frontiers in Microbiology 2014, 5.
[21] Pereira, H.; Barreira, L.; Mozes, A.; Florindo, C.; Polo, C.; Duarte, C. V.; Custodio, L.; Varela, J. Biotechnol Biofuels 2011, 4, (1), 61.
[22] Chan, A.; Andersen, R.; Le Blanc, M.; Harrison, P. Marine Biology 1980, 59, (1), 7-13.
[23] Volk, R.-B. Journal of applied phycology 2005, 17, (4), 339-347.
[24] Mutanda, T.; Ramesh, D.; Karthikeyan, S.; Kumari, S.; Anandraj, A.; Bux, F. Bioresource Technology 2011, 102, (1), 57-70.
[25] Tulin, F.; Cross, F. R. Plant Cell 2014, 26, (10), 4019-38.
[26] Bogen, C.; Al-Dilaimi, A.; Albersmeier, A.; Wichmann, J.; Grundmann, M.; Rupp, O.; Lauersen, K. J.; Blifernez-Klassen, O.; Kalinowski, J.; Goesmann, A.; Mussgnug, J. H.; Kruse, O. BMC Genomics 2013, 14, 926.
[27] Wakao, S.; Chin, B. L.; Ledford, H. K.; Dent, R. M.; Casero, D.; Pellegrini, M.; Merchant, S. S.; Niyogi, K. K. Elife 2014, 3, e02286.
[28] Schulze, P. S. C.; Barreira, L. A.; Pereira, H. G. C.; Perales, J. A.; Varela, J. C. S. Trends in biotechnology 2014, 32, (8), 422-430.
[29] Gendy, T. S.; El-Temtamy, S. A. Egyptian Journal of Petroleum 2013, 22, (1), 43-51.
[30] Hannon, M.; Gimpel, J.; Tran, M.; Rasala, B.; Mayfield, S. Biofuels 2010, 1, (5), 763-784.
[31] Libessart, N.; Maddelein, M. L.; Koornhuyse, N.; Decq, A.; Delrue, B.; Mouille, G.; D'Hulst, C.; Ball, S. The Plant Cell 1995, 7, (8), 1117-1127.
[32] Wang, Z. T.; Ullrich, N.; Joo, S.; Waffenschmidt, S.; Goodenough, U. Eukaryotic Cell 2009, 8, (12), 1856-1868.

Chapter 4

Photocurrent-based Microalgal Farming Monitoring

Utilities of microalgal byproducts as bioenergy resources are critically affected by how to achieve large-scale farming in various local environments, especially in non-arable regions. As the biological process of microalgae (*i.e.,* growth and biomass production) is much more rapid than arable crops and critically affected by environmental conditions, real-time monitoring capabilities can be considered as one of the criteria facilitating microalgal farming success. Although commercialized sensors can be used to monitor physicochemical conditions including water acidity, temperature, and photon flux density, biological variables addressing the living systems (*i.e.,* metabolism and byproduct anabolism) are not simply characterized by commercially available on-line sensors, but rather through microscopic characterization as post-hoc in laboratory environments. Here, we suggest a new microalgal monitoring method capable of assessing cellular status and the culture media condition using a non-invasive, in-situ method. Our approach utilizes the photocurrent measurements on the light-gated ion channels of microalgal cells and light-enhanced photo-electrochemistry at the interface between electrode and culture media. In this chapter, we demonstrate a sensor prototype and an algorithm to correlate biological statuses that we applied to a macroscale bioreactor and validated the monitoring capabilities in aspects of farming variables of interest, such as cell number, metabolic activity, media acidity, and ion contents. In our proof-of-concept demonstration, the temporal dynamics of the photocurrent over the microalgae culture period showed that the analytical evaluation of photocurrents are highly correlated with cell conditions (*i.e.,* metabolic activity and population). Also, the photocurrent monitoring during high-value metabolite production period informed the dynamics of the metabolite accumulation in microalgae. This study indicates that the photocurrent-based cell monitoring method can be utilized as a strategic index for algal cultivation.

4.1. Introduction

Recently microalgae have been in the spotlight as a great source of bioenergy due to its excellent ability to capture light and atmospheric carbon dioxide and converting the resources into valuable biochemical energy byproduct [1-4]. Even with such promising attributes of microalgae as a bioenergy, however, there is still a great need for research to find a way to harvest microalgal biomass in a profitable manner and on a large scale for commercialization. The success of algal farming can be critically affected by a monitoring method that can be as frequent as possible (or continuous at best) to maximize the amount of byproducts of interest in the continuous biochemical procedures of the living microalgal cells. As microalga is a unicellular organism with a very short cellular cycle, the state of algae culture rapidly changes. Additionally, the microalgal metabolism of desired byproduct production is critically influenced by ever-changing environmental factors (*i.e.,* media and atmospheric condition) [5-8]. Thus, high-frequency monitoring is indispensable for successful and profitable algal culture on a large scale.

In general, the variables to be monitored during the microalgal culture are categorized in physical, chemical, and biological aspects. Although commercialized sensors can be used for the monitoring of physical and chemical variables, including pH, temperature, and photon flux density, monitoring of biological variables, which is the most crucial for microalgal farming relies on methods whose availability is currently limited to a laboratory environment. The followings are the exemplary equipment for the biological variables: 2D fluorometry, Raman spectrometry, NMR spectroscopy, GC-MS, HPLC, and pyrolysis [9-10]. This addresses that most of these methods require post-hoc characterization via a complicated, time-consuming, expensive, and lab-environmental procedures, causing a significant gap for pragmatic applications. It is evident that an inexpensive, in-situ, real-time, non-invasive monitoring system allowing to address the biological parameters would permit better controls of farming procedures, and thus achieve higher productivity in industrial applications.

In this regard, we proposed a new microalgal monitoring method based on an uncomplicated photocurrent measurement but capable of assessing comprehensive information from cell growth to production rate of high-value metabolite in a real-time, in-situ and non-invasive manner (Figure 4.1). The approach is designed to measure photocurrents originated from light-gated ion channels of a portion of microalgal cells in a bioreactor through external photonic excitation (Figure 4.2). In detail, photosynthetic microalgae have a light-gated ion channel (*i.e.,* a rhodopsin-ion channel hybrid) that contains light-isomerizable retinal chromophore. Light absorption of the retinal complex induces a conformation change from the all-trans-retinal (closed state) to 13-cis-retinal (open state), and it triggers an ionic flow resulting in photoreceptor current [11-14]. As the photocurrent is the intrinsic characteristic of living microalgae, photocurrent detection can potentially be an ideal rapid monitoring method for microalgal physiology fulfilling no requirement of complicated, time-consuming sample preparation.

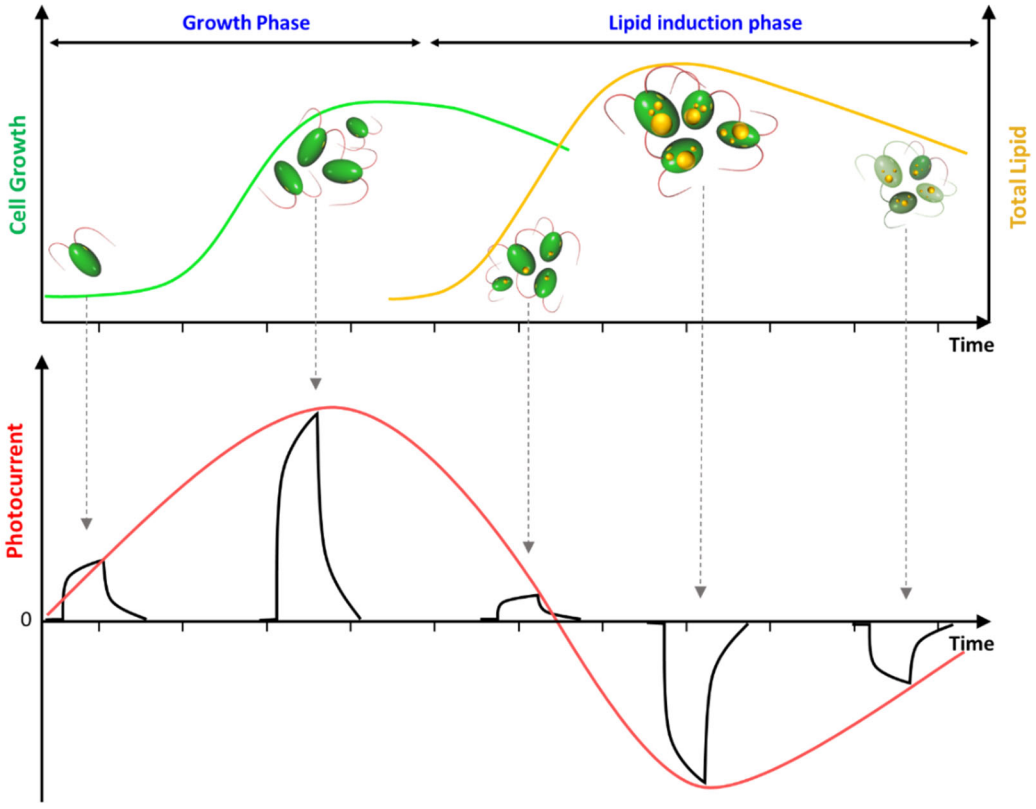

Figure 4.1. Schematic illustration of photocurrent-based microalgae culture monitoring. As the photocurrent is a unique signal from living microalgae, the photocurrent from the whole microalgae population is expected to have different values depending on the number and metabolic status of microalgae. Therefore, the photocurrent detection has potential as a monitoring method of whole microalgae culturing process, including cell growth and lipid induction phase.

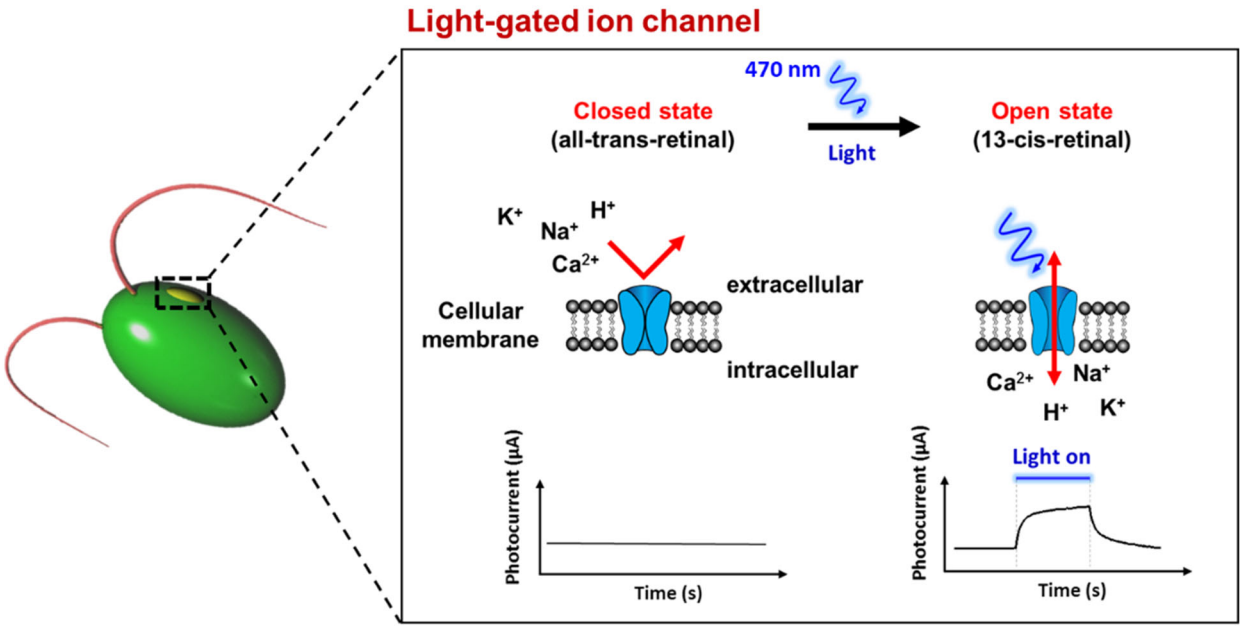

Figure 4.2. Schematic illustration showing how the light-gated ion channel of microalgae works. Upon light illumination, light-isomerizable retinal chromophore in light-gated ion channel changes its structure from all-trans to 13-cis, provides space for ions to pass through. Only positive ions are selectively passed through the channels, resulting in the current. This current is named as photocurrent because it is induced by light.

4.2. Design of the Photocurrent-based Cell/Media Monitoring System

A dual-compartment sensor system with the illuminators, as shown in Figure 4.3, was designed to measure light-induced electrophysiological responses of the microalgal population residing in a measurement chamber. The dual-compartment system consists of two chambers: one is for microalgae, and the other one is only for media, which are described as microalgae chamber and media chamber, respectively. They are separated by non-transparent, size-sieving porous membrane to keep the chemical composition of both chambers identically and to block the light illumination from the other side. Also, blue LEDs (470nm) are positioned across the electrodes for illumination, a means for generating photocurrent. Alternating illumination to each chamber across the transparent electrode with the corresponding voltage application is the basic operation to measure the photocurrent.

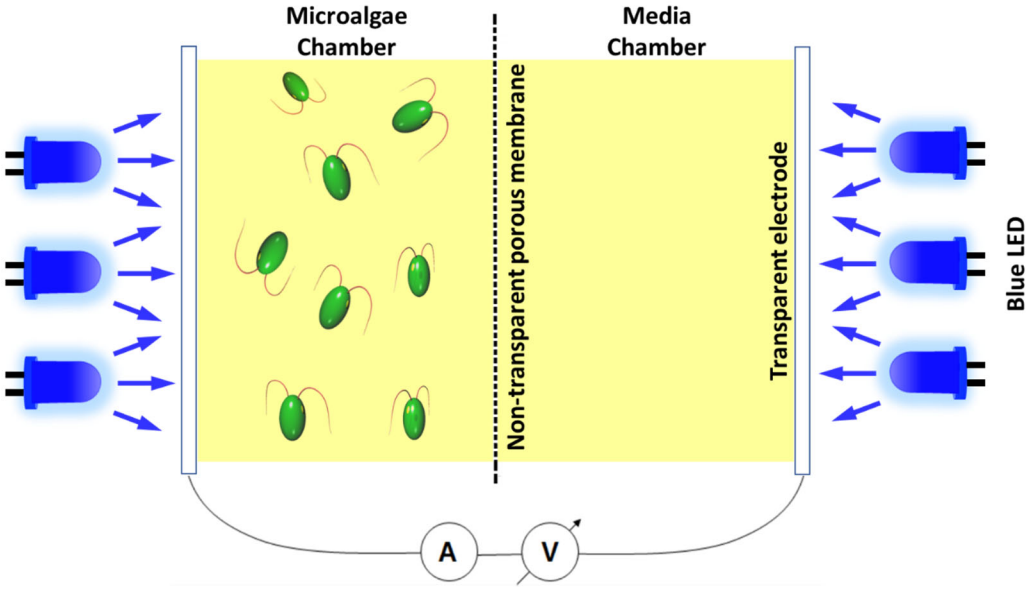

Figure 4.3. Design of the dual-compartment sensor for photocurrent-based cell/media monitoring. The sensor system consists of two chambers that are not completely separated and are electrochemically connected through the porous membrane. The two compartments named as cell chamber and media chamber are configured identically consisting of transparent electrode and blue LED except the existence of cell or not. The dual-compartment sensor, which permits the asymmetric positioning of the cell, enables not the only measurement of photocurrent from cells but also the analytical decoupling of mixed photocurrents into each component photocurrent originated from cell and media.

4.2.1 Characteristics of the Dual-Compartment Sensor System

The reasons why the sensor system consists of two compartments which permit the asymmetric positioning of cell can be explained as follows: (1) electrophysiological signals from microalgae can be measured only with the asymmetric positioning of the cells between two electrodes, and (2) compartmentalization of cell and media facilitates the decoupling of mixed photocurrent signal from the cells and media.

4.2.1.1 Geometric Asymmetry for Photocurrent Readout

Our dual-compartment sensor system is designed to measure photocurrent due to the asymmetry of cell location in the sensor module. If microalgae cells are positioned uniformly in the space between two electrodes, the electric signal from cells will be transmitted to both electrodes identically, compensating each other, and no resultant signal would be measured in the sensor system (Fig. 4.4A). On the other hand, if the cells are positioned asymmetrically between two electrodes, the cell-originated electric signal will be transmitted unequally to the two electrodes, and the difference provides the resultant electrical signal measured in the sensor module (Fig. 4.4B). For a detail analysis of extracellular electric signal measurement with two electrode system (Fig. 4.5A), a numerical simulation was applied using a governing equation of Nernst-plank equation which describes the flux of ions under the influence of both an ionic concentration gradient (∇c) and an electric field (E) (eq. 4.1). Here, $\boldsymbol{D_i, c_i, \mu_i, V, R_i}$ represent diffusion coefficient of specific ion, concentration of specific ion, ion mobility in the medium, local potential, and reaction rate of specific ion, respectively. We can consider the reaction rate as the transmembrane current of the microalgae upon the illumination.

$$\frac{\partial c_i}{\partial t} + \nabla \cdot (-D_i \nabla c_i - \mu_i c_i \nabla V) = R_i \qquad \text{(eq. 4.1)}$$

As shown in Figure 4.5B, the electrical readout is zero when the reaction occurs at the center (Blue). On the other hand, If the reaction occurs at the position close to the electrode, a non-zero electrical signal is obtained in the system (Red). Based on the simulation result, we can conclude that the two compartments system which permits the asymmetric positioning of the cells is indispensable for the photocurrent measurement.

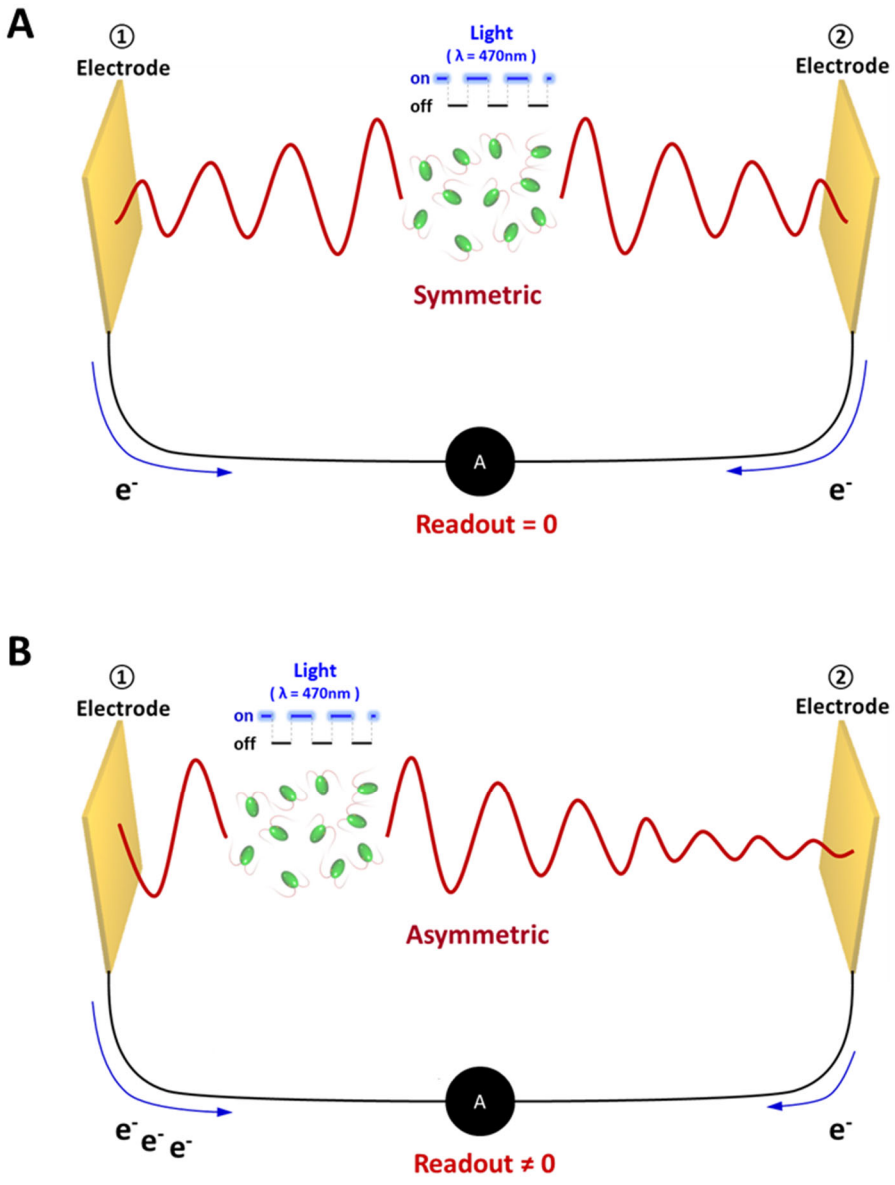

Figure 4.4. Schematic illustration showing how asymmetric cell distribution enables photocurrent measurement. Upon illumination, cations flow into the microalgae cell through the light-gated ion channel so that the surroundings lose their ionic balance and generate negative potential. In order to compensate for the ionic imbalance, the negative potential propagates as a waveform, which is known as volume conduction. When the non-zero charge density reaches the interface of the electrode, they cannot penetrate the electrode, but they can push free electrons in the electrode. As a result, the difference of the electron flows from two electrodes can be measured as current by the amperemeter. **(A)** In the case where the cells are located at the same distance between two electrodes, the non-zero charge density originated from cells decreases proportional to the travel distance, and it is transmitted symmetrically to both electrodes with the same value. Thus, electron flows from two electrodes compensating each other, and no resultant signal would be measured in the system. **(B)** In the case where the cells are located at the different distances between the two

electrodes, a higher charge density is delivered to the electrode close to the cell. Therefore, the flow of electrons from each electrode toward the wire shows different values, and the difference is measured as a current by an amperemeter.

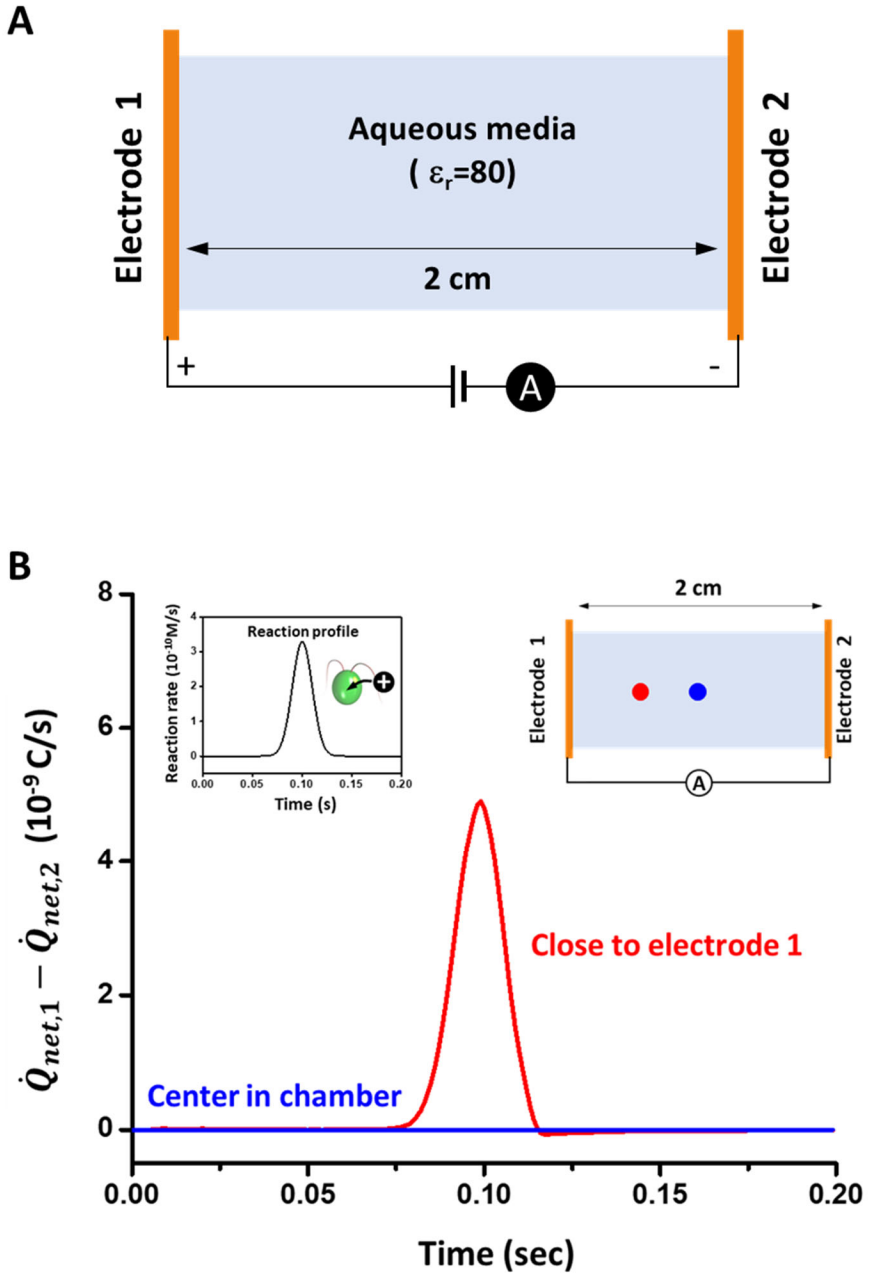

Figure 4.5. Schematic illustration of the model system used in the simulation, and its analytical calculations. **(A)** The model system consists of two opposing electrodes spaced 2 cm apart and connected by wires, with a cell culture medium filled between them. **(B)** Reaction position-dependent electrical readouts for the scenarios shown in upper insets. The electrical signal is measurable (red line) only when the reaction occurs at an asymmetric position (red dot) between the two electrodes.

4.2.1.2 Decoupling of Signals from Cell and Media

Upon the light illumination, two different kinds of electric signals are generated simultaneously from the media containing microalgae cells faced with electrodes. One is from light-gated ion channels of microalgal cells, and the other one is from a light-enhanced, electrochemical reaction between electrolyte and electrodes (Fig. 4.6).

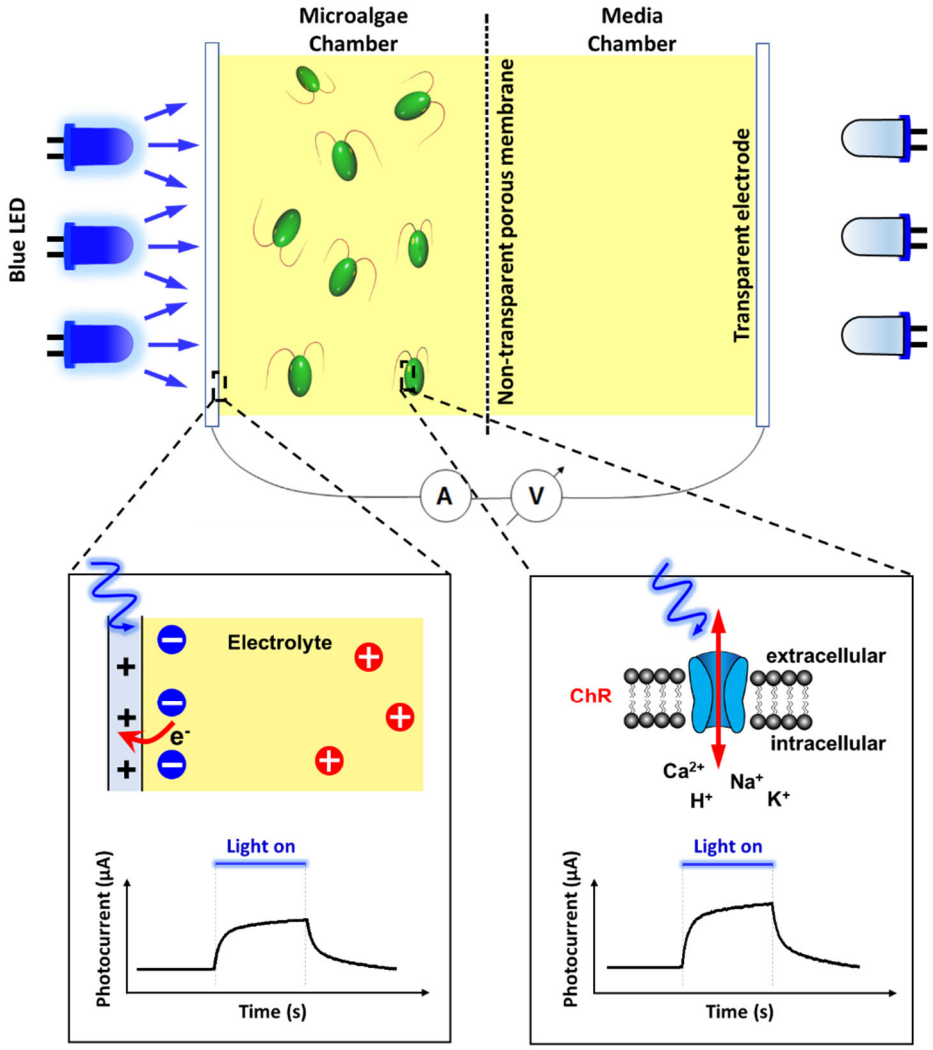

Figure 4.6. Schematic illustration showing two different photocurrents generated during cell chamber illumination. One is due to the flow of positive ions through the light-gated ion channels of microalgae cells (bottom right), and the other one is from light-enhanced, electrochemical reaction between electrolyte and electrodes (bottom left). The light illumination can vary the energy level of the holes and electrons in the electrode, causing a different type of photocurrent as a result of the photoelectrochemical reaction.

The signals are mixed and hard to distinguish from each other. Furthermore, the concentration of cell and media that affect photocurrent are changing simultaneously in the opposite way during the cell culture period, making data analysis more difficult. Photocurrent from the cell is expected to increase as time passes due to the cell growth. On the other hand, the photocurrent from media is expected to decrease due to the reduction of ion concentration. Which means, they contribute to the total photocurrent destructively, making the total photocurrent uninformative. Thus, the decoupling of mixed total photocurrents from cell and media is indispensable for data analysis, and it is expected to address multi-aspect culture variables more intuitively. With the dual-compartment system, two types of photocurrents can be analytically decoupled, as shown in Figure 4.7. If we illuminate the light only the microalgae chamber side, the generated photocurrent will be the combination of the signals from cell and media. On the other hand, the photocurrent originated solely from media will be produced upon illumination on the media chamber side. By subtracting these two photocurrents, we can get the signals from microalgae cells enabling monitoring of cell physiology.

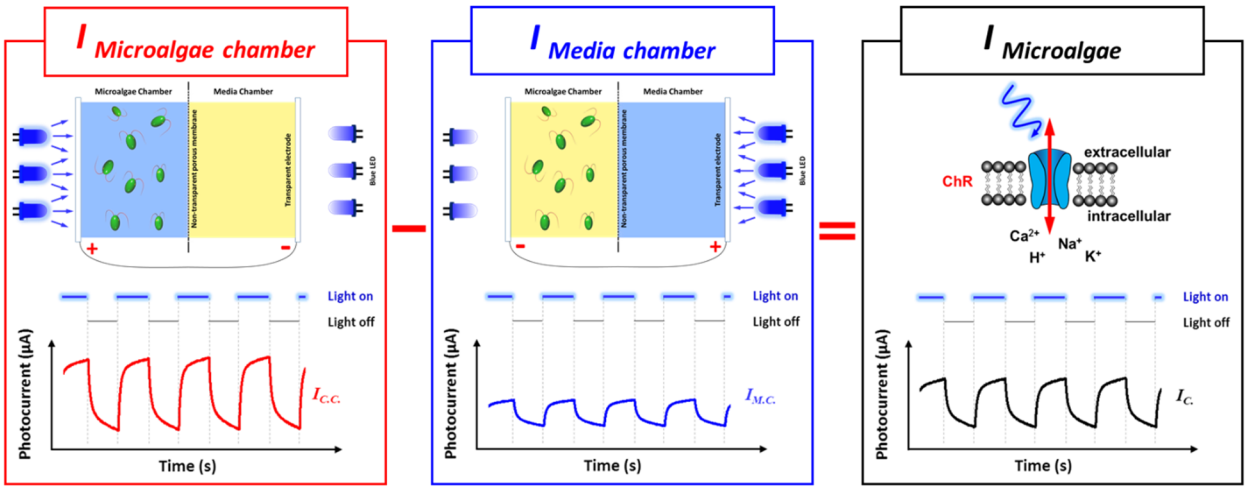

Figure 4.7. Schematic illustration showing a decoupling mechanism of cell-originated photocurrent from mixed photocurrent of cell and media using a dual-compartment system. The cell chamber is devised to measure the electrical signal mixed with the two types of photocurrents from cell and media (left). On the other hand, the media chamber is designed to detect only the photoelectrochemical reaction originated from media (middle). Thus, the difference in photocurrent measured from both chambers will be the photocurrent generated from the cell (right).

4.2.2 Benefit of the Potential Bias

In order to amplify the photocurrent signal in the sensor system, potential bias was considered in the sensor design. We hypothesized that the ions' movement rate could be increased between two electrodes with the aid of the electric field and resulting in amplified current as the current is defined as dq over dt. For a detailed analysis of potential bias effect on extracellular electrical signal measurement with the two-electrode system, a numerical simulation was applied using the same governing equation and model system as described in section 4.2.1.1(eq. 4.1 & Fig. 4.5A). As shown in Figure 4.8, the signal increases as the applied voltage increases. With the

voltage of 0.6, the signal is amplified about 20 times as compared to the zero biased case. Thus, based on the simulation result, we can conclude that we can get the amplified photocurrent signal with the aid of potential bias.

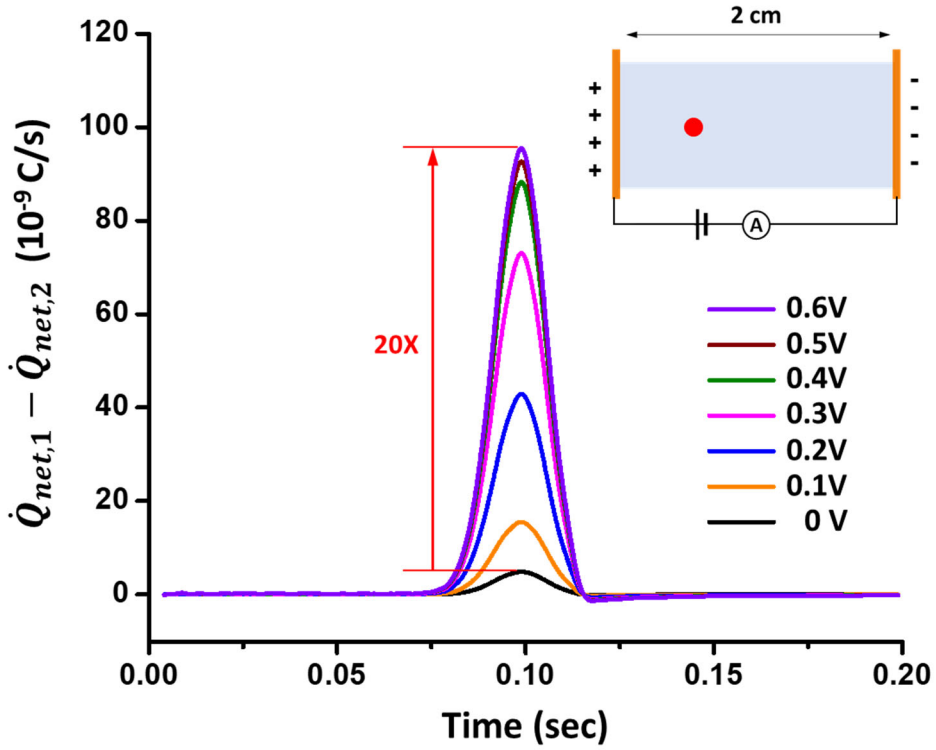

Figure 4.8. Electric signal intensities calculated with the potential bias in the two external electrodes system. The calculation shows how the electrical signal that can be measured in the system changes as the potential bias is increased from 0 to 0.6V by 0.1V. As the applied voltage increases, the intensity of the electrical signal also increases. At 0.6 V, the electric signal is amplified about 20 times as compared with the case of 0V, and it seems to be almost saturated. All calculations assumed that the reaction has occurred at the red dot (near the left electrode). as shown in the upper inset.

4.3. Fabrication of the Dual-Compartment Sensor System

To realize the dual-compartment sensor, the system was fabricated with 7 components, as described in Figure 4.9. The dual-compartment system consists of two chambers, cell and media chamber, as aforementioned. For the two chambers, a cylindrical shell made of acrylic plastic was used. They are separated by a black polycarbonate porous membrane which has a pore size of 2 μm so that the cells which have a size of about 10 μm cannot pass through, but the electrolytes are in equilibrium in two chambers. The end of the chambers are enclosed by gas permeable PDMS sheet and ITO-coated PET for the electric signal measurement. Both PDMS sheets and ITO-coated PET are transparent for the light illumination on each chamber. All the components were assembled using an uncured-PDMS.

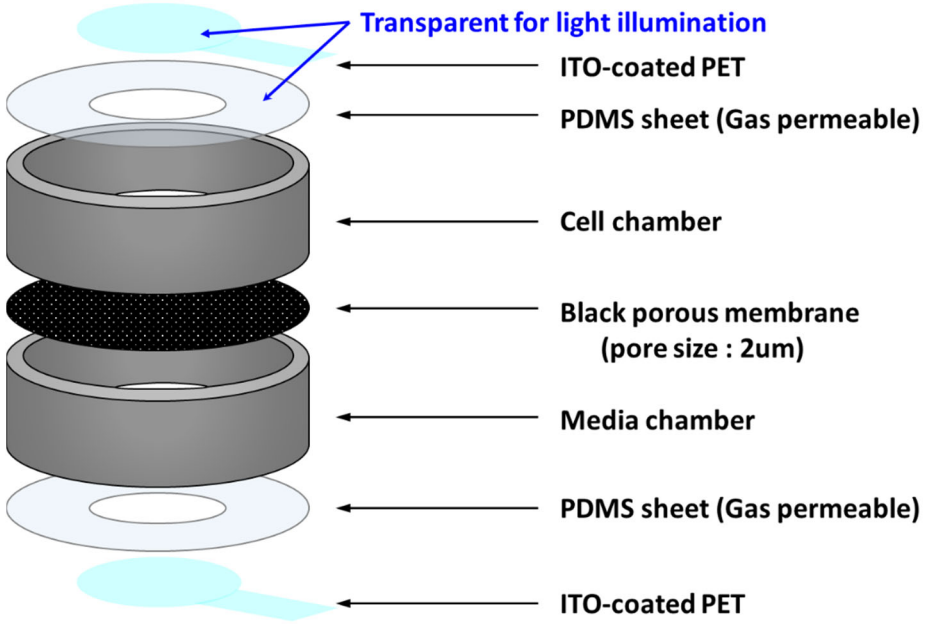

Figure 4.9. Schematic illustration showing each component of the dual-compartment sensor system from top to bottom. The symmetrical dual compartment system consists of seven components, each of which was prepared using a laser cutter and assembled all together using an uncured PDMS.

4.4. Proof-of-concept Demonstration of the Photocurrent-based Characterization

In this section, we will present conceptual demonstrations of the photocurrent-based microalgae detection. Further, for additional biochemical interest, we will investigate the potential correlation between the photoelectrochemical reaction and the media composition, which can potentially assess the change of the media condition during the culture period.

4.4.1 Characterization of Cell Concentration through a Photocurrent Measurement

As the biological activity of the light-gated ion channels is the main element of the detection, it can be hypothesized that the number of microalgal cells can affect the amplitude of the photocurrent. In algal farming, biomass or cell concentration is one of the top priorities of the biological parameters to be monitored. If the photocurrent amplitude distinguishes the cellular population number in the range of a typical growth pattern (*i.e.*, lag-phase, exponential, and stagnation stages), the proposed photocurrent detection holds great potential for monitoring the microalgal population. As a proof-of-concept demonstration, the photocurrent was measured using samples prepared with different cell densities within the range of a typical growth pattern. For the samples, four different cell densities, 10, 100, 1000, 10000 cells/μl, were prepared based on the *Chlamydomonas reinhardtii*' growth curve. All the cells tested in this experiment are in the same growth phase, but the numbers of cells varied to investigate whether the photocurrent represents the cellular population. As shown in Figure 4.10A, the photocurrent variation was successfully monitored depending on the cell density. The photocurrent not only varies according to the cell

density but also shows a linear correlation with the log scale of the cell concentration (Fig. 4.10B). The linear correlation indicates a strong association between two variables, cell density, and photocurrent. Also, another noticeable point in the experiment is detection sensitivity in the low and high cell concentration. Because, in the case of low concentration like 10/µl, it is not detectable with typical optical density measurement. Also, in the case of a high concentration like 10,000/µl, the cell should be diluted for the accurate optical density measurement. However, our result shows that the photocurrent can be measured without any treatment at the low or high density of cells.

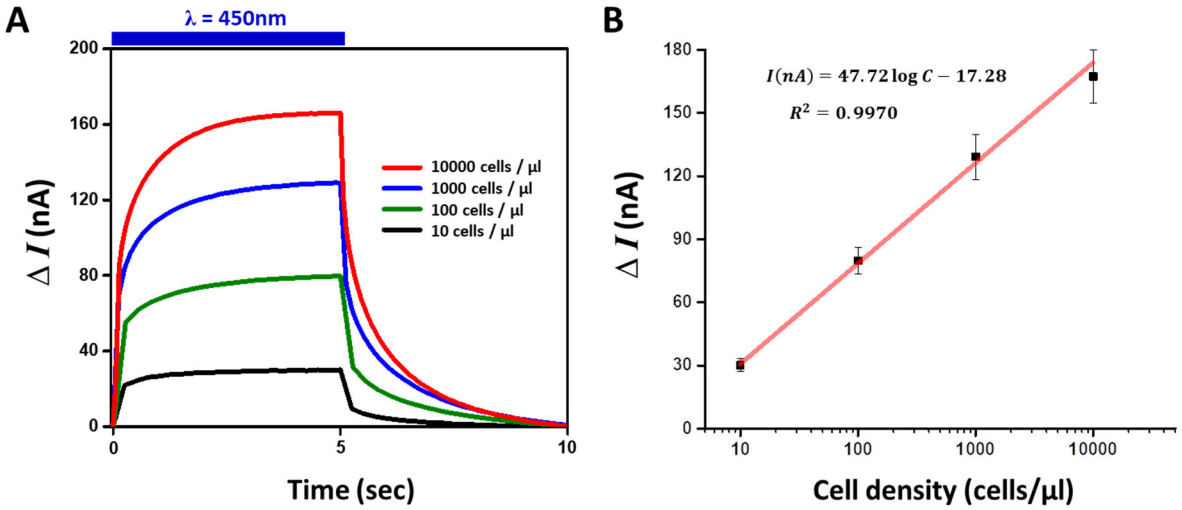

Figure 4.10. Photocurrents depending on the cell density. **(A)** Measured photocurrents from various cell concentrations (10, 100, 1000, 10000 cells/ µl) which are in the range of typical microalgae growth. The photocurrent increases with increasing cell concentration. **(B)** Correlation between cell concentration and amplitude of photocurrent. The amplitude of photocurrents is linearly correlated with the log scale of the cell density.

4.4.2 Characterization of Cell Culture Media through Photo-electrochemistry

In microalgal farming, not only the cell physiology but also the media condition is variables of interest. Inorganic cation concentrations and the pH of media are changed during the cell culture, and these parameters are directly linked with biomass productivity. Photocurrent detection will be beneficial to assess tactical strategies in culture if it can inform chemical variables. In this experiment, ITO was chosen as a transparent electrode for the light illumination. As the excitation wavelength for cellular ion channels is close to the ITO bandgap, the light illumination can vary the energy level, causing a different type of photocurrent as a result of the photoelectrochemical reaction. As the electrochemical reaction is a function of the electrolyte composition and the pH, the photoelectrochemical reaction will vary during the cell culture period. Prior to the proof-of-concept demonstration, we observed how the electrolyte concentration and pH of the media changes during microalgae cultivation. As shown in Figure 4.11A, the acidity of the media was changed to basic, and the ion concentration in media was decreased over time. Based on this result, various media composition was prepared by changing pH and ionic concentration from a normal microalgae culture media. As a proof-of-concept demonstration, the photocurrent was measured using samples with different media compositions. As the composition changed, the corresponding

photocurrents showed dynamic variation (Fig. 4.11B). This result shows the potential of the photocurrent as a monitoring method of media composition.

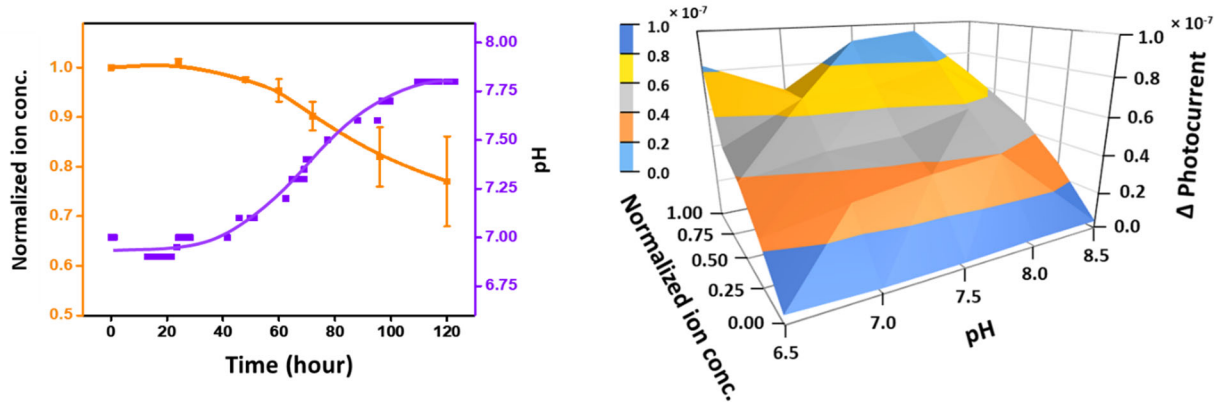

Figure 4.11. Characterization of cell culture media through photoelectrochemical response. **(A)** Changes in ion concentration and pH of the media during cell culture period. As time passes, the ion concentration in media decreases, and the pH changes from neutral to basic. **(B)** Heatmap of the photocurrent amplitude depending on ion concentration and pH of the media. Corresponding photocurrents shows dynamic variation as the composition of the artificial media changes. Artificial media samples having various composition of ion concentration and pH were prepared based on the graph (A).

4.5. Photocurrent-based Growth Monitoring

As discussed, the photocurrent amplitude can distinguish the cellular population number in the range of a typical growth pattern by showing the linear correlation with the log scale of cell concentration. However, the possibility of the cell culture monitoring was not sufficiently proven as all the cells tested in that experiment were in the same growth phase. Because, not only cell number but also cell growth phase (*i.e.*, lag-phase, exponential, and stationary phase) is changed during the cell culture period. In general, microalgal farming is divided into two major stages. The first stage is for population growth, and the second one is for the induction of high-value metabolites, as they would not be growing during the induction stage. In this section, we will demonstrate the photocurrent-based in situ microalgae monitoring during the growth stage.

Following a conventional cell culture protocol, microalgae cells were inoculated at a concentration of 10 cells per µl, and illuminated with a 5000K full spectrum of 100 µmol $m^{-2}s^{-1}$ at 28 °C. The media chamber of the photocurrent sensor system was filled with TAP media but without the cells. During a typical 5-day culture for the population increase, in situ photocurrent measurement was applied about every 12 hours on microalgae culturing with the opened photocurrent sensor system. For the photocurrent generation, the train of pulsed blue light (5s on followed by 5s off) was illuminated only on the designated chamber. Only the media chamber was illuminated when measuring photocurrent from media, and only the cell chamber was illuminated when measuring mixed photocurrent from cell and media. In order to reduce the time difference

between measured two photocurrents from cell and media chamber, they were measured in a row. Also, the potential bias of 0.6V was applied between two ITO electrodes whenever measuring the photocurrents for the signal amplification. The photocurrent vs time curves were recorded by an electrochemical station (CHI, USA). Along with the taking of the photocurrent measurements over a series of days, the cell population and media composition were also characterized in order to establish correlations between the photocurrents and the cell growth.

Figure 4.12A shows the temporal progress of the measured photocurrent from each chamber (red line for cell chamber and blue line for media chamber) at a representative time (①:1h, ②:34h, ③:59h, ④:83h, ⑤:105h). Both photocurrents change over time, but the photocurrent from the cell chamber changes more dynamically than that of the media chamber. The amplitude change along the time was summarized as plotted in Figure 4.12C. The change shows the totally different patterns in the two photocurrents. The photocurrent from the cell chamber shows a peak around time point ③, on the other hand, that of the media chamber shows an M-shape pattern which has a valley around time point ③. The M-shape pattern can be explained by following the trace of media composition change which is measured during the cell culture period in the contour map of photocurrent amplitude attained from conditioned media with various pH and ionic concentration (Fig. 4.11B).

For the most crucial part, cell-derived photocurrent, the analytical calculation as described in section 4.2.1.2 was performed using the two photocurrents in the Figure 4.12A, and the temporal progress of cell-derived photocurrent was obtained as shown in Figure 4.12C. Evident amplitude change of the cell-derived photocurrent along the time was plotted, and it was overlaid with the cell growth curve in Figure 4.12D to figure out the correlation between the photocurrents and the cell growth. The photocurrent amplitude vs time curve shows a Gaussian-like shape having a peak at the time point ③. I found that the peak was matched to the later stage of the exponential growth, where the cell shows the highest growth rate in the high cell concentration region. An obvious question arises of why the photocurrent is decreased in the stationary phase even though the total cell count has increased than the exponential growth phase. We reasoned that the photocurrent is an integrated result of not only the total cell number but also the metabolic activity of the cells. We hypothesized that the expression level of the light-gated ion channel would be the highest in the exponential growth phase, where the cells have the highest metabolic activity. As the photocurrent is generated by the activation of the light-gated ion channel, it is obvious that higher photocurrent can be produced if the cells express more light-gated ion channels on their bodies. The expression level of the light-gated ion channels along culture time was characterized through qPCR of the extracted mRNA from microalgae cells which were sampled every 12 hours. The expression of the light-gated ion channels shows a peak in the exponential growth phase as expected. The question above mentioned can be answered by integrating two factors, cell number and expression level of light-gated ion channels. Cell density increases over time, which would supposedly increase photocurrent, but it is compensated and finally decreased by the declining expression level of light-gated ion channels per cell in the stationary phase.

As the photocurrent can provide comprehensive information regarding cell number and cell activity, which is the essential information in the cell culture, the photocurrent measurement can be a great way to monitor microalgae culture. However, even though *Chlamydomonas reinhardtii* is the popular model organism for the microalgae study [15-17], it alone is not enough to represent the whole microalgae population. To assess the universality of the photocurrent-based microalgae growth monitoring method, another popular strain of microalgae, *chlorella*, was also

tested. We observed a fairly consistent result with the case of *Chlamydomonas*. This presents a powerful potential of the photocurrent as a cell growth monitoring.

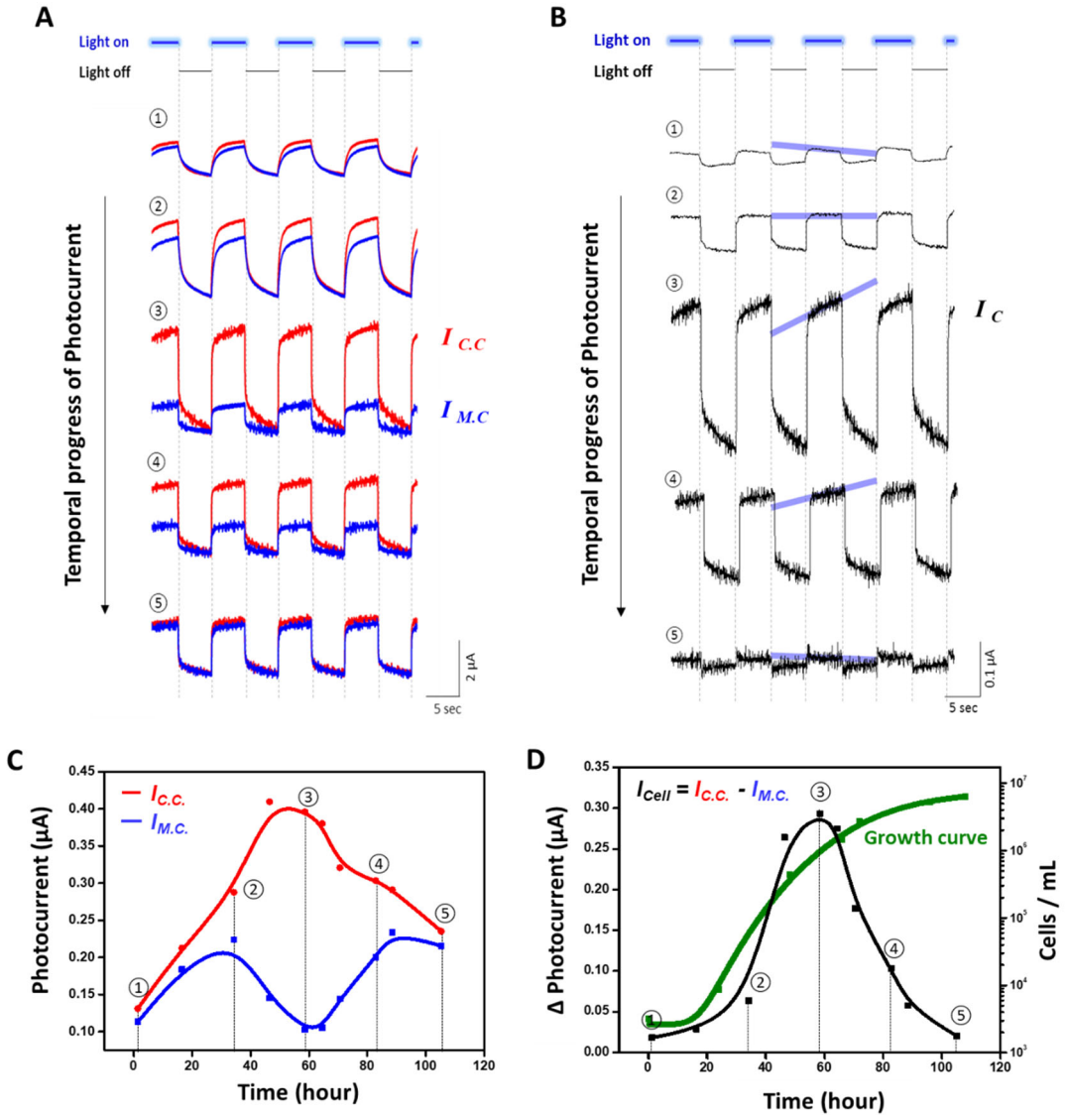

Figure 4.12. Photocurrent monitoring throughout microalgae cultivation, and it's correlation with cell growth. **(A)** Temporal progress of the measured photocurrent during cell culture period upon illumination of each chamber at a representative time (①:1h, ②:34h, ③:59h, ④:83h, ⑤:105h). $I_{C.C}$ (red line) and $I_{M.C}$ (blue line) represent photocurrent from the cell chamber and photocurrent from the media chamber, respectively. **(B)** Temporal progress of cell-derived photocurrent (I_C) obtained by analytic calculation of two photocurrents, $I_{C.C,}$ and $I_{M.C}$. **(C)** Summarized plot for the amplitude changes of the photocurrents from each chamber along the culture time. **(D)** Overlaid plot of the amplitude changes of cell-derived photocurrent along the culture time and its corresponding cell growth.

4.6. Photocurrent-based Lipid Induction Monitoring

The most important stage in the microalgae culturing is the induction of high-value metabolites. Depending on the strains of microalgae, a variety of different metabolites are produced at this stage, like lipid, antioxidant, carotenoids, proteins, and vitamins [18-22]. Among these substances, lipid is the most common and desirable high-value metabolites in microalgae culturing [23]. So, in this section, we will focus on lipid induction monitoring. In situ and non-invasive are the key factors for effective monitoring of the lipid induction in microalgae. As the photocurrent fulfills these requirements, photocurrent-based monitoring will be an ideal way to determine harvest time if it can inform the dynamics of the lipid induction in microalgae cells during the culture period. In order to test whether the photocurrent can capture the information regarding lipid induction dynamics, photocurrent measurement was applied during the lipid induction stage. For the lipid induction, the cells in the initial saturation stage were inoculated with the nitrogen-depleted media. They then incubated at 28 °C under continuous illumination of 100 μmol m^{-2} s^{-1}. The media chamber was also filled with nitrogen-depleted TAP media but without the cells. The in-situ photocurrent measurements were applied every 12 hours for 9 days on lipid-induced microalgae culturing with the opened photocurrent measurement system.

Figure 4.13A shows the temporal progress of the measured photocurrent from each chamber (red line for cell chamber and blue line for media chamber) at a representative time (①:10h, ②:58h, ③:106h, ④:164h, ⑤:227h). The noticeable thing in this data in comparison with the case of growth monitoring is that the relative amplitude of the photocurrents from two chambers have changed with each other. As shown in Figure 4.13C, the summarized plot of the amplitude change along the time, the photocurrent amplitude of the media chamber becomes higher than that of the cell chamber. In contrast, it showed the opposite trend in growth monitoring. Thus, the cell-derived photocurrent obtained through the difference between the two measured photocurrents has a negative value, as described in Figure 4.13B. One possible (The most convincing) scenario explaining the phenomena is that the ionic flow through the light-gated ion channel during the lipid induction phase is outward movement, as opposed to the case of the growth phase. According to the literature, high intracellular pH is common in actively dividing prokaryotic and eukaryotic cells, while low intracellular pH is typical in resting cells with low metabolic activity. Moreover, the ionic flow through the light-gated ion channels of microalgae is the passive transport of cations. Thus, during the growth stage, when the microalgae are actively dividing, they are expected to have high intracellular pH, resulting in an influx of cations across the cellular membrane through the light-activated ion channels. On the other hand, during the lipid induction stage, when the microalgae stop the cell growth/division and begin to accumulate lipid bodies, they are expected to have low intracellular pH, resulting in an efflux of cations.

As shown in Figure 4.13D, the amplitude change of cell-derived photocurrent was also dynamic during the lipid induction period as in the growth stage, and it showed a peak at time point ③. In order to discover the correlations between the photocurrents and the lipid accumulation, the amplitude of the photocurrent was compared with the lipid amounts in the cells which is analyzed by the conventional lipid staining method using a Nile red (Fig. 4.13E & F). Interestingly, the maximum amount of lipid accumulation in the cell was also observed at the time when the photocurrent amplitude reached its maximum.

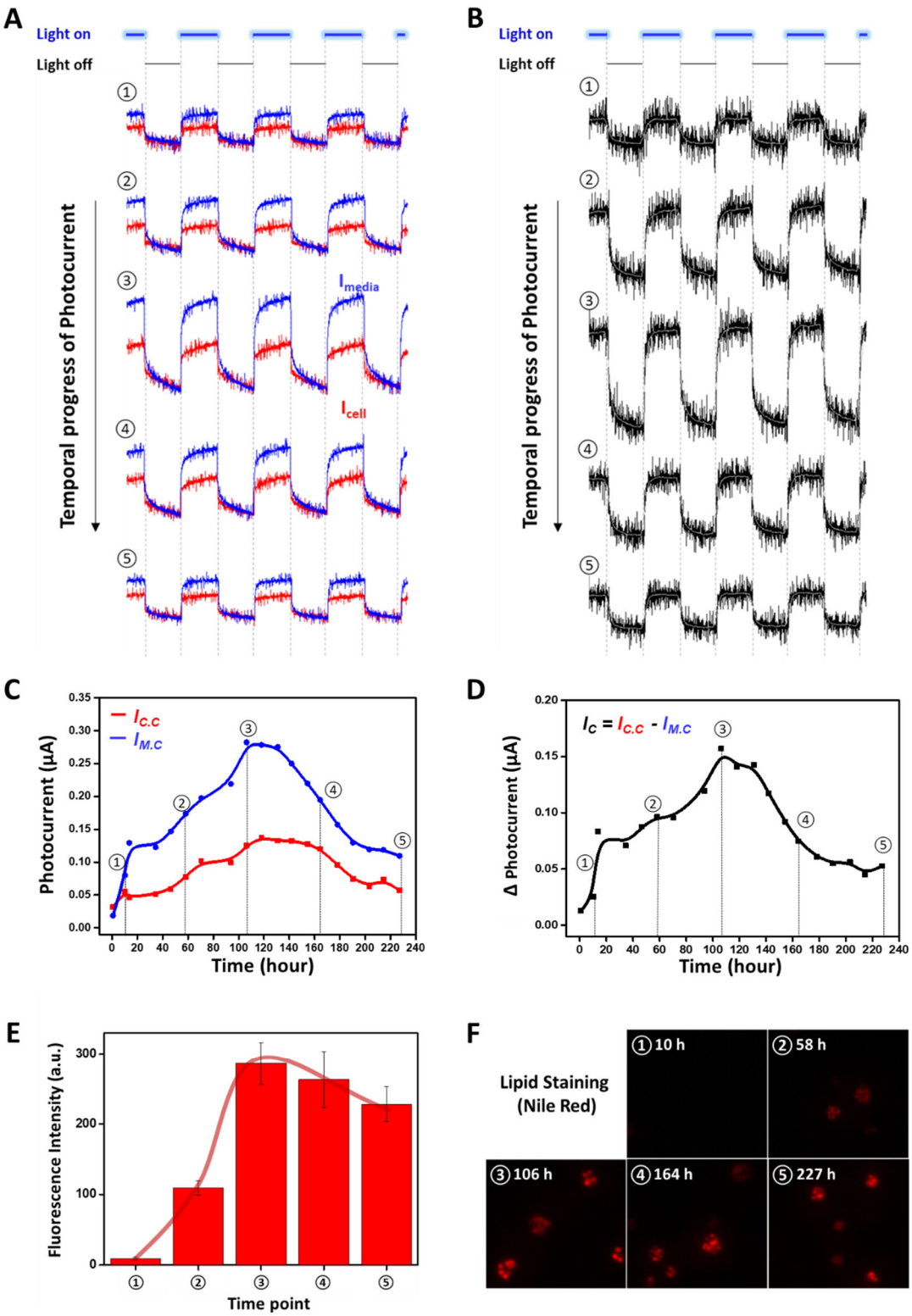

Figure 4.13. Photocurrent monitoring throughout the lipid induction stage, and its correlation with lipid contents in the cell. **(A)** Temporal progress of the measured photocurrent during the lipid induction period upon illumination of each chamber at a representative time (①:10h, ②:58h, ③:106h, ④:164h, ⑤:227h). $I_{C.C}$ (red line) and $I_{M.C}$ (blue line) represent photocurrent from the cell

chamber and photocurrent from the media chamber, respectively. **(B)** Temporal progress of cell-derived photocurrent (I_C) obtained by analytic calculation of two photocurrents, $I_{C.C}$ and $I_{M.C}$. **(C, D)** Summarized plot for the amplitude changes of the photocurrents from each chamber and that of calculated cell-derived photocurrent along the lipid induction time. **(E)** Fluorescence intensity of stained lipids in the cell, indicating the amount of lipid accumulated along the time. **(F)** Fluorescence image of the lipid-stained microalgae sampled at a representative time.

We reasoned that the increase in photocurrent until the lipid content in the cell reaches its peak is due to an increase in the electrochemical gradient across the cell membrane. According to the literature, we can assume that the intracellular pH of microalgae will decrease during the lipid accumulation period. Even if the decrease in intracellular pH is subtle, it can be expected that the electrochemical gradient across the cell membrane will increase gradually since the pH measurement in media shows a rapid increase during the lipid induction period. As the electrochemical gradient is the driving force of the ionic current through the light-gated ion channel, the photocurrent becomes more significant as the electrochemical gradient increases.

On the other hand, we assumed that the reason why the photocurrent declines as the amount of lipid in the cell decreases is that the integrity of the cell membrane is impaired, resulting in lipid leakage and destruction of the electrochemical gradient across the cell membrane. Under stress condition, the microalgae cell start to accumulate lipid as a reserve source of carbon and energy to endure adverse environmental condition. During this period, lipid metabolism is known to change from membrane lipid synthesis to neutral lipid body storage resulting in damage to the cell membrane. Therefore, after the threshold, it can be assumed that the integrity of the cell membrane begins to be impaired, leading to a decrease in photocurrent due to a collapsed electrochemical gradient as well as a reduction in intracellular lipid due to the leakage of lipid body. In fact, the amount of extracellular lipids was increased rapidly since the photocurrent starts to decrease, which supports the above assumption.

Reference

[1] Baicha, Z.; Salar-García, M. J.; Ortiz-Martínez, V. M.; Hernández-Fernández, F. J.; de los Ríos, A. P.; Labjar, N.; Lotfi, E.; Elmahi, M., A critical review on microalgae as an alternative source for bioenergy production: A promising low cost substrate for microbial fuel cells. *Fuel Processing Technology* **2016,** *154*, 104-116.

[2] Menetrez, M. Y., An Overview of Algae Biofuel Production and Potential Environmental Impact. *Environmental Science & Technology* **2012,** *46* (13), 7073-7085.

[3] Rodionova, M. V.; Poudyal, R. S.; Tiwari, I.; Voloshin, R. A.; Zharmukhamedov, S. K.; Nam, H. G.; Zayadan, B. K.; Bruce, B. D.; Hou, H. J. M.; Allakhverdiev, S. I., Biofuel production: Challenges and opportunities. *International Journal of Hydrogen Energy* **2017,** *42* (12), 8450-8461.

[4] Singh, A. K.; Singh, M. P., Importance of algae as a potential source of biofuel. (1165-158X (Electronic)).

[5] Abo Bodjui, O.; Odey Emmanuel, A.; Bakayoko, M.; Kalakodio, L., Microalgae to biofuels production: a review on cultivation, application and renewable energy. In *Reviews on Environmental Health*, 2019; Vol. 34, p 91.
[6] Gatamaneni, B. L.; Orsat, V.; Lefsrud, M., Factors Affecting Growth of Various Microalgal Species. *Environmental Engineering Science* **2018,** *35* (10), 1037-1048.
[7] Juneja, A.; Ceballos, M. R.; Murthy, S. G., Effects of Environmental Factors and Nutrient Availability on the Biochemical Composition of Algae for Biofuels Production: A Review. *Energies* **2013,** *6* (9).
[8] Mata, T. M.; Martins, A. A.; Caetano, N. S., Microalgae for biodiesel production and other applications: A review. *Renewable and Sustainable Energy Reviews* **2010,** *14* (1), 217-232.
[9] Han, Y.; Wen, Q.; Chen, Z.; Li, P., Review of Methods Used for Microalgal Lipid-Content Analysis. *Energy Procedia* **2011,** *12*, 944-950.
[10] Lee, T.-H.; Chang, J.-S.; Wang, H.-Y., Current developments in high-throughput analysis for microalgae cellular contents. *Biotechnology Journal* **2013,** *8* (11), 1301-1314.
[11] Deisseroth, K.; Hegemann, P., The form and function of channelrhodopsin. *Science* **2017,** *357* (6356), eaan5544.
[12] Hegemann, P.; Moglich, A., Channelrhodopsin engineering and exploration of new optogenetic tools. (1548-7105 (Electronic)).
[13] Nagel, G.; Ollig, D.; Fuhrmann, M.; Kateriya, S.; Musti, A. M.; Bamberg, E.; Hegemann, P., Channelrhodopsin-1: A Light-Gated Proton Channel in Green Algae. *Science* **2002,** *296* (5577), 2395.
[14] Taylor, A. R.; Brownlee, C.; Wheeler, G. L., Proton channels in algae: reasons to be excited. *Trends in Plant Science* **2012,** *17* (11), 675-684.
[15] Harris, E. H., CHLAMYDOMONAS AS A MODEL ORGANISM. *Annual Review of Plant Physiology and Plant Molecular Biology* **2001,** *52* (1), 363-406.
[16] Kou, Z., Fluorescent measurement of lipid content in the model organism Chlamydomonas reinhardtii. *Journal of applied phycology* **2013,** *v. 25* (no. 6), pp. 1633-1641-2013 v.25 no.6.
[17] Griesbeck, C., Kobl, I. & Heitzer, Chlamydomonas reinhardtii**.** *M. Mol Biotechnol* **2006**, 34: 213.
[18] Barkia, I.; Saari, N.; Manning, S. R., Microalgae for High-Value Products Towards Human Health and Nutrition. *Mar Drugs* **2019,** *17* (5), 304.
[19] de Morais, M. G.; Vaz, B. d. S.; de Morais, E. G.; Costa, J. A. V., Biologically Active Metabolites Synthesized by Microalgae. *BioMed Research International* **2015,** *2015*, 15.
[20] Perez-Garcia, O.; Escalante Fm Fau - de-Bashan, L. E.; de-Bashan Le Fau - Bashan, Y.; Bashan, Y., Heterotrophic cultures of microalgae: metabolism and potential products. (1879-2448 (Electronic)).
[21] Pignolet, O.; Jubeau S Fau - Vaca-Garcia, C.; Vaca-Garcia C Fau - Michaud, P.; Michaud, P., Highly valuable microalgae: biochemical and topological aspects. (1476-5535 (Electronic)).
[22] Pulz, O.; Gross, W., Valuable products from biotechnology of microalgae. (0175-7598 (Print)).
[23] Harwood, J. L.; Guschina, I. A., The versatility of algae and their lipid metabolism. *Biochimie* **2009,** *91* (6), 679-684.

Chapter 5

Concluding Remarks

Today we are facing a severe problem of the energy crisis and global warming, which has been made us realize the urgency of developing sustainable and eco-friendly energies. Among potential resources of next-generation energies, microalgae are being attracted a lot of attention from researchers due to its enormous unique advantages which cannot be achieved with other resources as follows; high productivity, non-competing with human resources (e.g., freshwater and fertile land), diverse metabolic capability, energy-rich hydrocarbon contents, and net-zero emission of carbon dioxide. Extensive research on microalgae over the last couple of decades has deepened the biological understanding of the organisms and has raised its possibility as the next-generation biofuels. However, still, microalgae-based biofuels are economically less-competitive than other cheap fossil-based fuels, and more practical researches are needed to address them.

Over the four main chapters, we discussed new approaches utilizing BioMEMS, optics, and electronics for high-throughput screening of superior microalgae species, and in-situ monitoring of the microalgae cultivation process in real-time. Although numerous studies have been conducted to obtain superior species, it has been focused mainly on the development of new strains through genetic engineering. Unfortunately, it has been overlooked to develop technologies for fast and effective screening of superior species. Thus, researchers have consumed a lot of energies in terms of human, resources, and time to screen superior ones from hundreds of thousands of natural and genetically engineered strains. Moreover, even in the case of the superior strain selected by spending such a lot of energy, the high yield is not always guaranteed in every environment because its productivity is greatly affected by the surrounding environment. Besides, microalgae have a short life cycle, which leads to a sharp change in their conditions than other crops even with small fluctuations in the surrounding environment. Therefore, it is crucial to monitor the process of cultivation as frequent as possible in each environment when selected microalgae strains are applied to mass production, but unfortunately, this also has been overlooked. Real-time monitoring of microalgae growing and energy-carrier production according to the fluctuations in the surrounding environmental conditions will enable timely production management and consequentially lead to high productivity.

Therefore, the new approaches we have presented in this thesis are expected to provide a step closer to the realization of microalgae as next-generation energy by contributing to the superior strain selection and production management, which have been considered two of the major bottlenecks in commercializing microalgae-based biofuel.

One of the ultimate goals of my research is to implement of autonomous online microalgae monitoring sensor to extensive microalgae cultivation in the field. For algae-based biofuels to be realized as next-generation energy, mass production of microalgae should be carried out over vast areas (e.g., hundreds to thousands of hectares). Besides, attempts are also being made to grow microalgae cells on desert or ocean owing to its merit of being able to grow in non-arable land. Because such vast cultivation areas, desert, or sea are not facilitating human access, autonomous online monitoring will be an essential part of realizing algae-based biofuel.

For application to field photobioreactors, a microalgae monitoring sensor system consisting of two units is suggested as shown in Figure 5.1. As a freely floating sensor immersed in a photobioreactor, the small-sized photocurrent sensor will be able to monitor a large volume of microalgal culture. The photocurrent sensor unit is the same as presented in the chapter 4. Next to the individual photocurrent sensor unit, a low power consuming electronic control unit needs to be placed to be a stand-alone system while collecting the photocurrent signals, processing the measurements, and transferring the data to a central facility. Ultimately the photocurrent sensor system will be operated by solar cell power and enable wireless communication to centralize the measurement information. The design layout of electronic unit is described in the right bottom of the Figure 5.1. This unit consists of microprocessor, analog-to-digital converter, an amplifier and a few types of electronic switches. For current measurement, a small resistance called shunt resistor is integrated in the loop of photocurrent measurement. The applied voltage across the shunt resistor can be read by op amp and high-sensitivity ADC and finally processed as current by the microprocessor. The total cost of the electronic unit will be less than $100 by assembling commercially available circuit units (Fig. 5.2). The total power consumption will be as low as supported by a conventional solar charger. Also, we can expect much lower cost like less than $20 for the electronic unit in an actual manufacturing, which is reasonable to apply to the large-scale field applications as an inexpensive monitoring method.

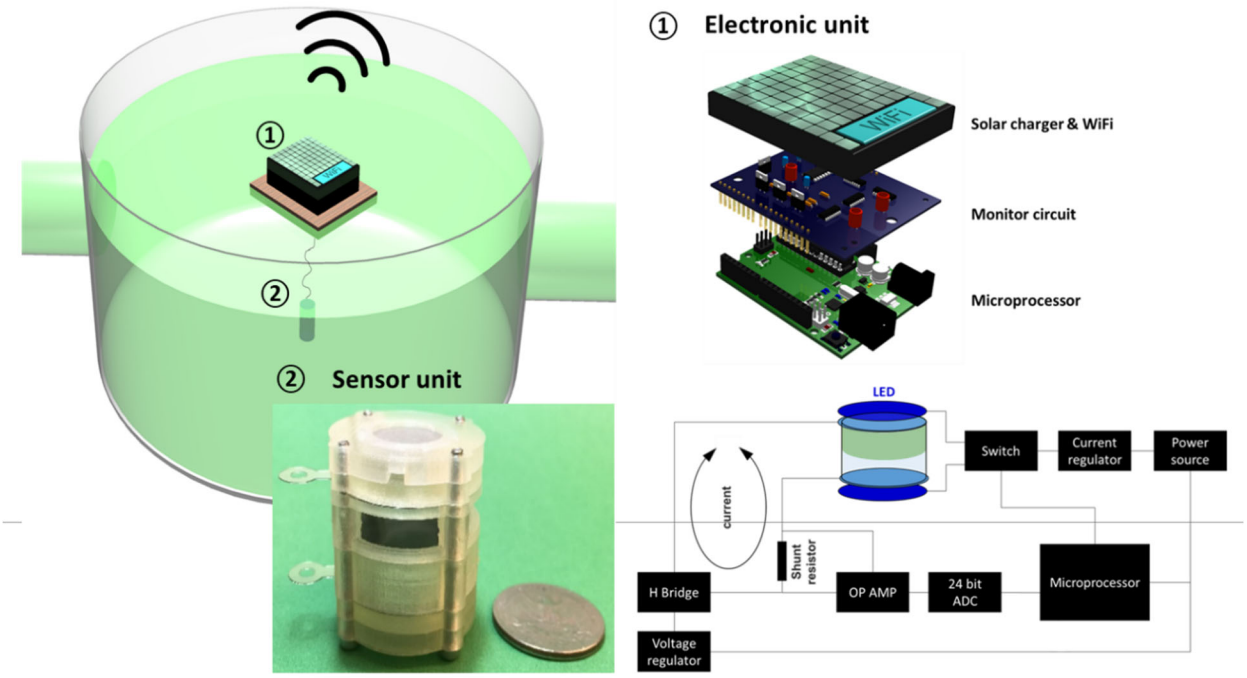

Figure 5.1. Miniaturized microalgae monitoring sensor system configured as two main units of ① floating electronic unit, and ② immerging sensor unit. Circuit diagram of the electronic unit (Right bottom).

Component	Details	Power consumption	Cost
Microprocessor	Arduino Uno	300 mW	$ 10
LED	SP-01-B4	500 mW	$ 10
Switch	Transistor	-	$ 0.01
Current regulator	CL-2NS-G	-	$ 0.1
24 bit ADC	LTC2400	10 mW	$ 10
OP AMP	LMV358	-	
H Bridge	4X transistor	-	$ 0.01
Voltage regulator	1V	-	$ 0.1
Shunt resistor	10~100 Ω	-	$ 0.01
Power source	Solar charge	> 10 W (12V)	$ 10
Total			< $ 100

Figure 5.2. Material list and cost of the electronic unit

Based on my research activities, I hope to realize ideal microalgae monitoring for real ubiquitous microalgal farming someday. We can imagine that many of the photocurrent monitoring systems will be distributed over extensive algal farms, continuously monitor the algal culture condition, and inform the measurements through wireless communication (Fig. 5.3). By using the inexpensive components, the monitoring system will not cause high costs on microalgal farming; yet, will maximize the production yield by providing tactical culturing information over a large-area farm.

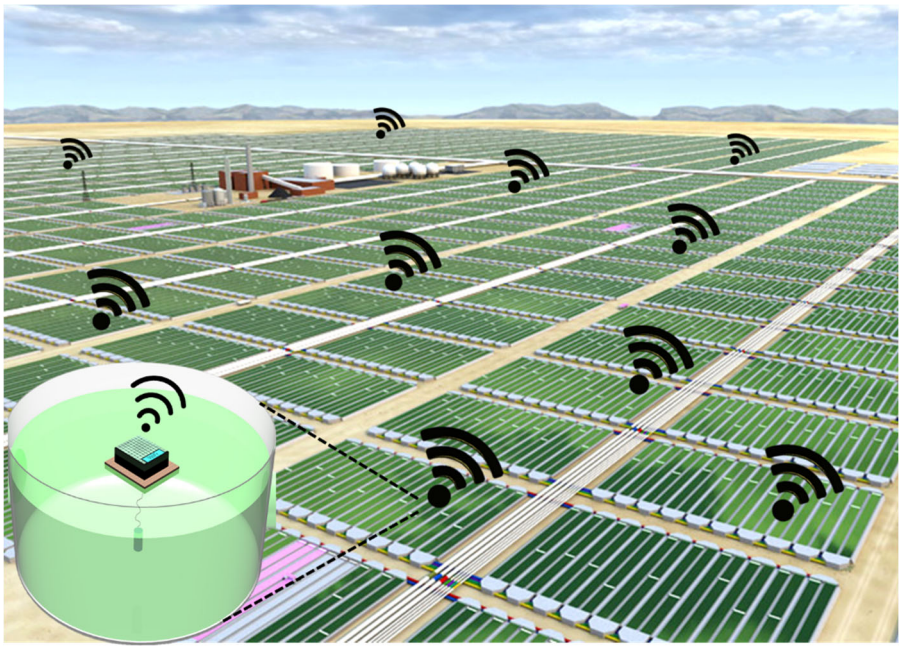

Figure 5.3. Illustration showing an ideal autonomous online microalgal monitoring for real ubiquitous microalgal farming. The miniaturized sensors as stand-alone systems distributed over extensive farms continuously monitor the algal culture condition and inform the measurement information to a central facility through wireless communication for timely production management.

Appendix

A. Supplementary Information for Label-free Density Difference Amplification-based Cell Sorting

A.1. Computational Method of the Particle Trajectory

The numerical simulations are performed using a commercial CFD software (ANSYS CFX 14.0; ANSYS, Inc.). In order to investigate the particle trajectories under the continuous flow field, the local instantaneous fluid velocity at the particle position is required. To calculate the fluid velocity, Navier-Stokes and continuity equations are considered and the fluid flow is assumed to be laminar, steady, viscous and incompressible. Governing equations are as follows:

$$\rho\left[\frac{\partial u}{\partial t}+\mathrm{u}\frac{\partial u}{\partial x}+v\frac{\partial u}{\partial y}\right]=-\frac{\partial p}{\partial x}+\mu\left(\frac{\partial^2 u}{\partial x^2}+\frac{\partial^2 u}{\partial y^2}\right), \tag{A1}$$

$$\rho\left[\frac{\partial v}{\partial t}+\mathrm{u}\frac{\partial v}{\partial x}+v\frac{\partial v}{\partial y}\right]=-\frac{\partial p}{\partial y}+\mu\left(\frac{\partial^2 v}{\partial x^2}+\frac{\partial^2 v}{\partial y^2}\right), \tag{A2}$$

$$\frac{\partial u}{\partial x}+\frac{\partial v}{\partial y}=0 . \tag{A3}$$

Particle trajectory is calculated by the Newton momentum equation (*i.e.*, $F = mdv/dt$), that is combined with the force balance equation. Each force is defined as $F_G = \rho_p V_p g$, $F_B = \rho_f V_p g$, and $F_D = C_D A_p \rho_f v^2/2$, respectively. ρ_p, ρ_f, V_p, C_D, A_p, and v are the particle density, the fluid density, the particle volume, the drag coefficient, the cross-sectional area of the particle, and the relative velocity, respectively. We adopted Schiller-Naumann model for the drag coefficient, C_D. The model is defined as $C_D = \frac{24}{Re}(1 + 0.15Re^{0.687})$ at $Re \leq 1000$ and $C_D = 0.44$ at Re > 1000, respectively.

For a coupling method between the fluid and the particle, one-way coupling is applied. In this coupling method, only the fluid affects the particle motion. There is no feedback from the particle motion to the fluid dynamics. Initially, the fluid dynamics equations are solved to provide the information of fluid field. Next, the position and velocity of the particle are calculated from the Newton momentum equation. The fluid dynamic equations and equations for particle motion are interdependently computed with the one-way coupled method.

A.2. Comparison of possible microfluidic channel configurations for density-based separation

Particles larger than a few microns suspended in a fully developed flow experience mainly three forces: gravity (F_G), buoyancy (F_B), and drag (F_D) forces. Particle trajectory is calculated by the force balance equation. Each force is defined as $F_G = \rho_p V_p g$, $F_B = \rho_f V_p g$, and $F_D = C_D A_p \rho_f v^2/2$, respectively. ρ_p, ρ_f, V_p, C_D, A_p, and v are the particle density, the fluid density, the particle volume, the drag coefficient, the cross-sectional area of the particle, and the relative velocity, respectively. The drag force can be represented as Stokes drag, $F_D = 6\pi\mu r v$, at $Re < 1$, where μ and r are the viscosity of fluid and the radius of particle. The force balance equation is combined with the Newton momentum equation (*i.e.*, $F = mdv/dt$) to describe the motion of particle. The governing equation for the motion of particles can be expressed as

$$F = m\frac{dv}{dt} = \rho_f V_p g - \rho_p V_p g + 6\pi\mu r v \ . \tag{A4}$$

The velocity and the distance are derived by the integral of the Newton momentum equation. For the y direction, the particle is affected by three different forces, such as F_B and the y component of F_D and F_G. Thus, the Newton momentum equation for y direction can be written as

$$F_y = m\frac{dv_y}{dt} = \rho_f V_p g - \rho_p V_p g + 6\pi\mu r(v_{yf} - v_{yp}) \ , \tag{A5}$$

where v_{yf} and v_{yp} represent the velocity of fluid and particle in the y direction, respectively. The velocity along y direction is calculated from the integral of the momentum equation as

$$v_y(t) = \left(v_{yf} + \frac{\rho_f V_p g - \rho_p V_p g}{6\pi\mu r} \right) + \left\{ v_{yp0} - \left(v_{yf} + \frac{\rho_f V_p g - \rho_p V_p g}{6\pi\mu r} \right) \right\} e^{-\frac{6\pi\mu r}{\rho_p V} t} \ . \tag{A6}$$

The velocity vector is approximated with the 1st order of Taylor expansion, that is

$$v_y(t) \approx v_{yp0} - \frac{6\pi\mu r}{\rho_p V} \left\{ v_{yp0} - \left(v_{yf} + \frac{\rho_f V_p g - \rho_p V_p g}{6\pi\mu r} \right) \right\} t \ . \tag{A7}$$

The height (H) is also estimated by the integral formulation from the approximated velocity as follows:

$$H(t) \approx y_0 + v_{yp0}t - \frac{3\pi\mu r}{\rho_p V}\left\{v_{yp0} - \left(v_{yf} + \frac{\rho_f V_p g - \rho_p V_p g}{6\pi\mu r}\right)\right\}t^2 \quad . \tag{A8}$$

The maximum height ($H_{\max}$) can be determined with the time when the velocity of y direction reaches 0. $H_{\max}$ can be written as

$$H_{\max} \approx y_0 + \frac{\rho_p V \left(v_{yp0}\right)^2}{12\pi\mu r\left(v_{yp0} - v_{yf}\right) - 2(\rho_f - \rho_p)V_p g} \quad . \tag{A9}$$

The difference between $H_{\max}$ of different particles, $\Delta H_{\max}$, is further estimated from the above expression as following:

$$\begin{aligned}\Delta H_{\max} &\approx V\left(v_{yp0}\right)^2 \left\{\frac{\rho_{p2}}{12\pi\mu r\left(v_{yp0} - v_{yf}\right) - 2(\rho_f - \rho_{p2})V_p g}\right. \\ &\qquad \left. - \frac{\rho_{p1}}{12\pi\mu r\left(v_{yp0} - v_{yf}\right) - 2(\rho_f - \rho_{p2})V_p g}\right\} \\ &\approx \frac{V\left(v_{yp0}\right)^2(\rho_{p2} - \rho_{p1})}{12\pi\mu r\left(v_{yp0} - v_{yf}\right)}\end{aligned} \tag{A10}$$

Thus, $\Delta H_{\max}$ has the relation as

$$\Delta H_{\max} \propto \frac{\left(v_{yp0}\right)^2}{\left(v_{yp0} - v_{yf}\right)}, (\rho_{p2} - \rho_{p1}) \quad . \tag{A11}$$

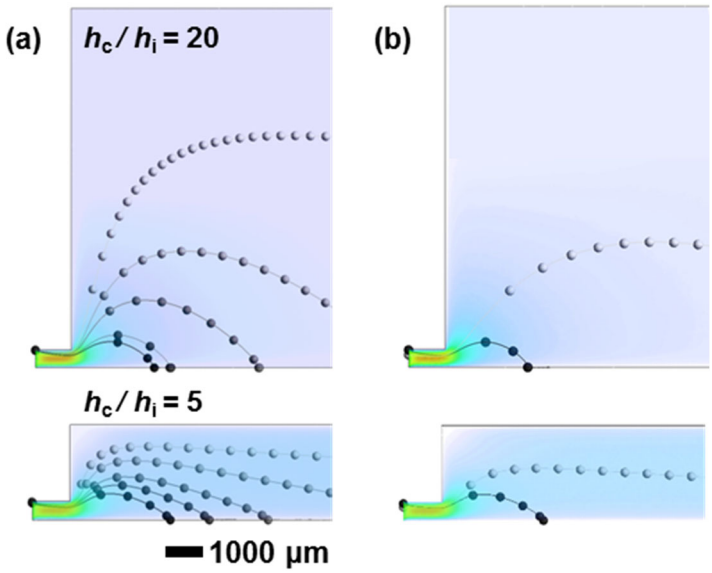

Figure A.1. Microfluidic particle separation with respect to the ratio of the height of the inlet (h_i) to the separation chamber (h_c). **(a)** Representative trajectories of particles having different densities, 1.1, 1.3, 1.5, 1.7, and 1.9 g/cm^3. **(b)** Representative trajectories of 1.1 and 1.9 g/cm^3 particles if two particles with the densities of 1.1 g/cm^3 and 1.9 g/cm^3 enter each separation chamber at the same positions (*i.e.*, same entrance heights with the heavier particle, assuming that both particles travel the same streamlines at the entrance). As the ratio of the height is increased from 5 to 20, H_{max} of the lighter particle (*i.e.*, the density of 1.1 g/cm^3) is significantly increased while H_{max} of the heavier particle remains unchanged.

B. Supplementary Information for Photonic Cavity Bioreactor for Rapid Strain Screening

B.1. Fabrication of Multi-well Photonic Cavity Bioreactor Plates

96 well platform-based photonic cavities (Fig. 3.3A) were fabricated with the ionic water lithography (Fig. 3.2). Polydimethylsiloxane (PDMS) pre-polymer was prepared by thoroughly mixing base and curing agent of Sylgard® 184 silicone elastomer kit in a 10:1 ratio, and four different concentrations of gold chloride (HAuCl4) solutions (0.2 mM, 1 mM, 2 mM, and 5 mM) were prepared from a 100 mM stock solution. Then, c.a. 40 g of PDMS pre-polymer was poured onto a 96-well plate frame (96 Well StripWell, Corning, USA) and degassed for approximately 30 min to remove all of the bubbles. Next, 200 μL of the gold chloride solution was dropped into each of the wells. As a result, the four types of photonic cavities were fabricated, and bare cavities were also prepared with DI water whose density adjusted with glycerol as an experimental control. All of the reactions were performed at room temperature for overnight. Then, the fabricated photonic cavities were rinsed with DI water to remove unreacted ions. Prior to all cell culture experiments, the cavities were autoclaved (121°C, 20 min) and incubated with TAP medium at 4 °C.

B.2. Characterization of Gold Nanoparticles in the Photonic Cavity Bioreactor

To characterize the size of the gold nanoparticles (AuNPs) and thickness of nanoparticle-infiltrated PDMS layer, we froze and cracked the fabricated photonic cavities and imaged Pt-coated pieces of them through a scanning electron microscope (FEI Quanta 3D FEG). Gold nanoparticles are embedded underneath the cavity surface so that SEM could not image the nanoparticles. In order to expose the plane holding the nanoparticles, we peeled off the nanoparticle-infiltrated layer through rapidly repeating freezing and thawing. The difference in thermal expansions enabled a clear separation of the nanoparticle-infiltrated layer from PDMS bulk. Also, for characterization of the thickness of the nanoparticle-infiltrated PDMS layer, a cross-sectioned photonic cavity was prepared through immersing a photonic cavity into liquid nitrogen and cracking normally to the inner cavity surface using a knife-edge. Then, 2 nm of platinum layer was deposited on the samples before electron microscopy imaging, On the SEM imaging, peeled PDMS bulk held a lot of dimple patterns, and the peeled PDMS layer matching PDMS bulk held an array of gold nanoparticle clusters which consist of 100-200 nm of gold nanoparticles. Also, the cross-sectional SEM image revealed that the thickness of the nanoparticle-infiltrated PDMS layer is 1-2 μm as we distinguished through energy dispersive X-Ray spectroscopy (EDX).

B.3. Calculation of Interparticle Distance of Plasmonic Nanoparticles in PCBs

The number of gold nanoparticles and interparticle distance on the surface of each photonic cavity are estimated from theoretical calculation (Table B.1). For the calculation, we assume that 80% of the gold ions are reduced to gold nanoparticles, and its size is about 150 nm in diameter, as discussed in the main text. Briefly, the number of Au atoms (n) consists of a gold nanoparticle (150 nm) is estimated from the atomic mass of Au (m_{Au}) and the density of gold nanoparticle (ρ). From that value, the total number of AuNPs ($N_{pc,i}$) that are formed in each photonic cavity is calculated from the total number of Au ion applied in ionic water lithography. Also, distance (d) between the AuNPs is estimated by assuming that the AuNPs are evenly spaced on the cavity surface. The equations used in the calculation are as follows;

$$n = \frac{\rho V_{AuNP}}{m_{Au}}$$

$$N_{pc,i} = \frac{M_{pc,i} \times N_A \times V_{pc} \times \eta}{n}$$

$$V_{pc} = \int_{-b}^{p} \pi r(h)^2 \, dh$$

$$A_{pc} = \int_{-b}^{p} 2\pi r(h) \, dh$$

$$d_{pc,i} = 2\left(R_{circle,i} - r_{AuNP}\right) = 2\left(\sqrt{\frac{A_{pc}/N_{pc,i}}{\pi}} - r_{AuNP}\right)$$

where n, ρ, V_{AuNP}, m_{Au}, $N_{pc,i}$, $M_{pc,i}$, N_A, V_{pc}, η, A_{pc}, $d_{pc,i}$, $R_{circle,i}$, and r_{AuNP} represent the number of Au molecules consist of one gold nanoparticle, density of gold nanoparticle, volume of gold nanoparticle, atomic mass of Au, total number of gold nanoparticles formed in the photonic cavity i, molar concentration of Au ion solution that is used to make photonic cavity i, Avogadro's number, volume of photonic cavity (i.e.,200 ul), reduction efficiency, surface area of photonic cavity, distance between AuNPs in photonic cavity i, radius of imaginary circle in photonic cavity i, radius of AuNP, respectively. And the ratio among *a, b,* and *p* noted in Fig. B.1. are determined based on the fabricated cavity.

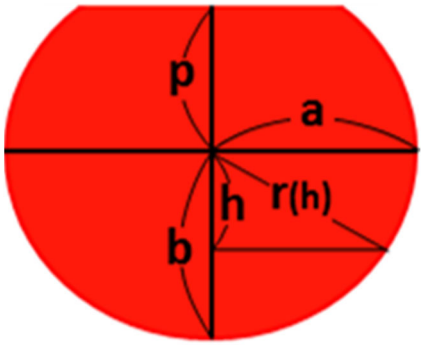

Figure B.1. Schematic of photonic cavity. Variables (a, b, p, h, r(h)) used in the calculation are indicated in the figure.

Photonic cavity	Total number of AuNPs	Interparticle Distance (nm)
PCB 1 (0.2 mM)	0.185×10^9	3276
PCB 2 (1 mM)	0.924×10^9	1382
PCB 3 (2 mM)	1.849×10^9	933.6
PCB 4 (5 mM)	4.622×10^9	535.4

Table B.1. Number of gold nanoparticles and interparticle distance in each photonic cavity.

B.4. Optical Resonance of the Plasmonic Nanostructures in PCBs

B.4.1. Dark-field microspectroscope setup

The optical resonance of plasmonic nanostructures embedded in the cavity surfaces was characterized through dark-field microspectroscopy. The dark-field microscope (Axiovert 200 inverted microscope, Carl Zeiss Inc) was equipped with a condenser (NA 1.2 /1.4, Carl Zeiss), spectrograph (Acton SP2300, Princeton Instruments) and a highly sensitive CCD camera (PIXIS 256, Princeton Instruments) for spectral measurements. Also, a color camera (MicroPublisher 3.3 RTV, QImaging) was mounted on the microscope for true color imaging. The microspectroscope setup was placed in a dark room to prevent ambient light interference. The scattered light was collected with an objective lens (LD ACHROPLAN, Zeiss), and entered the spectrograph to be separated into a series of monochromatic lights. The intensity of the monochromatic lights was measured by the CCD camera as a function of wavelength.

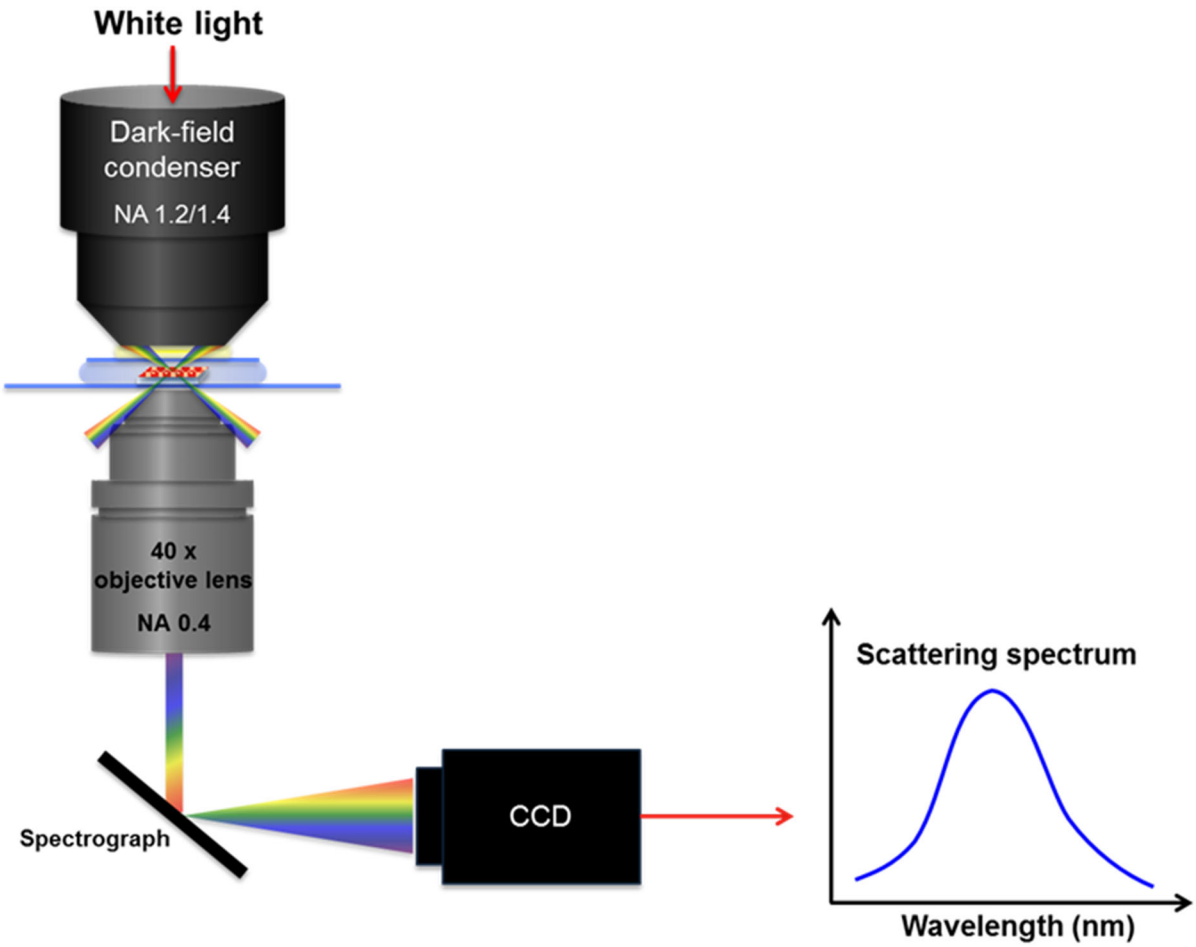

Figure B.2. Schematic illustration of dark-field microspectroscope setup.

B.4.2. Dark-field scattering measurement

The optical resonance of the gold nanoparticles embedded underneath the cavity surfaces was characterized through optical dark-field scattering measurement. For the measurement, thinly sliced pieces of photonic cavities were immersed in a glycerol solution with a refractive index identical to PDMS (n_{PDMS} = 1.4036) and covered by a cover slide (18 x 18 mm, NO.1) on top. The prepared samples were mounted on the inverted microscope, and the dark-field scattering measurement was performed by using the aforementioned dark-field microscopy setup. The dark-field images (representative one taken from the PCB 3 sample is shown in Fig. 3.3D) and scattering spectra of the four types of photonic cavities (Fig. 3.6A) were obtained from 40X objective lens. For the characterization of cavity nanoparticle scattering asymmetry (Fig. 3.4B), we used 10X, 20X, and 40X objective lenses with different numerical apertures of 0.25, 0.4, and 0.6, respectively.

B.5. Measurement of optical intensity distribution in the PCBs

The characterization of the spatial distribution of optical scattering intensity in the photonic cavity was performed (Fig. 3.5B) with a half-cut photonic cavity and normal illumination of white light (OSL2 fiber illuminator, Thorlabs Inc) as illustrated in Fig. B.3. Scattering spectra from the nanoplasmonic structure on the photonic cavity were collected with an optical fiber (0.39 NA, M29L01, Thorlabs Inc) normally positioning to the light illumination and processed by a spectrometer (USB 2000+, Ocean Optics). In order to measure the z-axis distribution of the scattering spectrum, the optical fiber scanned along the centric vertical line of the cavity at every 0.5 mm interval. The movement of the optical fiber was adjusted precisely as immobilized on an XYZ-axis translation stage.

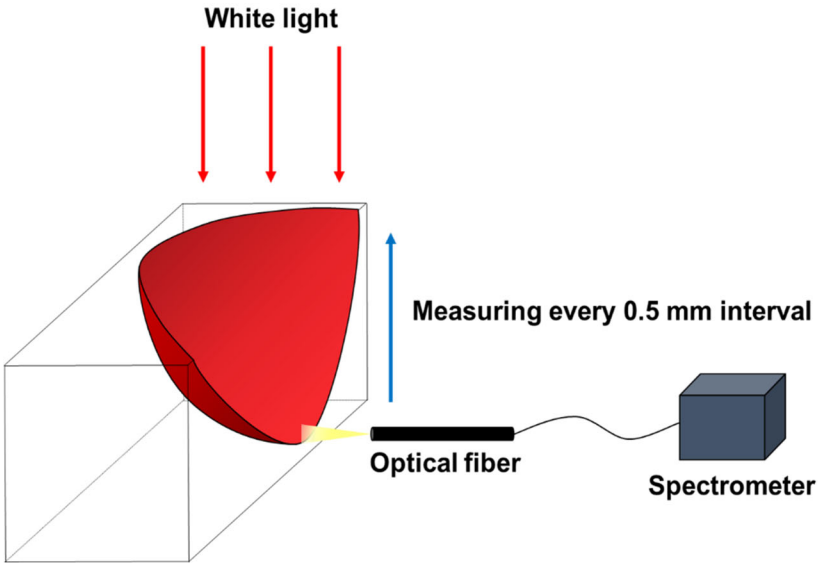

Figure B.3. Schematic of optical set up for measuring Z-axis distribution of scattering spectra from the photonic cavity. The scattering spectra were collected every 0.5 mm intervals along the Z-axis with normally positioned optical fiber from the direction of light illumination and processed by a spectrometer.

B.6. Algal Strain and Culture Conditions

Green microalgae *Chlamydomonas reinhardtii* (CC124) was cultivated in 250 mL flasks in Tris Acetate Phosphate (TAP) medium with adjusted pH = 7.0 ± 0.1. The algae were grown at 28 °C under continuous illumination of 100 µmol m^{-2} s^{-1} provided by white halogen lamps (4700 K). The cells were maintained continuously in the mid-exponential growth phase before experiments. Cells from the 5th day of the saturation phase were used for lag phase characterization and curvature effect experiments, and cells from the mid-exponential growth phase were used all of the other experiments. In the case of lipid induction experiment, the culture media of cells in the 3rd day of the stationary phase was changed from TAP to nitrogen depleted media (TAP-N; pH 7) after centrifugation (2500 rpm, 3min). The time point of cells that used in each experiment are indicated in Fig. B.4.

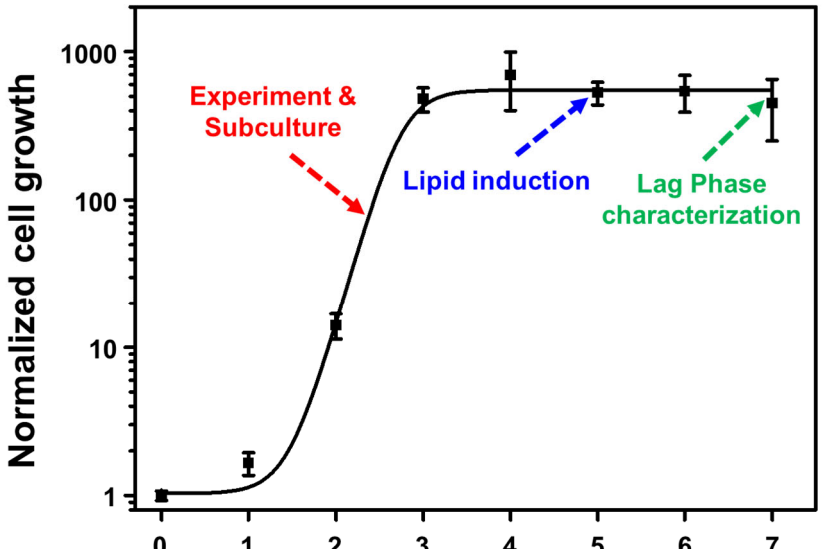

Figure B.4. Growth curve of *Chlamydomonas reinhardtii* in flask cultures with an initial concentration of 30 cells μl^{-1}. The cells were maintained continuously in the mid-exponential growth phase and used in most of the experiments unless otherwise indicated. Cells from the 3rd day and 5th day of the saturation phase were used for lipid induction, and lag phase characterization/curvature effect experiments, respectively.

B.7. Algal Pigment Characterization

In order to characterize the absorption spectra of algal pigments, pigments of *Chlamydomonas* were extracted by ethanol, and the absorption spectra were measured by spectroscopic analysis. In detail, the suspension of *Chlamydomonas* cells in the ethanol was placed in the ice bath and sonicated (40 kHz) for 20 min as 2 min break at every 5 min sonication in a sonicator (S4000, Misonix). After sonication, the suspension was centrifuged at 5000 rpm for 10 min, and the supernatant containing algal pigments was collected. For the absorption spectra measurement, the sample was prepared as follows. Punched PDMS with a 10 inches diameter was attached on the glass slide (3 x 1 in), and the extracted algal pigments solution was placed in it. In this experiment, PDMS with a thickness of 4 mm was used as a solution boundary to secure enough path length for absorption. The sample was covered by cover slide (18 x 18 mm, NO.1) and mounted on the inverted microscope (same setting with the above-mentioned dark-field spectroscopy except dark-field condenser). Then, the transmission spectra were measured with a 10X objective lens and converted to absorption spectra.

B.8. Individual Cell Tracking and 2D Histogram

In order to characterize intercellular interactions in the cavity, cellular behaviors in the cavity chamber were compared with ones in the flat chamber. 10 cells per μl were loaded in both of the chambers (V_{total}: 200 μL), and 1000 frames of time-lapse snapshot was captured at 30 fps using a stereoscope (AXIO Zoom.V16, Carl Zeiss Inc) equipped with a ring illumination. For the individual cell tracking and frequency analysis, the time-lapse snapshots were analyzed using an ImageJ (National Institutes of Health) software and MATLAB (MathWorks, MA, USA).

B.9. Time-Lapse Images / Movies for Monitoring of Cell Gathering Process

In order to monitor the algae gathering process at the bottom of the cavity, a time-lapse movie was captured for 8 hours with 6 min intervals. A population freshly paced in the cavity chamber gradually gathered at the bottom center of the cavity within 4 hours, as shown in Fig. B.5.

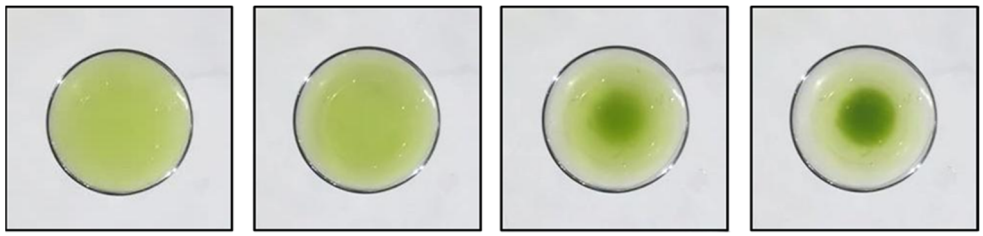

Figure B.5. Time-lapse images of the algae gathering process at the bottom of the cavity at 0, 72, 144, and 216 mins.

B.10. Curvature-Dependent Cell Growth

Cavities with different curvatures used in this work were fabricated using a two-step curing process. Firstly, the bottom part of the cavities was prepared by curing 2 g of PDMS mixture in cup shape containers. Afterward, a different amount of PDMS mixtures (2, 4, 6, 8 g) were added on each container. Then, 1 mL of water was dropped into each container and cured overnight at room temperature. As a result, cavities with four different curvatures (0.7, 1.1, 1.8, and 2.0 cm^{-1}) were fabricated. Prior to cell culture experiments, the cavities were autoclaved (121°C, 20 min) and incubated at 4 °C for 1 hour in 1% BSA in TAP media. Algae cells were inoculated in each cavity and cultured, as described in the section of 'B.6. Algal strain and culture conditions'. 18 hours after inoculation, all the cases were sampled and immediately treated with 1% formaldehyde to fix the population amount. Each of the algae population was counted by using a hemocytometer.

B.11. Correlation Between Cell Population and Gathering at the Bottom of the Cavity

In order to characterize the correlation between cell population and gathering at the bottom of the cavity, media containing 5 different cell densities (500, 1000, 2000, 4000, 8000 cells per μl) were introduced to each cavity. 4 hours later, the top view of the gathered cells in the cavity was imaged, and the intensity of green channel was determined with the ImageJ (National Institutes of Health) software (Fig. 3.8C)

B.12. Initial Cell Density-Dependent Lag Phase

In order to investigate the influence of the initial density of cells on a growth curve, *Chlamydomonas reinhardtii* (CC124) was cultivated in 250 mL flasks with three different initial densities, and their growth was monitored up to 5 days (Fig. 3.9B). Initial density of 300, 30, and 0.3 cells per μl were used as high, medium, low initial cell density, respectively, and all of the culture conditions are the same as described in the section of 'B.6. Algal strain and culture

conditions'. As shown in Figure 3.9B, the lag phase, an adoption period to a new environment, become shorter as the initial cell density increases. Low (0.3 cells per µl) and medium (30 cells per µl) initial cell density cultures show 2 days and 1 day of lag phase duration, respectively. The lag phase was virtually absent when cultures were begun at an initial cell density of 300 cells per µl.

B.13. Lag Phase Characterization in PCB

In order to assess the advantage of PCB on the early stage of culture regarding the lag phase, we inoculated CC124 as single-cell dissociation in PCB 3 (fabricated with 2 mM $HAuCl_4$), bare cavity and flat chamber as a low concentration of one cell per 5 µl. As the total volume of each culture chamber is 200 µl, approximately 40 cells (± 3.9) were placed in individual chambers, and a calculation shows intercellular distance can be 1.71 mm in the flat chamber. To minimize evaporation from the small volume over the culture duration, we covered the top of the culture chamber with a thin PDMS film, gas-permeable, but blocking water vapor evaporation. All the culture chambers were exposed with illumination of 100 µmol m^{-2} s^{-1} of the solar-like spectrum at 28 °C. At every 12 hours for 5 days, five chambers of all the cases were sampled and immediately treated with 1% formaldehyde to fix the population amount. The 100µl volume of each sample was imaged using a fluorescence microscope (Biorevo, BZ-9000, Keyence) and counted for chlorophyll-autofluorescent cells.

B.14. Cell Population / Chlorophyll Quantification

We assessed the number of cells by counting the number in a specific volume in a conventional or a home-made hemocytometer, or measuring chlorophyll optical density. In detail, the algae population was counted in a hemocytometer by sampling 100 µl of algae suspension from the cavity and adding 25 µl of 4% formaldehyde to immobilize the algae. Each counting was conducted twice, and three samples were taken for each experiment. Also, the spectrophotometric method is used to determine the quantity of chlorophyll in algal samples. 50 µl of *Chlamydomonas reinhardtii* cells sampled from photonic cavities was mixed with 150 µl of 100 % ethanol for chlorophyll extraction and incubated for 30 min in the dark at room temperature. The total volume of 200 µl is then analyzed by a spectrophotometric method (absorbance at 450 nm) in a microplate reader (Thermomax, Molecular devices).

B.15. Lipid Body Quantification

Nile red staining, which is a general fluorescent lipophilic staining method, is applied to determine the quantity of lipid body in algal samples. *Chlamydomonas reinhardtii* cells were stained with a 2 µg mL^{-1} solution of Nile red and incubated for 30 min in the dark at room temperature. Nile red fluorescence in neutral lipids was observed with a fluorescence microscope (Biorevo, BZ-9000, Keyence) equipped with a 20x objective lens, using a TRITC filter for 545 to 565 nm excitation. By being bound to neutral lipids, Nile red emits a yellow-gold fluorescence (λmax = 580 nm). Fluorescence intensity of stained lipid body was analyzed with a microscope software (BZ-H1AE, Keyence).

B.16. Lipid Body Imaging

For confocal imaging, cells from the photonic cavity at the 2nd day of the lipid induction stage were stained with BODIPY 505/515 at a final concentration of 10 μg mL^{-1} (from a stock of 1 mg/mL in ethanol), followed by 30 min incubation in the dark at room temperature. Stained cells were then fixed with 1% formaldehyde solution for 30 min, followed by rising with the TAP media. After placing on the microscope slide, algae images were captured using a laser scanning confocal microscope (LSM710, Carl Zeiss Inc) with a 100x oil immersion objective lens. For detection of BODIPY 505/515 fluorescence from neutral lipids, the 488 nm laser was used, and emission was collected between 475 and 610 nm. Chlorophyll fluorescence was also captured using a 633 nm excitation laser, and emission was collected between 620 and 700 nm. For three-dimensional imaging, Z stacks through an entire cell were acquired at 0.25 μm intervals, and each image was computationally projected using a ZEN software (Zeiss). Chlorophyll and lipid body images were also merged and pseudo-colored (Green: chlorophyll, Red: lipid body) using a ZEN software (Zeiss).